

**STATISTICAL FLUCTUATIONS OF TWO
DIMENSIONAL TURBULENCE**

by

Yonggun Jun

B.S, Pusan National University, 1997

M.S, Pusan National University, 1999

Submitted to the Graduate Faculty of
the Department of Physics & Astronomy in partial fulfillment
of the requirements for the degree of

Doctor of Philosophy

University of Pittsburgh

2006

UNIVERSITY OF PITTSBURGH
DEPARTMENT OF PHYSICS & ASTRONOMY

This dissertation was presented

by

Yonggun Jun

It was defended on

April 21, 2006

and approved by

Xiao-Lun Wu, Department of Physics & Astronomy

Walter Goldburg, Department of Physics & Astronomy

David Jasnow, Department of Physics & Astronomy

Vladimir Savinov, Department of Physics & Astronomy

Guy C. Berry, Department of Chemistry, CMU

Dissertation Director: Xiao-Lun Wu, Department of Physics & Astronomy

STATISTICAL FLUCTUATIONS OF TWO DIMENSIONAL TURBULENCE

Yonggun Jun, PhD

University of Pittsburgh, 2006

The statistics of two-dimensional (2D) turbulence driven by electro-magnetic force are investigated in freely-suspended soap film. The turbulent flow is analyzed using the particle imaging velocimetry (PIV) method. In this thesis, three important features of 2D turbulence are mainly studied.

First, the effects of addition of small amounts of polymers on 2D turbulent flows are carefully investigated. As the polymer concentration ϕ increases, large scale velocity fluctuations are suddenly suppressed at a certain ϕ . This suppression is believed to happen due to the redistribution of saddle points of the flow. It implies that the saddle structures may play a role in energy-transfer to large scales.

The thesis also presents 2D intermittency in inverse energy cascade regime. In this subrange, the energy transfers from injection scale l_{inj} to large scales. Intermittency is recognized and analyzed by the structure function $S_p(l)$ of the velocity difference between two points, and log-normal model of the energy dissipation rate ε . The analyses show signs of intermittency even though its intensity is weaker than that in three-dimensional (3D) turbulence.

Finally, single-point(SP) velocity statistics are investigated, inspired by the theory proposed by Falkovich and Lebedev (FL). This theory reveals the connection between SP statistics and forcing statistics. For forced 2D turbulence, the SP velocity probability distribution function (PDF) deviates from Gaussian when turbulence intensity is sufficiently strong, which can be explained using FL theory. In the case of decaying turbulence, SP velocity PDF gradually evolves from super-Gaussian to sub-Gaussian as time increases.

TABLE OF CONTENTS

1.0 INTRODUCTION	1
1.1 Turbulence	1
1.2 Navier-Stokes equation	1
1.3 Energy balance equation	3
1.4 Turbulent cascade model	4
1.5 Intermittency	5
1.6 The inverse energy cascade in 2D turbulence	8
1.7 The energy spectrum in 2D turbulence	9
1.8 Thesis overview	11
2.0 POLYMERS AND 2D TURBULENCE	12
2.1 Introduction	13
2.2 Experiments	14
2.3 Conclusion	25
3.0 INTERMITTENCY ON LARGE SCALES	26
3.1 Introduction	27
3.2 Experimental Results	28
3.3 Conclusion	38
4.0 SINGLE-POINT VELOCITY STATISTICS	40
4.1 Introduction	41
4.2 Experimental Results	41
4.3 Conclusion	53
APPENDIX A. HIERARCHICAL STRUCTURE MODEL	54

APPENDIX B. LOCAL AVERAGE STATISTICS	61
APPENDIX C. THE STATISTICS OF PRESSURE FLUCTUATIONS . .	68
C.1 Introduction	68
C.2 Experimental Results	69
C.3 Conclusion	78
BIBLIOGRAPHY	79
BIBLIOGRAPHY	79

LIST OF TABLES

- 1 The table of the skewness S_p and the flatness F_p of pressure fluctuations. . . . 71

LIST OF FIGURES

1	The drawing of turbulence by Leonardo da Vinci.	2
2	The picture of the energy cascade in 3D turbulence.	4
3	(a) velocity fluctuations from a jet and (b) velocity fluctuations after high-pass filtering which shows intermittent bursts (Gagne 1980 [24]).	6
4	The scheme of the eddy cannibalization in 2D turbulence.	8
5	The scheme of the energy spectrum in 2D turbulence. k_{inj} , k_{out} , and k_{dis} represent the injection scale, outer scale, and the dissipation scale, respectively. The dark shadow indicates the inverse energy cascade regime and the light shadow indicates the enstrophy cascade regime.	10
6	Experimental setup. A voltage difference $V = V^+ - V^-$ is applied to the film generating a uniform current density J . Beneath the film is a set of bar magnets with alternating poles.	15
7	The velocity fields without polymer (a) and with polymer (b) of concentration 24 ppm.	17
8	The 2nd-order structure function $S_2(l)$. l_{inj} denotes the energy injection length. In increasing order of turbulence intensity, the curves correspond to $\phi = 24, 12, 9, 3$ and 0 ppm. The inset is the plot of $\langle \sigma^2 \rangle$ (circles) and $\langle \omega^2 \rangle$ (squares) vs. ϕ (see text for details).	18
9	The PDFs of squared strain rate $P(\sigma^2)$ (a) and squared vorticity $P(\omega^2)$ (b). For $\phi < \phi_C \simeq 10$ ppm, the PDFs are nearly identical but for $\phi > \phi_C$, the PDFs become narrower. The vertical line in (a) corresponds to the square of the Zimm relaxation rate τ^{-2}	20

10	Comparison between the l.h.s. (L_{yy} , circles) and the r.h.s (R_{yy} , lines) of Eq. (2.2) for $\phi = 0$ (a) and for $\phi = 12$ ppm (b). The air friction coefficient $\alpha \simeq 0.7$ s ⁻¹ is used in both cases.	22
11	(a) The energy budget vs. ϕ . (b) v_{rms} vs. V for $\phi = 0$ (circles) and for $\phi = 15$ ppm (squares).	23
12	(a) The velocity field $\vec{v}(\vec{x})$ (arrows) and the enstrophy $\omega^2(\vec{x})$ field (color rendered). (b) The velocity field $\vec{v}(\vec{x})$ (arrows) and the square of strain $\sigma^2(\vec{x})$ field (color rendered). The image size is 4 cm \times 4 cm.	29
13	(a) The 2nd-order δv_l structure function $S_2(l)$ measured with $f = 1$ Hz (blue, $Re_\lambda = 167$) and 3 Hz (red, $Re_\lambda = 80$). The injection scale l_{inj} is marked by the vertical arrow and the outer scale $l_o \simeq 2$ cm. (b) The 3rd-order δv_l structure function $S_{(3)}(l)$ measured with $f = 1$ Hz (blue in (a), $Re_\lambda = 167$).	30
14	The flatness F_l of $P(\delta v(l))$ (a) and the skewness S_l of $P(\delta v(l))$ (b) with $Re_\lambda = 167$ and $f = 1$ Hz.	31
15	(a) The normalized PDFs of δv_l for various scales. (b) $S_p(l)$ vs. l	32
16	The scaling exponent ζ_p as a function of p . The slope of the solid line is ~ 1.2	33
17	The log-log plot of $S_p(l)$ as a function of $S_3(l)$ at $Re_\lambda = 212$. ESS tells that $S_p(l)$ scales as a function of $S_3(l)$ so that each plot is an increasing linear function. From bottom to top: $p = 1$ to 8.	34
18	The main figure shows that (i) the relative scaling exponents ζ_p/ζ_3 (diamonds) and $\overline{\zeta_p/\zeta_3}$ (squares) measured using different methods are consistent, (ii) ζ_p/ζ_3 are also consistent with the local energy dissipation rate measurements $\phi(p)$ (circles), and (iii) the intermittency in the film is stronger than that seen in Ref. [41] (triangles) but weaker than in Ref. [2] (triangle-downs). The solid line is for $\zeta_p/\zeta_3 = p/3$ and the dash line is the lognormal-model fit to our data ($\mu \sim 0.11$). The inset displays the correlation coefficients between $ \widetilde{\delta v_l} $ and ε_l' in the inertial range.	36
19	The schematic diagram for calculating the average vorticity using 2-channel LDV. The average vorticity $\bar{\omega}$ can be obtained by adding up the tangential components of the velocity at the points a, b, and c (see the text for details).	43

20	The SP velocity PDF along the forcing direction when $v_{yrms}=8.4$ (blue), 9.9 (green), 12.1 (red), and 13.2 (black) cm/s, corresponding to $Re_\lambda = 110, 137, 180,$ and 212, respectively. The curves in the main figure are normalized whereas those in the inset are unnormalized. The tails of the PDFs deviate from Gaussian, which is delineated by the dashed line.	45
21	The normalized even moments $\Phi(p)$ vs. p . The symbols correspond to $Re_\lambda = 110$ (diamonds), 137 (stars), 180 (triangles), and 212 (circles). $\Phi(p)$ for the normal distribution is plotted as squares. The inset shows the integrand $v_y^{10}P(v_y)$ for $Re_\lambda=110, 137, 180,$ and 212.	46
22	The SP velocity v_x (a) and vorticity $\bar{\omega}$ (b) PDFs at different times t in decaying 2D turbulence. As t increases (0.01, 0.02, 0.03, 0.05, 0.08, 0.11, 1.15, 0.18, 0.21, 0.26, and 0.33 s), the $P(v_x)$ becomes narrower, and evolves from sub-Gaussian ($F < 3$) to super-Gaussian ($F > 3$). The $P(\bar{\omega})$ however remains approximately Gaussian. The inset displays the late-time velocity PDFs with $t=0.21, 0.26,$ and 0.33 s.	48
23	(a) The flatness F (a), and (b) the normalized energy E/E_0 (squares) and the normalized enstrophy Ω/Ω_0 (circles) vs. t	49
24	The normalized SP velocity PDF (circles) and the PDFs calculated based on the energy injection rate ε with $\alpha = 2/5$ (thick red line) and $1/3$ (thin green line) at $Re_\lambda = 212$ (see text for more details). The Gaussian PDF is presented by the dashed line. Inset: Exponent α is plotted as a function of v_{yrms}	52
25	The log-log plot for the test of the hierarchical structures: $\frac{H_{p+1}(l)}{H_2(l)} = \frac{A_p}{A_1} \left[\frac{H_p(l)}{H_1(l)} \right]^\beta$. It is represented as the circles and the squares at $Re_\lambda=212$ and 110, respectively. The solid line and the dashed line denote the slope $\beta=1$ and $2/3$, respectively.	57
26	The plots of Eq (A.14). Δ is obtained from the slopes of the plots: 0.31 for $Re_\lambda = 212$ and 0.49 for $Re_\lambda = 110$	58
27	The plot of ζ_p/ζ_3 based on the log-Poisson fit for $Re_\lambda = 212$ (a) and 110 (b).	60

28	The coarse-grained energy transfer rate Π_l as a function of the coarse-grained strain rate σ_l^2 . The length scales are 0.31 (squares), 0.62 (circles), 0.93 (triangle), 1.24 (triangle-down), 1.56 (diamond), 1.87 (triangle-left), and 2.17 (triangle-right) cm. The arrow denotes $\sigma_l^2 = 4500 \text{ s}^{-2}$	62
29	The coarse-grained outward energy flux Π_l^+ (circles) and inward flux Π_l^- (squares). The length scales l are 0.31 (a), 0.93 (b), 1.56 (c), and 2.17 (d) cm.	64
30	The number of events (frequency) of the coarse-grained outward energy flux Π_l^+ (circles) and inward flux Π_l^- (squares). The length scales l are 0.31 (a), 0.93 (b), 1.56 (c), and 2.17 (d) cm.	65
31	(a) The coarse-grained high order moments $G_p(l)$. From bottom to top, $p=1$ to 9. (b) The scaling exponent ζ_p/ζ_3 as a function of p . The squares represent data from previous analysis [29] and the circles are obtained from coarse-grained velocity difference.	66
32	The snapshot of the pressure field (color-coded) and the velocity field (arrows).	70
33	The non-dimensionalized PDF of pressure for all runs (see Table 1). The black, red, blue, and green lines indicate the run 1, 2, 3, and 4, respectively. The tail part of the PDF decays exponentially.	72
34	The lower moments of pressure fluctuations: (a) p_{norm} , (b) the skewness S_p , and (c) flatness F_p (see the contents for the definitions)	73
35	The pressure PDFs in presence of polymer.	75
36	The pressure spectrum $E(k_x, k_y)$ in k -space.	76
37	The power spectrum of the pressure $E_{pp}(k)$ for four different turbulence intensities: $\text{Re}_\lambda =$ (squares), 180 (circles), 137 (triangle-ups), and 110 (triangle-downs). All have same scaling exponent in both of large and small scales.	77

1.0 INTRODUCTION

1.1 TURBULENCE

Turbulence is recognized as irregularly fluctuating and unpredictable motion which is composed of a number of small eddies that travel in the current. It is ubiquitous but has been a very difficult subject to study. It is natural that, in spite of the difficulty involved, turbulence has taken the attention of engineers and physicists because of its practical importance in applications such as weather forecasting, aeronautical engineering, etc.

1.2 NAVIER-STOKES EQUATION

The dynamics of fluids is described by two equations: the Navier-Stokes equation

$$\frac{\partial \vec{v}}{\partial t} + (\vec{v} \cdot \nabla) \vec{v} = -\frac{1}{\rho} \nabla P + \nu \nabla^2 \vec{v}, \quad (1.1)$$

and the continuity equation

$$\frac{\partial \rho}{\partial t} + \nabla \cdot (\rho \vec{v}) = 0, \quad (1.2)$$

where \vec{v} is the velocity, P the pressure, and ν the kinematic viscosity coefficient. Eq. (1.2) can be rewritten as

$$\nabla \cdot \vec{v} = 0 \quad (1.3)$$

when ρ is constant. This is considered as an incompressible condition of fluid. The meanings of each term of Eq. (1.1) are as follows: (1) the inertial term, $(\vec{v} \cdot \nabla) \vec{v}$, is responsible for momentum transport. This is the only nonlinear term in the equation which makes the



Figure 1: The drawing of turbulence by Leonardo da Vinci.

phenomenon complex and rich. (2) $-\nabla P$ is the pressure gradients term. It does not contribute to the creation of the dissipation of the energy, but it accelerates the fluid molecules and redistributes energy among different velocity components. (3) $\nu \nabla^2 \vec{v}$ is the viscous term dissipating the injected energy. Due to this term, the kinetic energy is not conserved.

Turbulence can be characterized in terms of Reynolds number

$$\text{Re} = \frac{UL}{\nu},$$

where U and L are the typical velocity and length scale in the flow, respectively. The dimensionless number Re was first introduced by Osborne Reynolds to describe the transition from a laminar to turbulent flow. The Taylor microscale Reynolds number Re_λ is frequently used for experimental and numerical works because it is independent of the system geometry. The quantity Re_λ is defined as:

$$\text{Re}_\lambda \equiv \frac{v_{rms}\lambda}{\nu},$$

where v_{rms} is the root mean squared velocity defined as $\sqrt{\langle v_1^2 \rangle - \langle v_1 \rangle^2}$, and the Taylor micro-length scale λ is defined as

$$\frac{1}{\lambda^2} \equiv \frac{\langle (\partial_1 v_1)^2 \rangle}{v_{rms}^2},$$

where v_1 is the first component (x-component) of velocity [23]. The brackets in the above equation are ensemble or time averages of v_1 .

1.3 ENERGY BALANCE EQUATION

When the total energy E is $\langle \vec{v}^2 \rangle / 2$, the following relation can be obtained by multiplying \vec{v} and ensemble-averaging on both sides of Eq. (1.1):

$$\frac{\partial E}{\partial t} = \langle -\vec{v} \cdot (\vec{v} \cdot \nabla) \vec{v} - \vec{v} \cdot \nabla p + \nu \vec{v} \cdot \nabla^2 \vec{v} \rangle, \quad (1.4)$$

where reduced pressure $p = P/\rho$. Assuming the periodic boundary condition on the cubic volume L^3 , one can obtain the following relations by integrating by parts:

$$\langle \partial_i f \rangle = 0, \quad (1.5)$$

$$\langle (\partial_i f) g \rangle = -\langle f \partial_i g \rangle, \quad (1.6)$$

where f and g are the arbitrary periodic functions. Using Eq. (1.3), (1.5), and (1.6), the first two terms in the right-hand side of Eq. (1.4) vanish [23]. By use of the vector identity

$$\begin{aligned} (\nabla \times \vec{v}) \cdot (\nabla \times \vec{v}) &= (\epsilon_{ijk} \partial_j v_k)(\epsilon_{ilm} \partial_l v_m) \\ &= \partial_j (v_k \partial_j v_k) - \partial_j \partial_k (v_j v_k) - v_k (\partial_j \partial_j v_k), \end{aligned}$$

one can get

$$\frac{dE}{dt} = \nu \int \vec{v} \cdot \nabla^2 \vec{v} dV = -\nu \int (\nabla \times \vec{v})^2 dV = -\nu \int \omega^2 dV,$$

where the vorticity $\omega = \nabla \times \vec{v}$. The energy balance equation of Eq. (1.4) is then as follows:

$$\frac{dE}{dt} = -2\nu\Omega,$$

where the enstrophy $\Omega = \langle \omega^2 \rangle / 2$. For an inviscid condition, $\nu = 0$, the energy is a conserved quantity. In the limit $\nu \rightarrow 0$ the total energy is not conserved, but it is constantly dissipated [23]: $\lim_{\nu \rightarrow 0} 2\nu\Omega \equiv \langle \varepsilon \rangle$, where $\langle \varepsilon \rangle$ is the mean energy dissipation rate of the system.

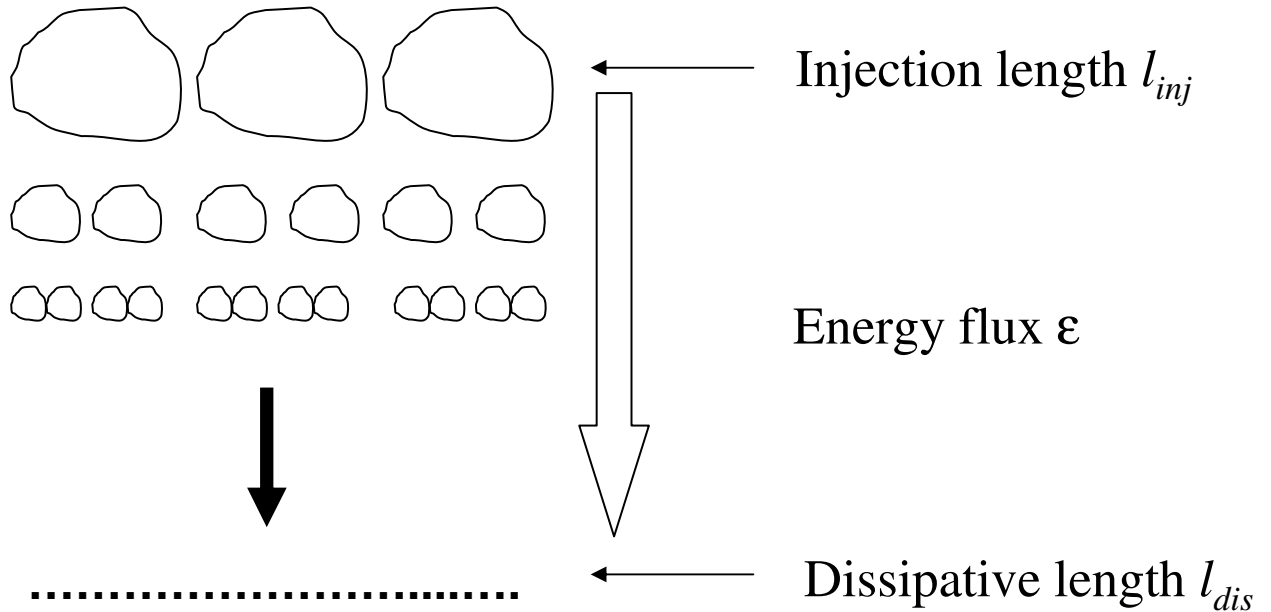


Figure 2: The picture of the energy cascade in 3D turbulence.

1.4 TURBULENT CASCADE MODEL

Although there have been many studies to define the eddy [22], it is not well defined. It is, loosely speaking, the volume where the fluid moves coherently and pressure is lower than in the vicinity. The turbulent cascade is expressed in terms of the eddy. The cascade picture was first given by R.F. Richardson in an evocative piece of a poem [46]:

'..Big whorls have little whorls
that feed on their velocity,
and little whorls have lesser whorls
and so on to viscosity...'

Large eddies that are given at an injection length scale l_{inj} , which is the length where the energy is injected, break down to smaller eddies. In turn, smaller eddies break down to even smaller eddies, and so on. This process goes on until the dissipation length scale l_{dis} is reached, and all the input energy is dissipated into heat due to molecular friction. This length scale is determined by the viscosity ν and the energy dissipation rate $\langle \varepsilon \rangle$: $l_{dis} = (\nu^3 / \langle \varepsilon \rangle)^{1/4}$.

The length scale from l_{inj} to l_{dis} is called the inertial range where the energy is conserved and is transferred to the smaller scales.

1.5 INTERMITTENCY

One of the statistical methods to investigate the phenomenology of turbulence is the structure function $S_p(l)$,

$$S_p(l) = \langle (\delta v_l)^p \rangle = \int (\delta v_l)^p P(\delta v_l) d(\delta v_l), \quad (1.7)$$

where the two-point longitudinal velocity increment δv_l is defined as $\delta v_l \equiv [\vec{v}(\vec{x} + \vec{l}) - \vec{v}(\vec{x})] \cdot \hat{l}$, and \hat{l} is the unit vector in the longitudinal direction between the two points, and $P(\delta v_l)$ is the probability distribution function (PDF) of δv_l . From the Karman-Howarth relation [39], Kolmogorov derived an exact relation for the third moment in fully developed three-dimensional turbulence in 1941, well known as Kolmogorov's four-fifths law (K41) [31],

$$S_3(l) = \langle (\delta v_l)^3 \rangle = -\frac{4}{5} \langle \varepsilon \rangle l,$$

where the quantity $\langle \varepsilon \rangle = \nu \langle \sum_{i,j} (\partial_i v_j + \partial_j v_i)^2 \rangle / 2$ is the average energy dissipation rate and the bracket is the ensemble or time average.

In order to illustrate intermittency, an example is presented. As shown in Fig. 3 (a), which is an example of velocity fluctuations from a jet [24], velocity fluctuations look likely self-similar. When, however, the signal is passed through the high-pass filter, the signal shows intermittent behavior as shown in Fig. 3 (b). Intermittency is the rare and sudden events switching from quiescent to bursting behaviors.

The experimental measurements [2] showed that the structure function scales as

$$S_p(l) = \langle (\delta v_l)^p \rangle = \int (\delta v_l)^p P(\delta v_l) d(\delta v_l) \sim l^{\zeta_p},$$

where ζ_p is a nonlinear function of p and significantly deviated from Kolmogorov's prediction [31], $\zeta_p = p/3$. The deviation implies that $P(\delta v_l)$ is not self-similar in the inertial range and decays slowly with long tails. The presence of such tails is called intermittency. The strength

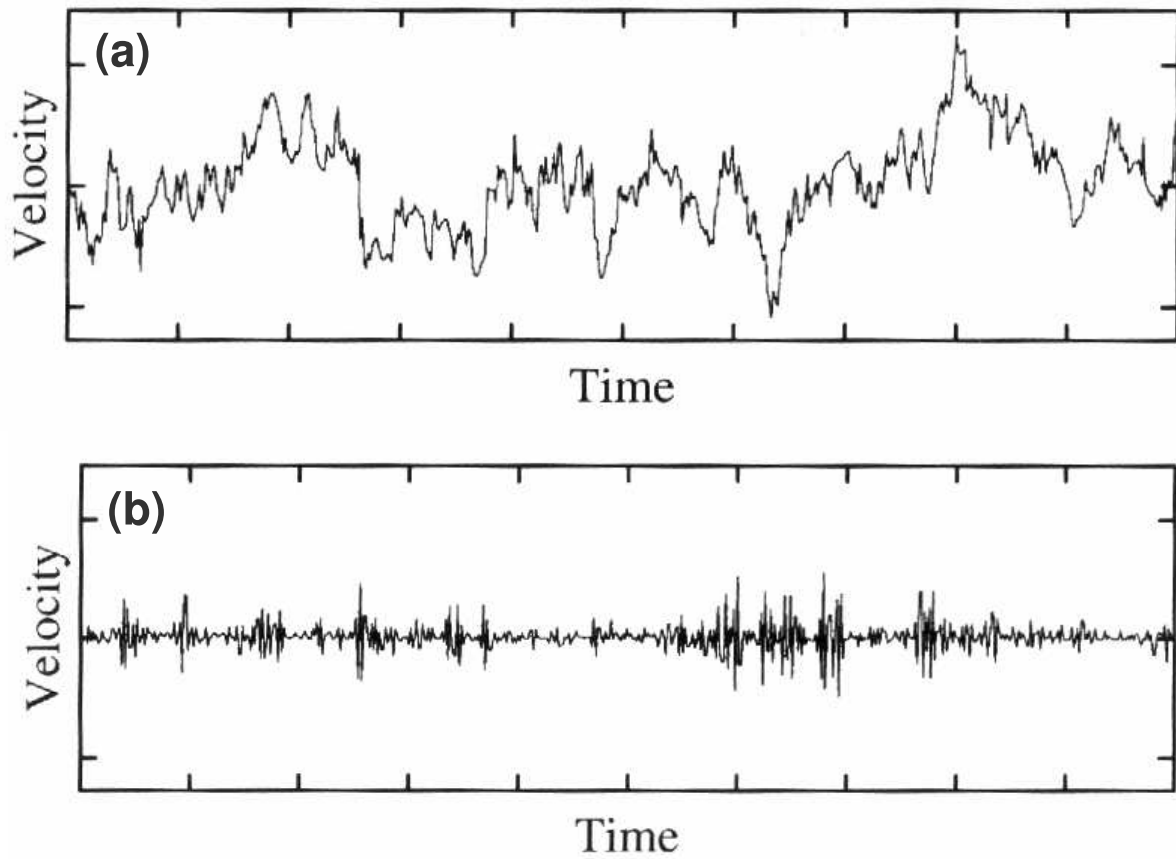


Figure 3: (a) velocity fluctuations from a jet and (b) velocity fluctuations after high-pass filtering which shows intermittent bursts (Gagne 1980 [24]).

of intermittency can be characterized in terms of $\mu(\equiv 2\zeta_3 - \zeta_6)$, which indicates how much the scaling exponent ζ_6 deviates from K41 ($2\zeta_3 = \zeta_6$).

In order to account for intermittency, Kolmogorov suggested a hypothesis, known as Kolmogorov's refined similarity hypothesis [32]. He assumed the relation between two point velocity difference δv_l and the local energy dissipation rate ε_l :

$$\langle(\delta v_l)^3\rangle \sim \varepsilon_l l,$$

where $\varepsilon_l = 1/V \int_{|x|<l/2} \varepsilon dV$ and V is a volume of a diameter l . Assuming that the local energy dissipation rate has its own scaling relation

$$\langle\varepsilon_l^q\rangle \sim l^{\tau_q},$$

a new scaling relation can be obtained

$$\langle(\delta v_l)^p\rangle \sim \langle(\varepsilon_l l)^{p/3}\rangle$$

with the exponent

$$\zeta_p = p/3 - \tau_{p/3}.$$

This relation has been tested and shown to be in a reasonable agreement with Kolmogorov's hypothesis in fully developed 3D turbulence [55, 43, 27]. Kolmogorov assumed the log-normal distribution of $P(\varepsilon_l)$, which means that they are not self-similar in all scales. The log-normal model is good for small p but is insufficient to account for recent experimental data [2]. Many models have been proposed to explain the anomalous scaling exponents ζ_p , such as the multifractal analysis by Parisi and Frisch [42] and log-Poisson model by She and Leveque (SL) [52]. In particular, the SL model, based on the hierarchical structure of the energy dissipation, shows good agreement with experimental data.

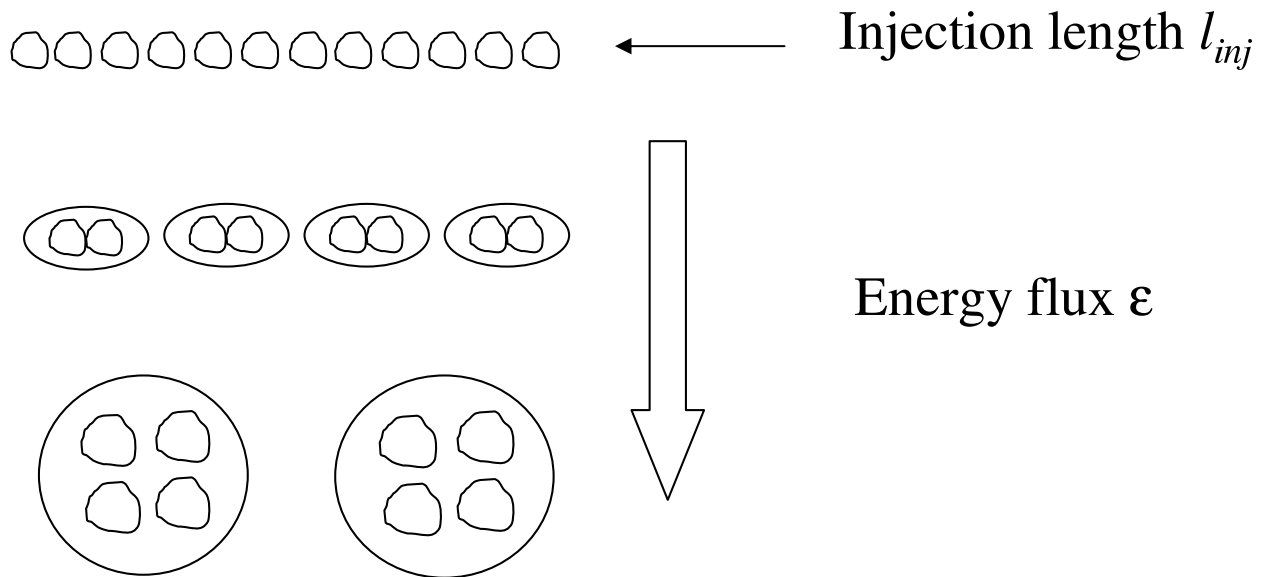


Figure 4: The scheme of the eddy cannibalization in 2D turbulence.

1.6 THE INVERSE ENERGY CASCADE IN 2D TURBULENCE

While the eddies cascade to small scales in 3D turbulence due to the vortex stretching, they cannot cascade to small scales in 2D turbulence because there is no vortex stretching in low dimensions. Instead of vortex stretching, there is vertex merging process in 2D turbulence. The eddies are generated at the injection scale l_{inj} . Two eddies interact with each other. When two neighboring eddies have the same rotating direction, they merge and become a single larger eddies. In turn, larger eddies merge into an even larger eddy, as shown in Fig. 4. This process may be called “cannibalization” of eddies. Because the energy sustaining the eddy is proportional to $l^{2/3}$, eddy cannibalization makes the energy transfer to larger scales. This type of the energy flow is known as the inverse energy cascade [33].

When the system is confined and the energy dissipation at large scales is weak, two large eddies of half the size of the system exist, which is called the condensation state, first noticed by Kraichnan [33]. In this state, the energy is concentrated at the smallest wave-number which is comparable to the system size. This phenomenon has been verified by Smith and

Yakhot in computer simulation [53] and by Paret et al. in an experiment [41].

1.7 THE ENERGY SPECTRUM IN 2D TURBULENCE

Assuming that the energy is injected through a narrow energy band around the wave number k_{inj} , one can anticipate that the energy $E = \langle v^2 \rangle / 2$ transfers to smaller $k (< k_{inj})$ and the enstrophy $\Omega = \langle \omega^2 \rangle / 2$ transfers to larger $k (> k_{inj})$ where $\omega = (\nabla \times \vec{v}) \cdot \hat{z}$.

The energy and enstrophy injection rates are denoted as ε_{inj} and χ_{inj} , and the transfer rates of the quantities are $\varepsilon_t = (\delta v_l)^3 / l$ and $\chi_t = (\delta v_l)^3 / l^3$, respectively. If k_{dis} is the maximum wave number where the viscosity cannot be ignored, the energy and enstrophy are independent of k in the inertial range ($k_{inj} < k < k_{dis}$), that is,

$$\varepsilon_t(k) = \varepsilon_t(k_{dis}) \quad \text{and} \quad \chi_t(k) = \chi_t(k_{dis}).$$

By dimensional analysis, one can obtain the relation,

$$k_{dis}^2 \varepsilon_t(k_{dis}) \sim \chi_t(k_{dis})$$

Therefore, if $\nu \rightarrow 0$ or $k_{dis} \rightarrow \infty$, $\varepsilon_t(k_{dis}) \rightarrow 0$ because $\chi_t(k_{dis})$ is constant over the inertial range. This shows that the energy cannot be transferred into small scales in the inertial range so that only the enstrophy transfers to small scales. The energy spectrum in the enstrophy cascade regime is obtained by dimensional analysis,

$$E(k) \sim \chi_t^{2/3} k^{-3}, \tag{1.8}$$

where $\langle v^2 \rangle / 2 = \int E(k) dk$.

Similarly, the energy spectrum in the inverse energy cascade regime can be obtained by showing that only the energy transfers to large scales. It is determined by k and ε_t ,

$$E(k) \sim \varepsilon_t^{2/3} k^{-5/3}. \tag{1.9}$$

Fig. 5 shows a simple diagram of the energy cascade $E(k)$ in 2D turbulence. When the energy E and the enstrophy Ω are injected in k_{inj} , E transfers to small k and ceases at

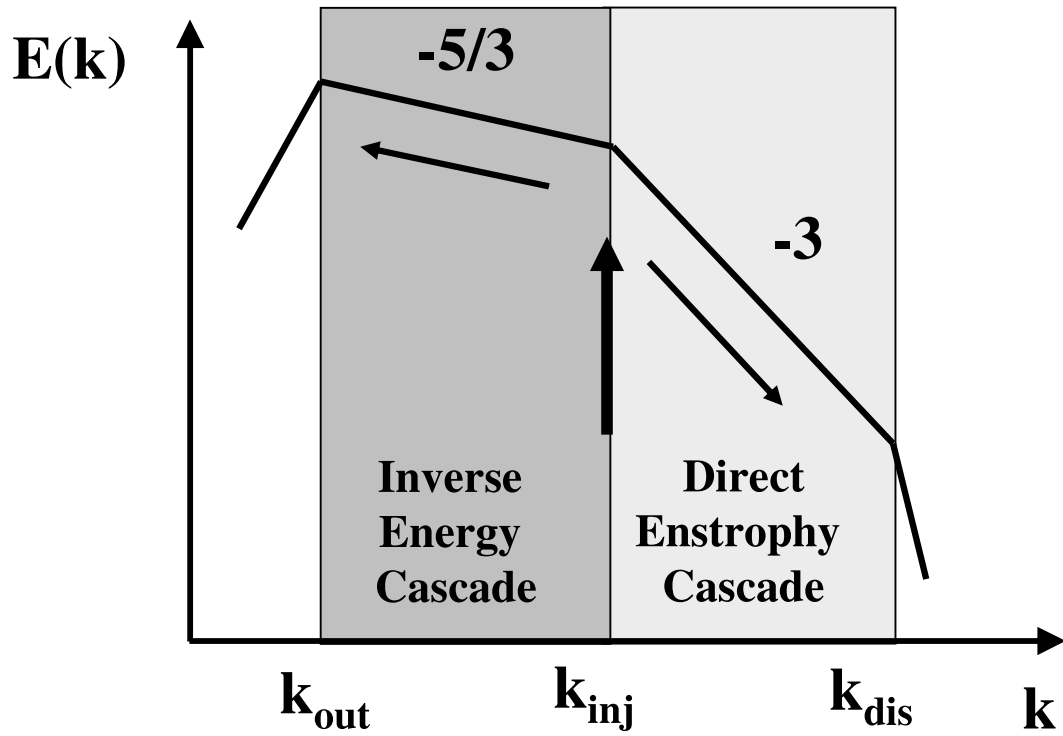


Figure 5: The scheme of the energy spectrum in 2D turbulence. k_{inj} , k_{out} , and k_{dis} represent the injection scale, outer scale, and the dissipation scale, respectively. The dark shadow indicates the inverse energy cascade regime and the light shadow indicates the enstrophy cascade regime.

k_{out} , which is the minimum wave number where the energy dissipation cannot be ignored, while Ω goes to large k and stops at k_{dis} . The energy spectrum for 2D turbulence was first calculated by Kraichnan [33] based on statistical physics. Later, The energy spectrum in 2D turbulence was confirmed through computer simulations [53, 11] and experiments [54, 51].

1.8 THESIS OVERVIEW

This thesis focuses on the statistical properties of 2D turbulence. It covers topics such as the turbulent interaction with small amounts of polymers, intermittency in large scales, the single-point velocity statistics in forced and decaying turbulence, and the topological structures of flows.

Chapter 2 describes the polymer effects on 2D turbulent flow. It is investigated how the addition of small amounts of polymers changes the large scale velocity fluctuations as the concentrations of polymer and the energy injection rates are varied.

Chapter 3 presents the analysis of intermittency at large scales. The high-order structure functions are analyzed by means of extended self-similarity. Also, intermittency is investigated through the log-normal model and the hierarchical structures. The latter is presented in the appendix. All analyses were performed in the inverse energy cascade regime.

Chapter 4 concerns the single-point velocity statistics in 2D forced and decaying turbulence. The dependency of the PDF on Reynolds number is studied in forced turbulence. The change of PDFs as a function of decaying time is also investigated in the soap channel experiment.

2.0 POLYMERS AND 2D TURBULENCE

We investigate the effect of dilute polymers on driven two-dimensional (2D) turbulence in a soap film. Transitions from strong to weak turbulence are identified by independently varying the polymer concentration ϕ and the energy injection rate ε_{inj} . Studies of velocity structures in small scales reveal that strong saddles are suppressed whereas weak ones become more populated. Interestingly, this redistribution of saddle points in turbulent flows strongly correlates with the quenching of velocity fluctuations on large scales, suggesting that this hydrodynamic structure may play a role in transferring energy from scale to scale.

2.1 INTRODUCTION

The effects of polymers on fluid flows and turbulence have attracted much attention since the pioneering work of Toms, who discovered that a trace amount of polymers can significantly reduce turbulent drag in pipe flows [57]. The phenomenon appears to be counter-intuitive because polymers typically increase the viscosity of a fluid such that hydrodynamic resistance is expected to increase. The importance of the phenomenon is evident as turbulent drag is a significant limiting factor for competitive sports such as swimming and sailing as well as for the efficient transport of crude oil through pipelines. However, this fascinating effect is not fully understood.

An early theoretical model on turbulent drag reduction was proposed by Lumley [37] who postulated that the effect is caused by a change in the flow-wall interaction in the presence of polymers. Tabor and de Gennes [56] gave an alternative interpretation and conjectured that turbulent eddies can be modified by the polymer so that the drag reduction is not a surface effect. According to this latter theory, strongly deformed polymers, if concentrated enough, can sequester significant amounts of kinetic energy from the flow and truncate turbulent energy cascades. The quenching of turbulence therefore requires the following two considerations. (i) The time criterion: the strain rate σ on the scale of a polymer should be larger than the inverse relaxation (Zimm) time τ^{-1} ($\tau = \eta R_g^3 / (k_B T)$) of the polymer, equivalently, the Weissenberg number $W = \tau\sigma > 1$, where η is the viscosity of fluid, k_B the Boltzmann constant, and T the temperature. Here, R_g is the radius of gyration which is $N^{3/5}b$ for an ideal chain, where N is the number of the monomers per chain, and b is the size of the monomer. (ii) The energy criterion: the energy density of elastic deformation of the polymer solution should be comparable to the kinetic-energy density of turbulence. Subsequent theoretical analyses using a simplified turbulence (shell) model [8] and a more realistic constitutive equation in the Navier-Stokes equation [17] are largely consistent with the physical picture in [56]. Though these theoretical ideas are appealing, their quantitative verification in laboratory experiments is still lacking. This provides a strong motivation for the current experiment.

It was found recently that a small amount of polymers could have an effect on 2D

turbulence [15, 1] as well as on 3D turbulence. Quenching of large-scale velocity fluctuations was discovered in decaying turbulence in a flowing soap film [1] and later confirmed by direct numerical simulations of a linear viscoelastic model [10]. The effect is remarkable, considering that in 2D the energy cascade direction is reversed with the kinetic energy being transferred from small to large scales. Since most of the injected energy cannot reach small scales in 2D, naively one would expect that large-scale velocity fluctuations would not be affected by polymers. It is noted that in a typical 2D turbulence experiment, the energy injection scale l_{inj} is about two orders of magnitude greater than the dissipative scale and is about four orders of magnitude greater than the radius of gyration R_g of polymers. One of the aims of this work is to elucidate how the fine structures of 2D turbulence are affected by the presence of a small amount of polymers and how these structural modifications result in the quenching of turbulence on large scales. Since the full velocity fields $\vec{v}(\vec{x})$ are acquired by particle imaging velocimetry (PIV) and the experiment allows a precise control of the energy injection rate $\varepsilon_{inj} = \langle \vec{f} \cdot \vec{v} \rangle$ (\vec{f} is an external force), it becomes feasible to calculate the energy budget scale-by-scale and to deduce the energy consumption by polymer deformation as the polymer concentration ϕ is varied. We have identified a sharp transition at $\phi = \phi_C$ where turbulent intensity drops precipitously along with a sharp increase in the energy uptake by the polymers. An interesting finding of this experiment is that the quenching of turbulence on large scales is accompanied by the suppression of strong saddles in the flow, suggesting that there may be a connection between saddles and energy transfer in 2D turbulence.

2.2 EXPERIMENTS

Our experiments were performed using a freely-suspended soap film ($7 \times 7 \text{ cm}^2$) in an electromagnetic (E&M) convection cell [48] shown in Fig. 6. Two edges of the film were in contact with metallic electrodes, allowing a square-wave voltage V ($f = 3 \text{ Hz}$) to be applied. The film was placed $\sim 1 \text{ mm}$ above a set of bar magnets with alternating poles. The width of each magnet is $a = 3 \text{ mm}$, the corresponding energy injection length $l_{inj} = 2a/\sqrt{3} \simeq 0.35 \text{ mm}$, and the strength of the surface field is 3 T. A computer controlled feedback system maintained

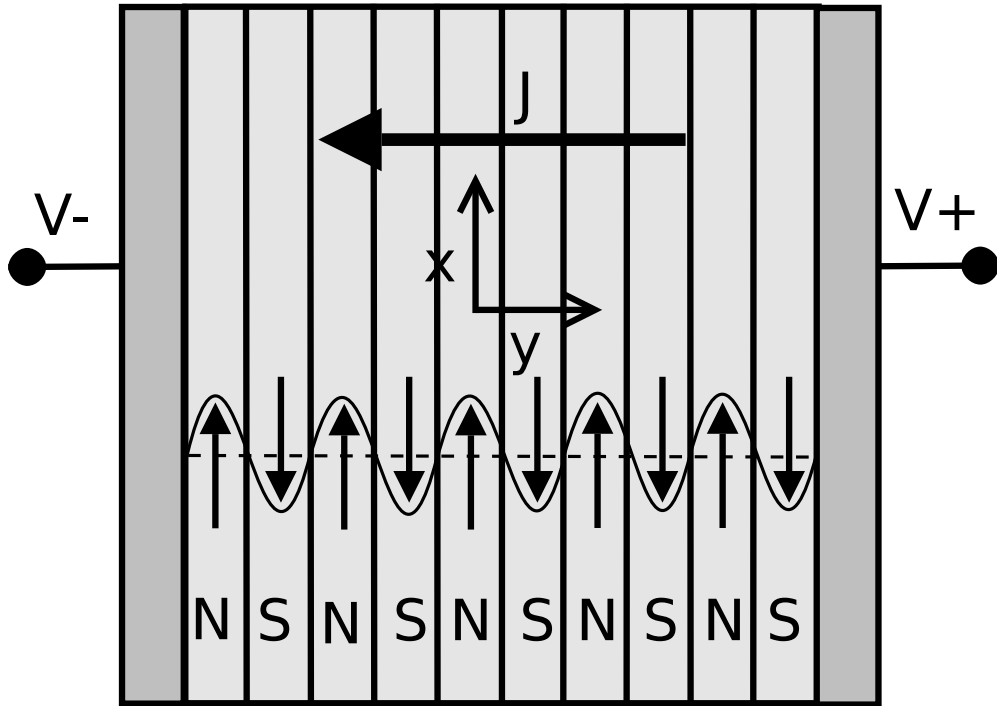


Figure 6: Experimental setup. A voltage difference $V = V^+ - V^-$ is applied to the film generating a uniform current density J . Beneath the film is a set of bar magnets with alternating poles.

the film-to-magnet distance and the film thickness $h \simeq 50 \mu\text{m}$. For small V , the flow is laminar with a set of shear bands known as the Kolmogorov flow. Upon increasing V , the system undergoes a sequence of instabilities and becomes turbulent when $V > 20$ volts. The soap solution was made of a mixture of four components (5 cc liquid detergent, 80 g ammonium chloride, 40 cc glycerol, and 400 cc distilled water). Linear polymers (polyethylene-oxide, $M_w = 8 \times 10^6$, $R_g \simeq 0.4 \mu\text{m}$) of varying concentrations ($0 < \phi < 25$ ppm) were used. Within this concentration range, there is no overlap between polymer coils as evidenced by a small ϕ dependence of the kinematic viscosity of the soap solution, which we determined to be $\nu \simeq 0.016 \text{ cm}^2/\text{s}$. To measure the velocity field $\vec{v}(\vec{x})$, the film was seeded with hollow glass spheres (diam=10 μm , $\rho = 1.05 \text{ g/cm}^3$). A 12 mJ double-pulsed Nd:YAG laser slaved to a CCD camera (Redlake, 1016 \times 1008 pixels) was used to illuminate the soap film. Images ($4.5 \times 4.5 \text{ cm}^2$) were acquired at the center of the soap film at 30 fps, yielding typically 10^4 vectors per velocity field.

Fig. 7 (a) is the velocity field without polymer. In this case, velocity strongly fluctuates in space, and the root mean squared velocity $v_{rms} \sim 13 \text{ cm/s}$. The velocity field has eddies of diverse sizes and small eddies embedded in a large eddy. This feature indicates the inverse energy cascade. On the contrary, in Fig. 7 (b) with polymer of concentration 24 ppm, velocity fluctuations are suppressed. There are lots of small eddies. This implies that the energy transfer to large scales is blocked in the presence of small amounts of polymer.

In the following discussion, five different polymer concentrations $\phi = 0, 3, 9, 12, 24$ ppm were used and the energy injection rate $\varepsilon_{inj} = 201.35 \text{ cm}^2/\text{s}^3$ was kept fixed by maintaining a constant V across the film. Figure 8 shows a set of 2nd-order structure functions $S_2(l) = \langle \delta v_l^2 \rangle$ measured using different ϕ , where δv_l is the longitudinal velocity difference on scale l , and $\langle \dots \rangle$ means the ensemble average. We found that in all cases there is a well-developed enstrophy range ($l < l_{inj}$) where $S_2(l) \propto l^{1.8 \pm 0.2}$. This scaling relation agrees reasonably well with the theoretical prediction $S_2(l) \propto l^2$ and persists down to the smallest scale ($\sim 300 \mu\text{m}$) resolvable by the PIV. Aside from small changes in the amplitude, the polymer appears to have no effect on this scaling behavior. For large scales ($l > l_{inj}$), two classes of behaviors can be identified: (a) For $0 < \phi < 10$ ppm, $S_2(l)$ increases with l and is reminiscent of an inverse energy cascade. Despite a large Taylor-microscale Reynolds num-

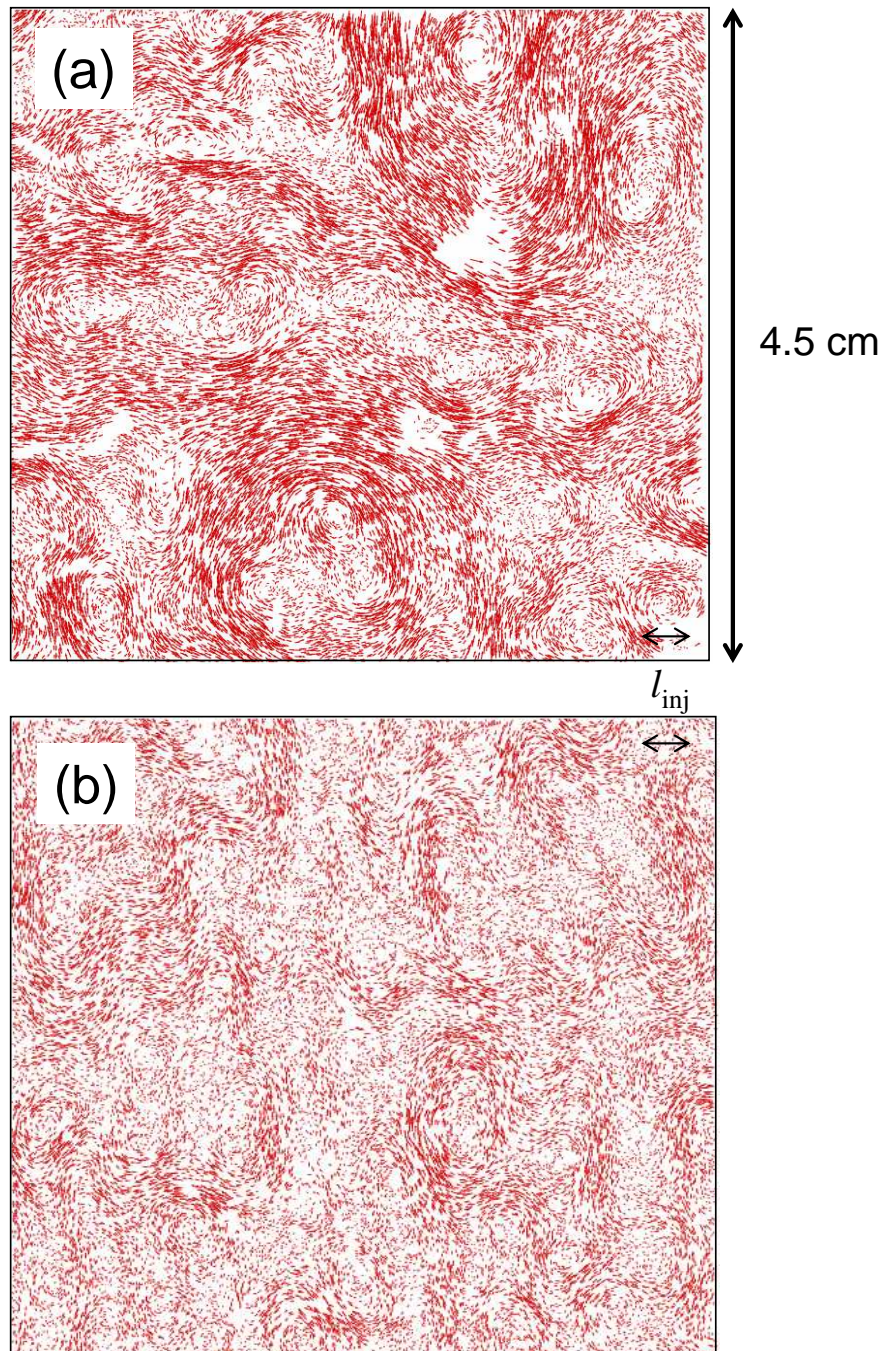


Figure 7: The velocity fields without polymer (a) and with polymer (b) of concentration 24 ppm.

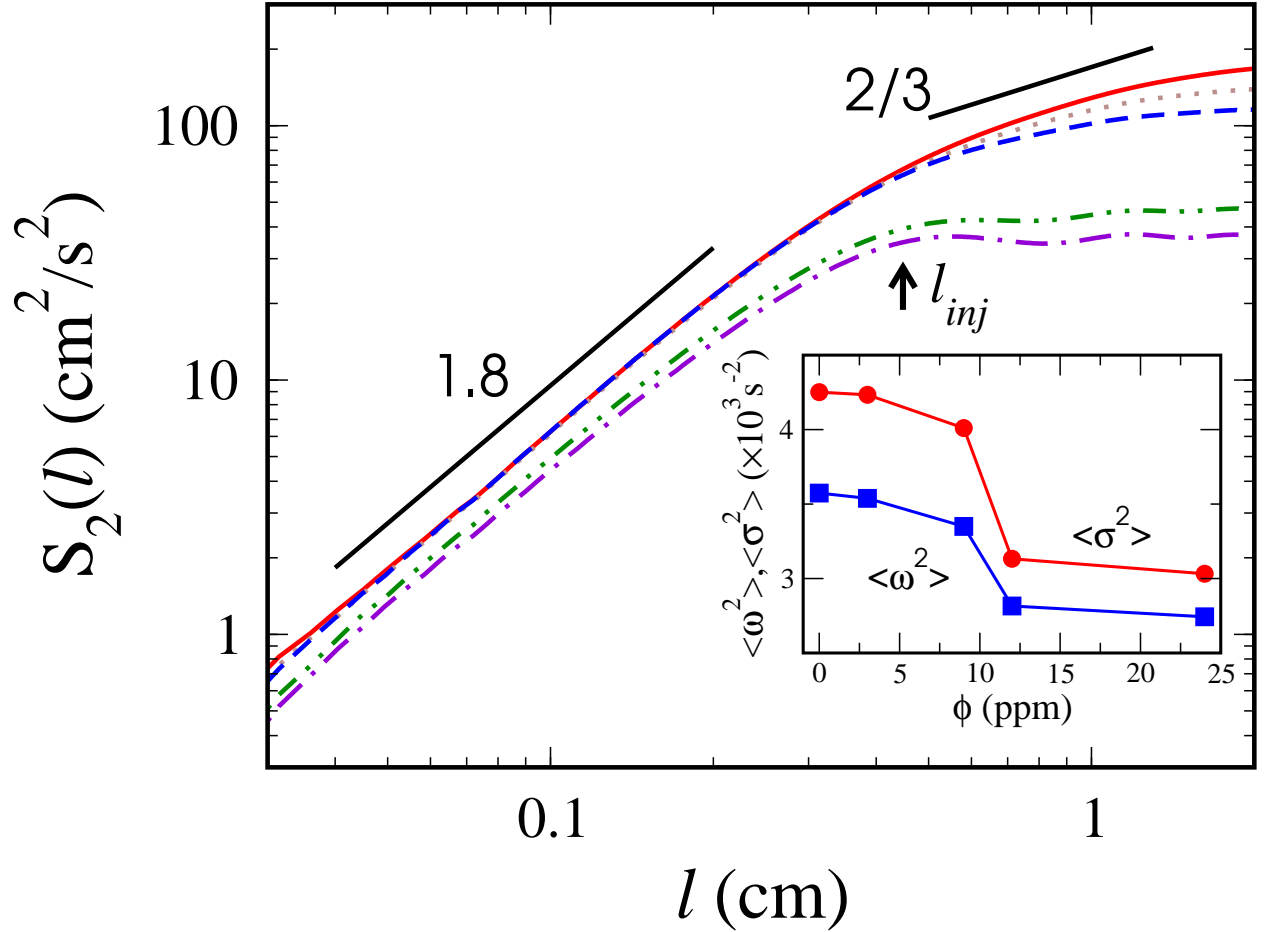


Figure 8: The 2nd-order structure function $S_2(l)$. l_{inj} denotes the energy injection length. In increasing order of turbulence intensity, the curves correspond to $\phi = 24, 12, 9, 3$ and 0 ppm. The inset is the plot of $\langle \sigma^2 \rangle$ (circles) and $\langle \omega^2 \rangle$ (squares) vs. ϕ (see text for details).

ber $Re_\lambda \simeq 152$, the Kolmogorov-like scaling $S_2(l) \propto l^{2/3}$ was not clearly observed due to the limited inertial range. In spite of this shortcoming, the magnitude of $S_2(l)$ was observed to decrease as ϕ was increased. (b) For $\phi > 10$ ppm, $S_2(l)$ becomes flat for $l > l_{inj}$, indicating the truncation of energy transfer to these large scales. The inhibition of the energy transfer to large scales can also be seen by the decreasing total kinetic energy $v_{rms}^2/2$, which is the asymptotic value of $S_2(l)$ for $l \gg l_{inj}$. Figure 8 shows that $v_{rms}^2/2$ drops sharply for $\phi \geq 10$ ppm.

The abrupt change of turbulent behavior when ϕ increases is suggestive, indicating that there may be a critical polymer concentration ϕ_C ($\simeq 10$ ppm) for quenching turbulence. The observation prompted us to examine other signatures that may be used to quantify the effect. One of the prominent features of 2D turbulence is the coherent structures, such as the centers where the vorticities are dominant, and saddle points where the strain rates are dominant in the flow. In a previous study [47], we investigated the distribution of centers and saddles via the quantity $\Lambda = \frac{1}{2}(\omega^2 - \sigma^2)$, which is related to the pressure by $\nabla^2 p = \Lambda$. Here $\omega^2 = \frac{1}{2} \sum_{i,j} (\partial_i v_j - \partial_j v_i)^2$ and $\sigma^2 = \frac{1}{2} \sum_{i,j} (\partial_i v_j + \partial_j v_i)^2$ characterize the center and the saddle structures in the flow, respectively. If $\Lambda > 0$, statistical distributions of ω^2 and σ^2 were measured for different ϕ and their probability density functions (PDF) are displayed in Fig. 9. It is shown that for $\phi < \phi_C$, $P(\omega^2)$ and $P(\sigma^2)$ are unaffected by ϕ , but they become significantly narrower for $\phi > \phi_C$, indicating that strong centers and saddles are suppressed. The effect is represented by the inset of Fig. 8 where $\langle \sigma^2 \rangle$ and $\langle \omega^2 \rangle$ vs. ϕ are plotted. We noted that in all cases of different ϕ , the ‘‘topological charges Λ ’’, averaged over space, are not strictly conserved. The differences between $\langle \sigma^2 \rangle$ and $\langle \omega^2 \rangle$ result from the film being slightly compressible ($\sim 10\%$). Since polymers are mostly deformed by saddles, it is instructive to compare the distribution of the strain rate σ with the Zimm relaxation time of the polymer. For our system with $\eta \simeq 0.02$ cP and $R_g \simeq 0.4$ μm , we found $\tau \simeq 16$ ms or $1/\tau^2 \simeq 3.91 \times 10^3$ s $^{-2}$, which is delineated as the vertical line in Fig. 9(a). A simple calculation shows that for $\phi < \phi_C$, $\sim 38\%$ of saddle points satisfy the time criterion ($\sigma\tau > 1$), and this fraction drops to $\sim 29\%$ for $\phi > \phi_C$. We also noted that the vertical line coincides approximately with the point where the two groups of PDFs cross each other. The

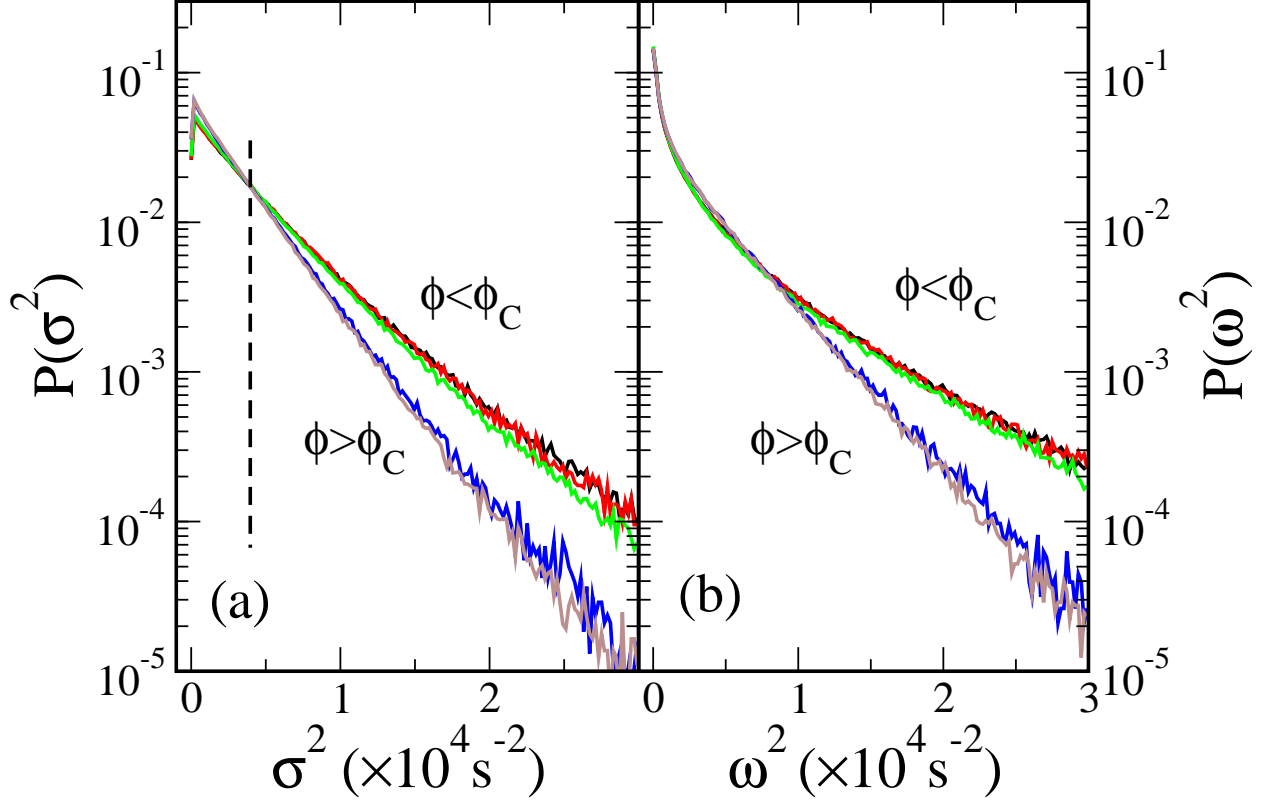


Figure 9: The PDFs of squared strain rate $P(\sigma^2)$ (a) and squared vorticity $P(\omega^2)$ (b). For $\phi < \phi_C \simeq 10$ ppm, the PDFs are nearly identical but for $\phi > \phi_C$, the PDFs become narrower. The vertical line in (a) corresponds to the square of the Zimm relaxation rate τ^{-2} .

significance of this observation is discussed in the summary. A weakened saddle distribution must be accompanied by a weakened vorticity distribution since $\langle \sigma^2 \rangle \sim \langle \omega^2 \rangle$. This is clearly delineated by Fig. 9(b).

To quantitatively assess the fraction of injected energy ε_{inj} that is ultimately transferred to the polymer's degrees of freedom and how this fraction changes with ϕ , we measured the overall energy budget of the system. The E&M cell is well suited for this task since the full velocity field can be measured using the PIV, allowing various energy rates to be calculated. To start with, in absence of polymer, we used the Kármán-Howarth relation leading to a linear scaling relation for the third-order velocity correlation function:

$$\begin{aligned} \frac{\partial}{\partial t} \langle u_i u'_j \rangle &= \frac{\partial}{\partial r_s} \langle u_i u'_s u'_j - u_i u_s u'_j \rangle - \frac{1}{\rho} \left[-\frac{\partial}{\partial r_i} \langle p u'_j \rangle + \frac{\partial}{\partial r_j} \langle p' u_i \rangle \right] \\ &+ 2\nu \frac{\partial^2}{\partial r_s^2} \langle u_i u'_j \rangle + \langle u'_j F_i \rangle + \langle u_i F'_j \rangle - 2\alpha \langle u_i u'_j \rangle, \end{aligned} \quad (2.1)$$

where α is the air drag coefficient, the subscript s means the s th component of the coordinates, and the prime and unprimed quantities correspond to locations $\vec{x} + \vec{r}$ and \vec{x} , respectively. Due to the steady-state condition, the l.h.s. vanishes. For the inertial range, the viscosity term may also be ignored. Since the Lorentz force is in the x-direction as shown in Fig. 6, the above equation can be further simplified if only the y component is evaluated. This yields:

$$\frac{\partial}{\partial r_s} \langle u_y u'_s u'_y - u_y u_s u'_y \rangle - \frac{1}{\rho} \left[-\frac{\partial}{\partial r_y} \langle p u'_y \rangle + \frac{\partial}{\partial r_y} \langle p' u_y \rangle \right] = -2\alpha \langle u_y u'_y \rangle \quad (2.2)$$

All the terms in this equation can be evaluated from the measured velocity field. In particular, the pressure field can be solved based on the equation $\nabla^2 p(\vec{x}) = -\Lambda(\vec{x})$ using a Fourier method under the incompressible and isotropic condition. Figure 10(a) shows the l.h.s. (L_{yy} , circles) and the r.h.s. (R_{yy} , lines) of Eq. (2.2) for $\phi = 0$. It is found that in the absence of polymer, the two sides are matched if $\alpha = 0.7 \text{ s}^{-1}$. In contrast, if the same calculation is carried out for $\phi = 12 \text{ ppm}$ as in Fig. 10(b), there is a significant discrepancy between the l.h.s. and the r.h.s. of Eq. (2.2). Such discrepancy is expected because the polymer-fluid interaction is not included in the equation.

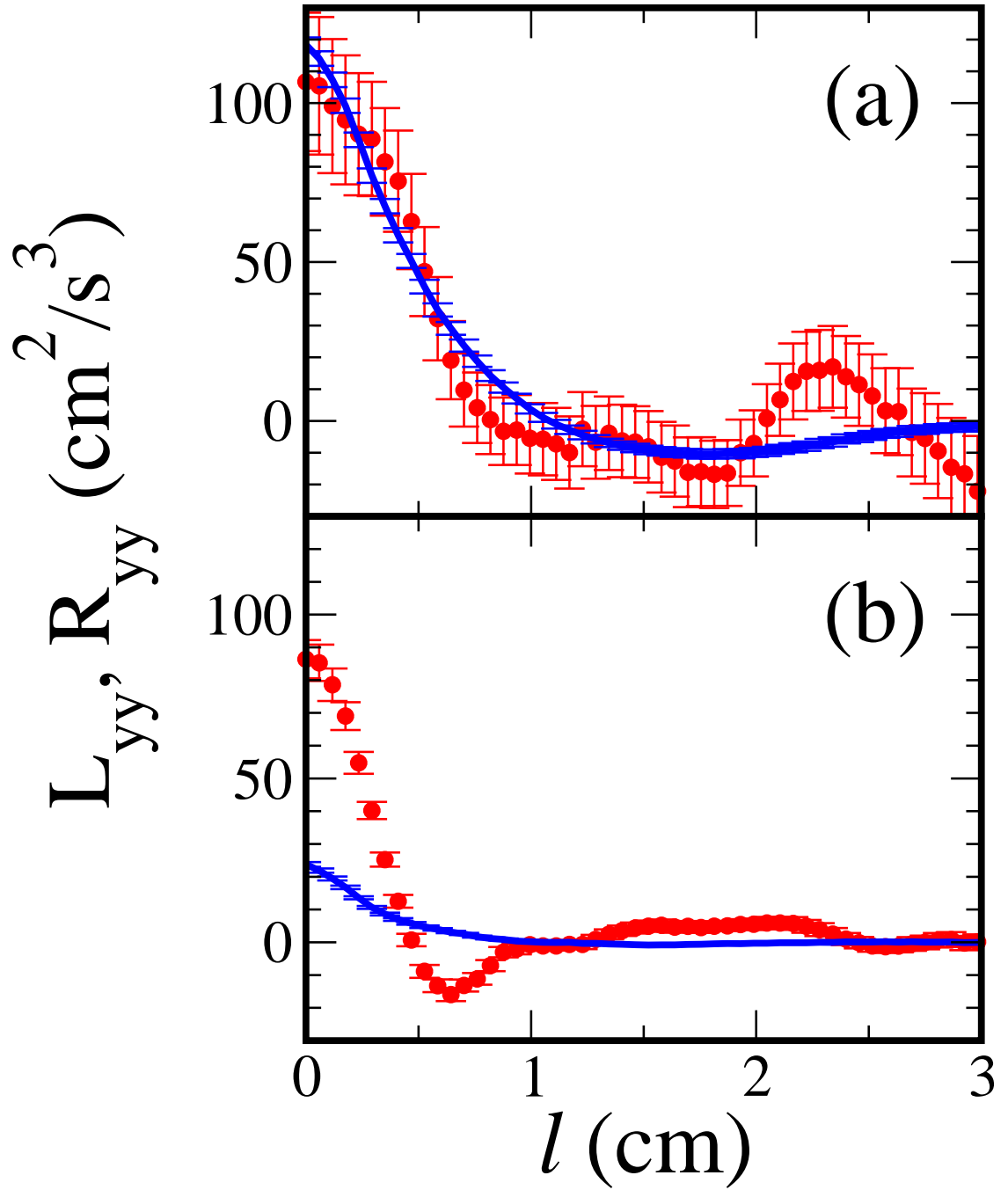


Figure 10: Comparison between the l.h.s. (L_{yy} , circles) and the r.h.s (R_{yy} , lines) of Eq. (2.2) for $\phi = 0$ (a) and for $\phi = 12$ ppm (b). The air friction coefficient $\alpha \simeq 0.7$ s⁻¹ is used in both cases.

In the single-point limit ($\vec{r} \rightarrow 0$), Eq. (2.2) gives the energy balance [36]:

$$\varepsilon_{inj} = \varepsilon_\nu + \varepsilon_\alpha + \varepsilon_p, \quad (2.3)$$

where the energy injection rate $\varepsilon_{inj} = \langle u_x F_x \rangle$ (see Fig.6) and the energy dissipation rates due to fluid viscosity $\varepsilon_\nu = \nu \langle \sigma^2 \rangle$ and due to air friction $\varepsilon_\alpha = \alpha \langle v^2 \rangle$ are all standard definitions and can be evaluated. The rate of energy uptake by the polymer ε_p is included and will be found by measurements. In the experiment, ε_{inj} was kept constant whereas ε_ν and ε_α were measured by varying ϕ . Figure 11 summarizes the result: for $\phi = 0$, $\varepsilon_\nu \simeq 57 \text{ cm}^2/\text{s}^3$ and $\varepsilon_\alpha \simeq 144 \text{ cm}^2/\text{s}^3$, yielding $\varepsilon_{inj} \simeq 201 \text{ cm}^2/\text{s}^3$. The fact that $\varepsilon_\alpha > \varepsilon_\nu$ is consistent with the physical picture that the injected energy is predominantly transferred to large scales $l > l_0$. Here $l_0 \simeq (\varepsilon_{inj}/\alpha^3)^{1/3}/8 \simeq 3 \text{ cm}$ is the outer scale of turbulence and is where $S_2(l)$ levels off (see Fig. 8) [49]. An appreciable amount of energy ($\sim 30\%$) is also transferred to small scales and consumed by viscosity. In the absence of polymer, this partition of energy on small and large scales is consistent with a previous study [48]. It is interesting to note that when ϕ is increased, the fraction of energy consumed by the fluid viscosity remains almost constant (see the heights of the dark-hatched area in Fig. 11(a)) until ϕ crosses ϕ_C , where ε_ν suffers a jump of $\sim 28.7\%$. The effect is more dramatic for the energy transfer to large scales as indicated by the heights of the light-hatched area in the same figure. Here one observes that ε_α keeps decreasing with ϕ and drops precipitously at ϕ_C . Such a strong ϕ dependence is due to the significant change in v_{rms} when the polymer was introduced into the flow as seen in Fig. 8. Since ε_{inj} is constant, it follows that more energy is sequestered by the polymer's elastic deformation, and ε_p increases markedly around ϕ_C as delineated by the heights of white area in Fig. 11(a).

The above measurement shows that for a given ε_{inj} , there exists a sharp change in the turbulence behavior when ϕ crosses ϕ_C . Is the converse true? To find out, we conducted an experiment in which $\phi = 15 \text{ ppm}$ was fixed but ε_{inj} was varied by changing the applied voltage ($46 < V < 65 \text{ volts}$). For comparison, an independent run was also carried out with $\phi = 0$. Figure 11(b) shows that in the absence of polymers, the turbulent intensity characterized by the v_{rms} is a smooth increasing function of V . When the polymer is present, the situation is somewhat different; v_{rms} increases initially, levels off, and then increases again. It forms

a plateau for a small range of V between 50 and 55 volts. This measurement suggests that there exist two thresholds V_{C1} and V_{C2} marked by two arrows in the figure. We believed that the lower threshold V_{C1} corresponds to the onset of the turbulent suppression and the higher threshold V_{C2} corresponds to the saturation of the elastic field. However, for the entire range of V , the measured energy transfer rate ($\propto \langle \delta v_l^3 \rangle$) remains positive, indicating an inverse energy cascade but with a reduced transfer rate when the polymer is present.

2.3 CONCLUSION

To summarize, the polymer effects on forced 2D turbulence in freely-suspended soap films were investigated quantitatively using two independent control parameters ϕ and ε_{inj} . The turbulent flow we measured is free from the boundary of the system so that all polymer effects on turbulence come from the bulk of the flow. The measurement shows that when ε_{inj} is fixed, turbulent suppression has a sharp threshold $\phi_C (\simeq 10 \text{ ppm})$. However, when ϕ is fixed, two thresholds can be identified, but the transitions in this case are much weaker. We found that turbulent suppression occurs concurrently with the elimination of strong saddles. Inspection of Fig. 9(a) reveals that those saddles that are eliminated have strength determined precisely by the relation $\sigma^2 1/\tau^2$, indicating that the time criterion is strictly obeyed in the experiment. Since polymer-turbulence interactions are primarily via saddles and the weakening of saddles by polymer stretching has the drastic effect of quenching turbulence, it is suggested that this hydrodynamic structure may play a role in transferring energy from scale to scale. It remains an intriguing possibility that the same mechanism operates in 3D as well as in 2D turbulence.

3.0 INTERMITTENCY ON LARGE SCALES

It is generally believed that two-dimensional turbulence is immune to intermittency possibly due to the absence of vortex stretching. However, in turbulence created in a freely suspended soap film by electromagnetic forcing, it is found that intermittency is not insignificant. We draw this conclusion based on the measured velocity structure function $S_p(l) (\equiv \langle |\delta v_l|^p \rangle) \propto l^{\zeta_p}$ on scales l greater than the energy injection scale l_{inj} . The scaling exponent ζ_p vs. p deviates from the expected linear relation and reveals intermittent behavior comparable to that observed in fully developed 3D turbulence in wind tunnels. Our measurements demonstrate that intermittency can be accounted for by the non-uniform distribution of saddle points in the flow. Also, we present an alternate analysis of intermittency by the geometrical multifractal method for two-dimensional turbulent flow. An analysis of the averaged energy dissipation rate clearly shows that 2D turbulence has a multifractal behavior and its probability distribution function is close to a lognormal distribution.

3.1 INTRODUCTION

Existing experiments [41] and theory [33] suggest that 2D turbulence on large scales represents a peculiar state of matter that is not far from thermal equilibrium. This is surprising because the system is dissipative and strongly driven by an external source. The experimental evidence derives from the remarkable observation of Paret and Tabeling who showed that in 2D turbulence created in a shallow layer of electrolyte, the energy spectrum $E(k)$ exhibits a $k^{-5/3}$ law, whereas the probability density function (PDF) $P(\delta v_l)$ of the velocity difference on scales l is, to a good approximation, a Gaussian function [41]. This measurement suggests that the energy transfer rate, which is proportional to the skewness of $P(\delta v_l)$, is weak compared to its 3D counterparts and may be the cause of weak intermittency. It has been recently postulated by L'vov *et al.* [38] that this interesting behavior may be intimately connected with the presence of a special dimension ($d_C = 4/3$) in which the $k^{-5/3}$ law holds but the enstrophy flux is strictly zero. Thus, the dynamics of the system are governed by the equipartition of enstrophy. They further argued that $d = 2$ is not too remote from d_C and the Gaussian statistics still prevail. It thus comes as a surprise that in our 2D soap film driven by electromagnetic forcing, the intermittency is not negligible as anticipated. If we characterize the strength of intermittency in terms of $\mu (\equiv 2\zeta_3 - \zeta_6)$, μ is only a factor of two smaller than that in fully-developed 3D turbulence [2]. Here ζ_p is defined by the p th-order longitudinal velocity structure function $S_p(l) (\equiv \langle |\delta v_l|^p \rangle \equiv \langle |(\vec{v}(\vec{x} + \vec{l}) - \vec{v}(\vec{x})) \cdot \hat{l}|^p \rangle) \propto l^{\zeta_p}$. Kolmogorov predicted $\zeta_p = p/3$ in 1941, but due to nonuniform distribution of the coarse-grained energy dissipation rate ε_l^{dis} , ζ_p is a nonlinear function of p . In an effort to identify the source of intermittency, $S_p(l)$ is compared with the moments of the coarse-grained energy dissipation rate ε_l^{dis} on scales l using the Kolmogorov refined similarity hypothesis (K62) [32]. It is unclear at the outset whether K62 is applicable to 2D turbulence on large scales because the energy transfer mechanism is entirely different in 2D than in 3D. However, our measurements show that K62 in its original form works rather well for all moments up to $p = 9$. This implies the coarse-grained energy transfer rate ε_l^t is proportional to the coarse-grained energy dissipation rate ε_l^{dis} in the inertial range ($l_{inj} \leq l \leq l_o$), and both may be connected with the saddle structures in the flow. Here l_{inj} and l_o are the energy injection

and the outer scale of turbulence, respectively.

3.2 EXPERIMENTAL RESULTS

The experiment was carried out in a freely suspended horizontal soap film driven by electromagnetic forcing as mentioned in chapter 2. The only differences are that the magnet size is smaller with $a = 0.25$ cm corresponding to the injection scale $l_{inj} = 2a/\sqrt{3} = 0.29$ cm, and the current I oscillates at 1 Hz instead of 3 Hz.

Figure 12(a) shows an overlaid image of the velocity $\vec{v}(\vec{x})$ and the enstrophy $\omega(\vec{x})^2 = \sum_{i,j}(\partial_i v_j - \partial_j v_i)^2/2$ fields. An interesting feature of the image is that the enstrophy is concentrated in patches, and strong long-lived vortices are nearly axially symmetric. The weak vortices, on the other hand, are susceptible to be torn by the straining motion of the flow and are elongated. Figure 12(b) is for the same $\vec{v}(\vec{x})$ field, but the squared strain rate or the saddle point $\sigma(\vec{x})^2 = \sum_{i,j}(\partial_i v_j + \partial_j v_i)^2/2$ is plotted. By definition, the local viscous dissipation is given by $\varepsilon(\vec{x}) = \nu\sigma(\vec{x})^2$, where ν is the viscosity of the film. The figure shows that the distribution of $\sigma(\vec{x})^2$ is different from that of $\omega(\vec{x})^2$; the saddles are more connected and populated between vortices. An ensemble of $\vec{v}(\vec{x})$ such as this one allows us to calculate various statistical quantities of 2D turbulence. Of particular interest is the velocity structure function $S_p(l)$ and its relation to the locally averaged saddles or equivalently the local dissipation rate:

$$\varepsilon_l^{dis}(\vec{x}) \equiv \frac{4}{\pi l^2} \int_{|\vec{x}-\vec{x}'|\leq l/2} \varepsilon(\vec{x}') d\vec{x}' \quad (3.1)$$

where \vec{x}' is the center of the circular box of radius $l/2$.

Among different moments, $S_2(l)$ and $S_3(l)$ hold special significance. The 2nd moment represents the energy distribution on different scales. In our experiment, the shape of $S_2(l)$ is sensitive to the forcing frequency, possibly due to a competition between time scales of forcing and the energy transfer. For high frequencies ($f \geq 3$ Hz), $S_2(l)$ is not a power law of l for $l > l_{inj}$, regardless of the magnitude of forcing. For lower frequencies ($f \sim 1$ Hz), on the other hand, a limited scaling range emerges. Figure 13(a) displays the measurements with $f = 3$ (circles, $Re_\lambda=80$) and 1 Hz (squares, $Re_\lambda=167$), respectively. One observes

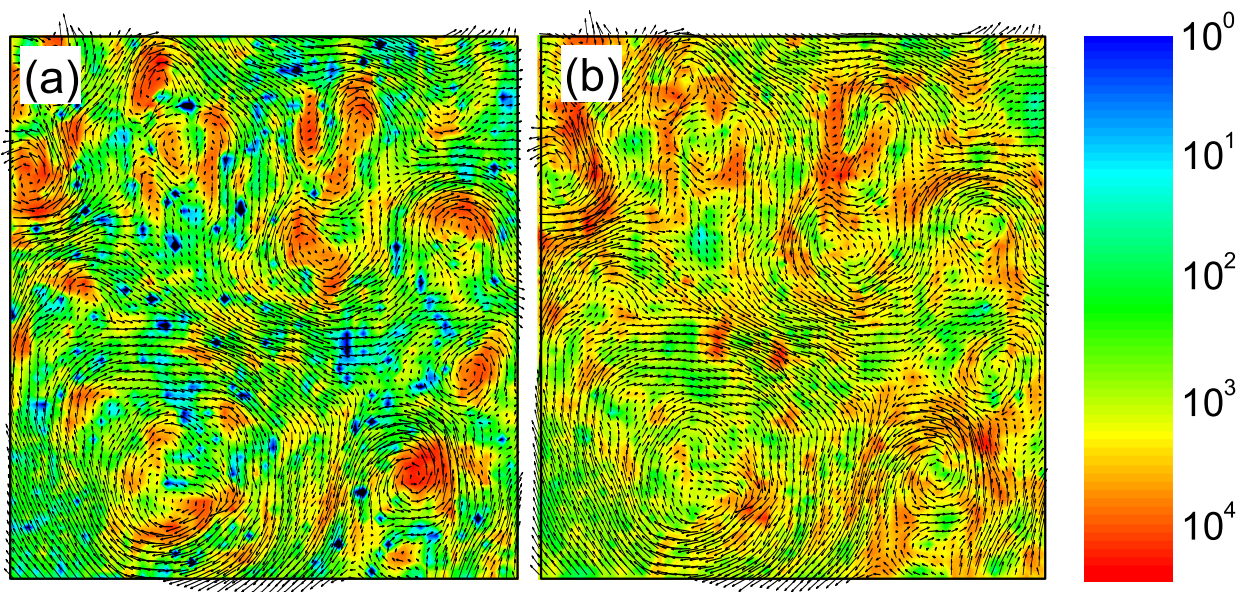


Figure 12: (a) The velocity field $\vec{v}(\vec{x})$ (arrows) and the enstrophy $\omega^2(\vec{x})$ field (color rendered). (b) The velocity field $\vec{v}(\vec{x})$ (arrows) and the square of strain $\sigma^2(\vec{x})$ field (color rendered). The image size is $4 \text{ cm} \times 4 \text{ cm}$.

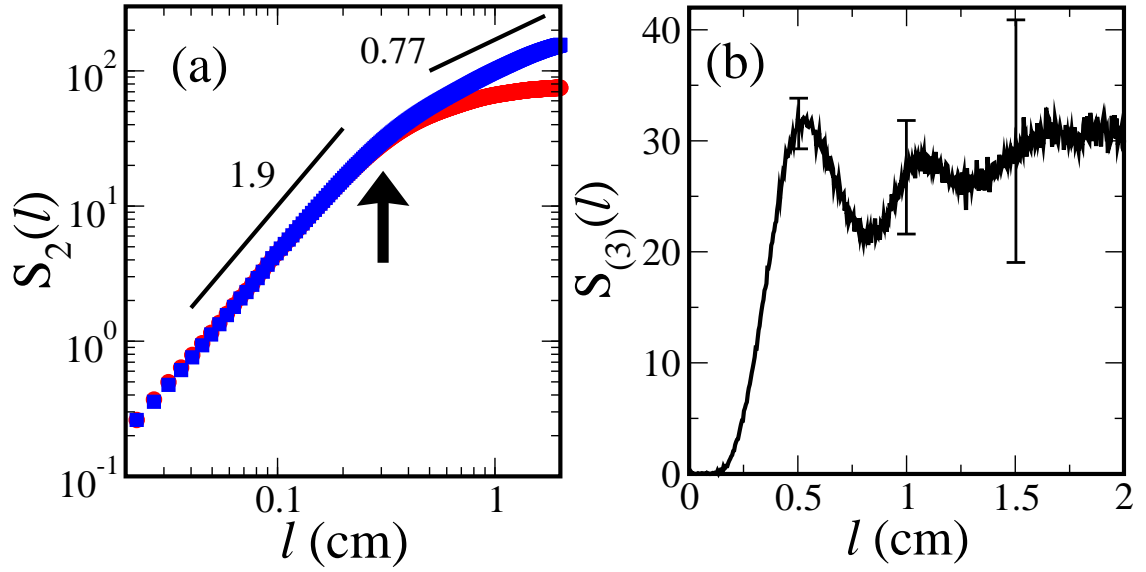


Figure 13: (a) The 2nd-order δv_l structure function $S_2(l)$ measured with $f = 1\text{Hz}$ (blue, $\text{Re}_\lambda = 167$) and 3 Hz (red, $\text{Re}_\lambda = 80$). The injection scale l_{inj} is marked by the vertical arrow and the outer scale $l_o \simeq 2\text{ cm}$. (b) The 3rd-order δv_l structure function $S_{(3)}(l)$ measured with $f = 1\text{Hz}$ (blue in (a), $\text{Re}_\lambda = 167$).

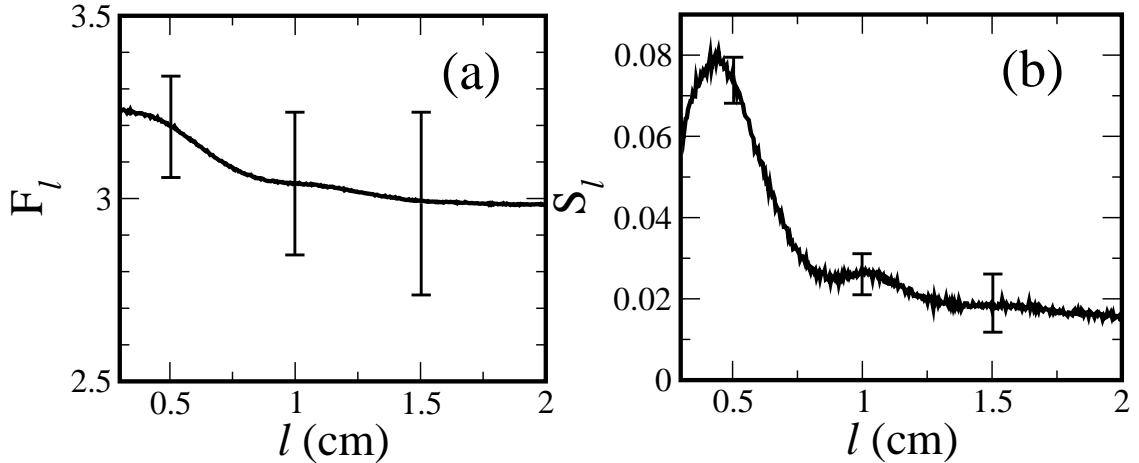


Figure 14: The flatness F_l of $P(\delta v(l))$ (a) and the skewness S_l of $P(\delta v(l))$ (b) with $Re_\lambda = 167$ and $f = 1$ Hz.

that although both data display a well-developed enstrophy subrange, $S_2(l) \propto l^{1.9 \pm 0.1}$, the large-scale behavior is entirely different. For 1 Hz, $S_2(l) \propto l^{2.3/3}$ over about half a decade in l . The scaling exponent is 15% greater than the theoretically predicted $2/3$ and was found to depend on Re_λ systematically, *i.e.*, $\zeta_2 \simeq 0.67 \pm 0.07$ for $Re_\lambda = 110.3$ and increases to $\zeta_2 \simeq 1.0 \pm 0.1$ for $Re_\lambda = 212.1$. Similar to $S_2(l)$, the third moment $S_{(3)}(l)$ was also found to deviate from the theoretical prediction ($S_{(3)}(l) \sim l$) as shown in Fig. 13(b), where the subscript (3) stands for the moment calculated *without* the absolute sign. Here one observes that $S_{(3)}(l)$ is not linear in l but oscillates in space due to the spatially periodic forcing in the experiment. This spatial anisotropy however was not observed in the even moments $S_p(l)$. $S_{(3)}(l)$ is positive at all scales, showing that the direction of energy transfer is from small to large scales and is consistent with the inverse energy cascade of 2D turbulence.

The low-order statistics observed in our experiment are in reasonably good agreement with Paret's measurements [41] and with the numerical simulation [9]. For instance, (i) the overall skewness $S_l = S_{(3)}(l)/S_2(l)^{3/2}$ displayed in Fig. 14(b) is rather small; it is $\sim 8\%$ near l_{inj} and decreases to $\sim 2\%$ for large scales. The averaged value over the inertial range is $\bar{S} = l^{-1} \int_{l_{inj} < l < l_o} S(l) dl = 0.03 \pm 0.02$. This is to be compared with the skewness of 5% seen in

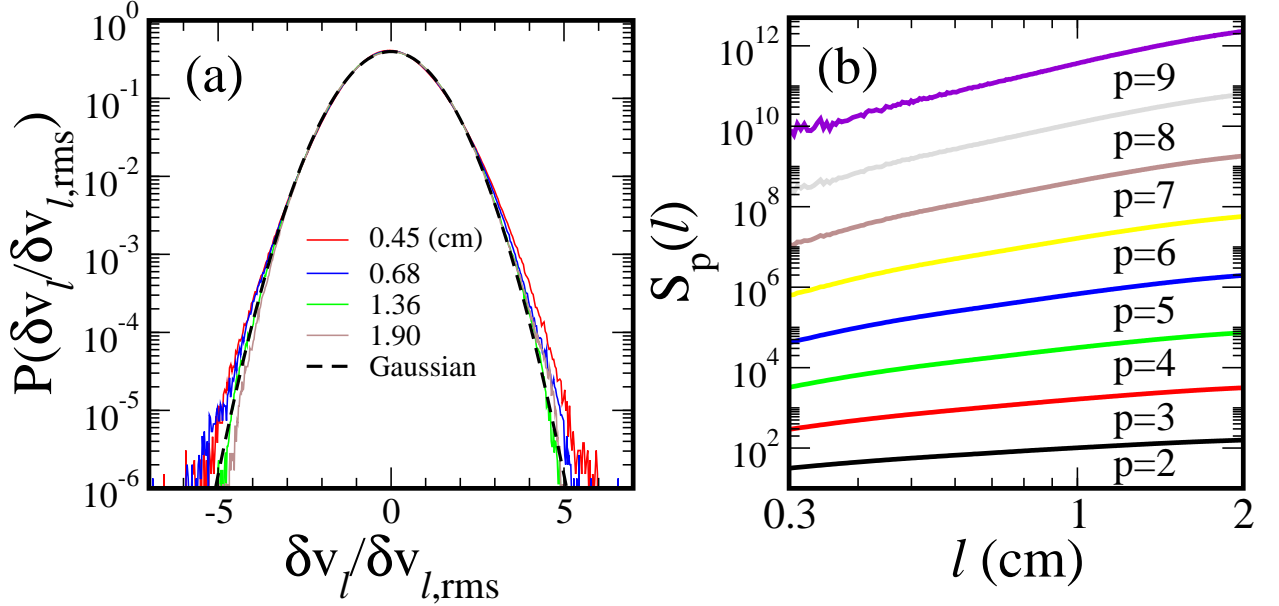


Figure 15: (a) The normalized PDFs of δv_l for various scales. (b) $S_p(l)$ vs. l .

Paret's experiment and 3% in the simulation. (ii) Similar to S_l , the flatness $F_l = S_4(l)/S_2(l)^2$ in Fig. 14(a) is not constant but varies from 3.25 near l_{inj} to 3.0 for large scales. The average value $\bar{F} = l^{-1} \int_{l_{inj} < l < l_o} F(l) dl = 3.1$ agrees well with the Gaussian value of 3. It should be emphasized that although \bar{S} and \bar{F} are reasonably consistent with the Gaussian statistics, this does not imply that higher order statistics need to be so. As the order p increases, rare events associated with the tails of the PDFs (see Fig. 15(a)) become more prominent. Since these rare events are l dependent, ζ_p must be a nonlinear function of p .

In Fig. 15(a), the normalized PDF of δv_l on various scales $l = 0.45, 0.68, 1.36$ and 1.90 cm are plotted. As can be seen, the central part of the PDFs can be fit well by a Gaussian distribution function (the dashed line), but systematic deviations are found in the wings of the PDFs, particularly for small l . Each PDF consists of more than 5×10^6 data points; the size of the data sets is thus comparable to 3D experiment in a wind channel [2]. Using the ranking order or the Zipf distribution of δv_l [18], it is possible to estimate the highest moment $S_{p_{max}}(l)$ that can be calculated from a given data set. In our case, the highest order turns out to be $p_{max} \sim 9$, which is smaller than $p_{max} = 12$ (2D) [41] and 14 (3D) [2] in

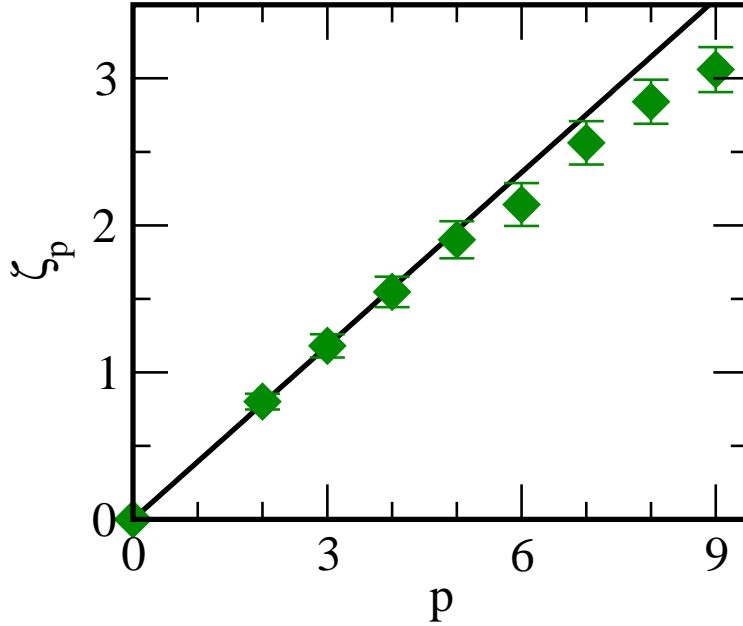


Figure 16: The scaling exponent ζ_p as a function of p . The slope of the solid line is ~ 1.2 .

earlier investigations. Figure 15(b) displays a set of $S_p(l)$ for $l > l_{inj}$. As shown, all moments scale as $S_p(l) \propto l^{\zeta_p}$. Although the scaling range is limited, the exponents ζ_p nonetheless can be extracted from the slopes of individual curves. This is delineated as diamonds in Fig. 16. If 2D turbulence is non-intermittent as suggested, ζ_p would be a linear function of p . This is not the case in our experiment; ζ_p bends for $p > 4$ and its initial slope of $1.2/3$ is greater than $1/3$ as shown by the solid line. The bending of ζ_p indicates that the velocity field in soap-film turbulence is intermittent, and the large initial slope suggests that the Kolmogorov-like scaling cannot apply to our system.

To obtain the Kolmogorov-like scaling exponent and to compare our experiment with previous investigations [41, 2], which have $\zeta_3 = 1$, the relative scaling exponents are obtained by using an extended self-similarity (ESS) hypothesis. This is based on K41 or $S_3(l) \sim l$. According to the hypothesis, the p th order structure function $S_p(l)$ scales as the third order structure function $S_3(l)$ as $S_p(l) \sim S_3(l)^{\zeta_p/\zeta_3}$. Fig 17 shows an example of ESS at $v_{rms} = 13.1$ cm/s. The slopes on this log-log plot yield the relative scaling exponent ζ_p/ζ_3

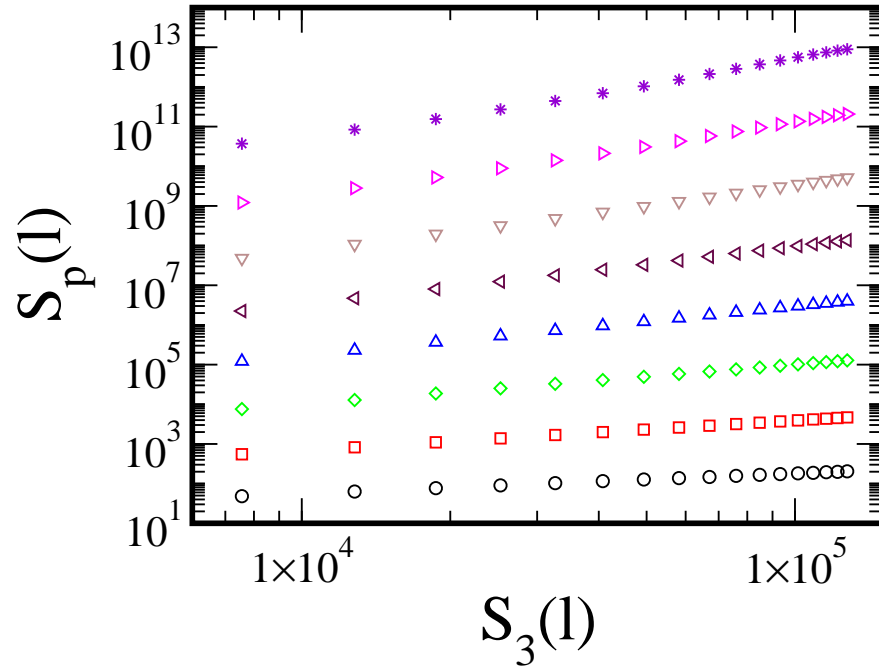


Figure 17: The log-log plot of $S_p(l)$ as a function of $S_3(l)$ at $\text{Re}_\lambda = 212$. ESS tells that $S_p(l)$ scales as a function of $S_3(l)$ so that each plot is an increasing linear function. From bottom to top: $p = 1$ to 8.

for different p . Another way to obtain the relative scaling exponents is as follows: We plot the ratio of the derivatives $\frac{d\ln(S_p(l))}{d\ln(l)} / \frac{d\ln(S_3(l))}{d\ln(l)}$ as a function of l . Here this ratio is approximately constant (data not shown) over a broader range of l and its averaged value $\overline{\zeta_p/\zeta_3} (= \overline{\frac{d\ln(S_p(l))}{d\ln(l)} / \frac{d\ln(S_3(l))}{d\ln(l)}}$) over the inertial range could be better determined than individual ζ_p [3]. The data is presented as squares in Fig. 18. In our experiment, the two methods yield essentially the same result, $\overline{\zeta_p/\zeta_3} \simeq \zeta_p/\zeta_3$, as evidenced by the closeness of squares and diamonds in the main figure. In Fig. 18 we also plot the data for fully-developed 3D turbulence (triangle-downs) measured by Anselmet *et al.* [2] and the 2D data (triangle) by Paret [41]. As will be shown in the Discussion, if K62 is valid and ε_l obeys a lognormal distribution [23], the relative scaling exponent ζ_p/ζ_3 can be calculated explicitly with the result $\zeta_p/\zeta_3 = p/3 + (\mu/18\zeta_3)(3p - p^2)$, where $\mu (= 2\zeta_3 - \zeta_6)$ characterizes the width of the distribution of ε_l and is the only adjustable parameter. For our experiment, a fitting procedure yielded $\mu \simeq 0.11$. This value should be compared with $\mu \simeq 0.2$ for the 3D turbulence data [2] and $\mu \simeq 0.03$ for Paret's data [41].

We next turn our attention to find whether the observed intermittency can be accounted for in a similar fashion as K62 [32]. This hypothesis has been the cornerstone for understanding 3D turbulence, and it would be interesting to see if this important idea has any relevance to 2D turbulence. The basic observation in 3D turbulence is that velocity fluctuations possess a broad spectrum and that the globally averaged energy dissipation rate ε cannot account for rare, intense local fluctuations. One way to fix this statistical bias is to divide the spatial domain into a collection of boxes of size l , each characterized by a locally averaged energy dissipation rate $\varepsilon_l(\vec{x})$ as defined in Eq. (3.1). It was conjectured by Kolmogorov that for the inertial range of scales, the PDF of the stochastic variable $V = \delta v_l / (l\varepsilon_l)^{1/3}$ depends only on the local Reynolds number $\text{Re}_\lambda = \langle l\varepsilon_l \rangle^{1/3} / \nu$ and in the limit $\text{Re}_\lambda \gg 1$, the PDF is universal, independent of Re_λ . If one further assumes the statistical independence between the random variables V and ε_l [27], it follows that $S_p(l) \equiv \langle \delta v_l^p \rangle = \langle V^p \rangle \langle \varepsilon_l^{p/3} \rangle l^{p/3} = C_p l^{p/3 + \tau_{p/3}} = C_p l^{\zeta'_p}$, where C_p is a p -dependent constant, $\langle \varepsilon_l^p \rangle \propto l^{\tau_p}$ and $\zeta'_p = p/3 + \tau_{p/3}$. Thus, if K62 is valid, one expects $\zeta_p = \zeta'_p$ for all p . By using the ratio of moments $S_p(l)/S_3(l)^{p/3}$ instead of the moment itself, the K62 can be generalized and facilitates a better determination of scaling exponents. This is the essence of extended self-similarity and has been successfully applied

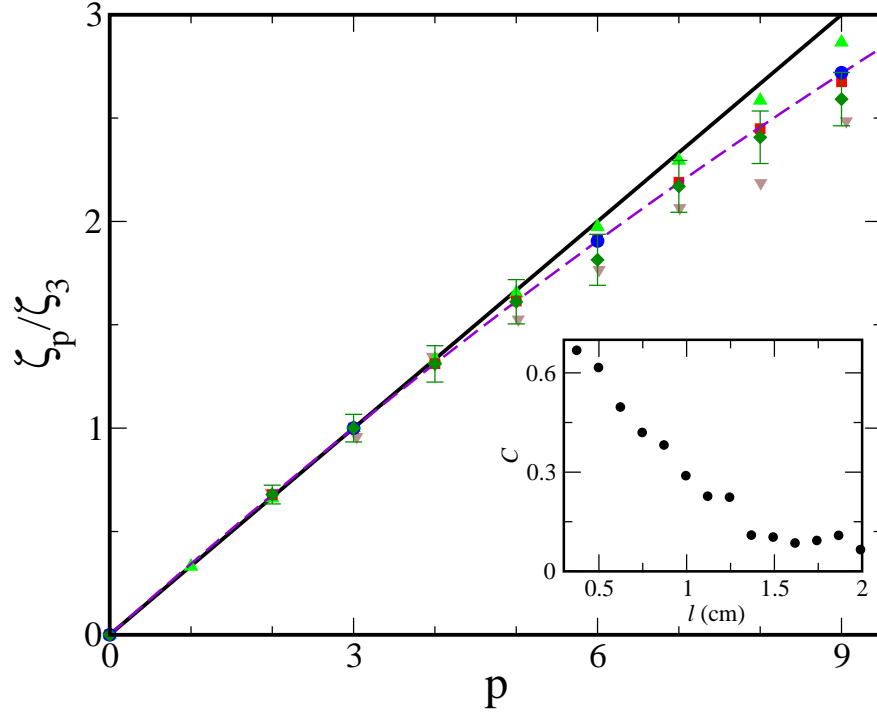


Figure 18: The main figure shows that (i) the relative scaling exponents ζ_p/ζ_3 (diamonds) and $\overline{\zeta_p/\zeta_3}$ (squares) measured using different methods are consistent, (ii) ζ_p/ζ_3 are also consistent with the local energy dissipation rate measurements $\phi(p)$ (circles), and (iii) the intermittency in the film is stronger than that seen in Ref. [41] (triangles) but weaker than in Ref. [2] (triangle-downs). The solid line is for $\zeta_p/\zeta_3 = p/3$ and the dash line is the lognormal-model fit to our data ($\mu \sim 0.11$). The inset displays the correlation coefficients between $|\widetilde{\delta v_l}|$ and ε_l' in the inertial range.

to turbulence with a low Re or with a nonclassical exponent ($\zeta_3 \neq 1$) [7]. It is readily shown that $\zeta_p/\zeta_3 = p/3 + \tau_{p/3}^*/\zeta_3$, where $\tau_{p/3}^* = \tau_{p/3} - (p/3)\tau_1$. If ε_l is distributed in a lognormal fashion, $\tau_1 = 0$ and $\tau_{p/3}^* = \tau_{p/3} = (\mu/18)(3p - p^3)$, where μ is the width of the $\ln(\varepsilon_l)$ distribution [23]. The above discussion shows that the reason ζ_p deviates from the linear p dependence is because of the non-trivial distribution of ε_l characterized by $\tau_{p/3}$. It should be emphasized that though K62 has gained considerable experimental and numerical support for 3D turbulence [43, 55, 27, 14], its implication for 2D turbulence remains unclear and is analyzed below.

A difficulty in applying K62 to 2D turbulence is that energy dissipation due to the fluid viscosity $\varepsilon_l^{dis} = \varepsilon_l^\nu (\equiv \nu \langle \sigma(\vec{x}')^2 \rangle_l)$ may not be entirely relevant to large-scale velocity fluctuations because energy flux is reversed. To our surprise, however, we found that δv_l and ε_l^ν are strongly correlated in soap films. The coefficient of correlation $C(l) = \langle (|\widetilde{\delta v_l}(\vec{x})| - \langle |\widetilde{\delta v_l}(\vec{x})| \rangle) \cdot (\varepsilon_l^\nu(\vec{x}) - \langle \varepsilon_l^\nu(\vec{x}) \rangle) \rangle / (s_{|\widetilde{\delta v_l}(\vec{x})|} s_{\varepsilon_l^\nu})$ is plotted in the inset of Fig. 18, where $\widetilde{\delta v_l}(\vec{x})$ is the averaged longitudinal velocity difference on the circumference of a randomly selected disk of diameter l , $\varepsilon_l^\nu(\vec{x})$ is the viscous dissipation inside the disk, $s_{|\widetilde{\delta v_l}(\vec{x})|}$ and $s_{\varepsilon_l^\nu}$ are their standard deviations, and the angular bracket is the volume plus the time average.

We observed that the correlation is about 70% near l_{inj} and decreases to about 10% for large l . This degree of correlation is on par with what was observed in the inertial range of 3D turbulence [43, 55, 27, 14]. We next proceeded to calculate energy dissipation statistics within disks of diameter l . The coarse-grained values of $\varepsilon_l^{dis}(\vec{x})$ are calculated according to Eq. (3.1) and the scaling exponents τ_p^* are evaluated based on an ensemble of disks. The resulting exponents, $\phi(p) \equiv p/3 + \tau_{p/3}^*/\zeta_3$, can thus be compared with the relative exponents ζ_p/ζ_3 calculated using δv_l . The scaling exponents $\phi(p)$, as shown by the solid circles in Fig. 18, are nearly identical to ζ_p/ζ_3 , indicating that intermittency in δv_l is consistent with the non-uniform distribution of ε_l^{dis} . For completeness, we also included the air drag $\varepsilon_l^\alpha \equiv \alpha \langle \vec{v}(\vec{x})^2 \rangle_l$ in the energy dissipation, $\varepsilon_l^{dis}(\vec{x}) = \varepsilon_l^\nu(\vec{x}) + \varepsilon_l^\alpha(\vec{x})$. Here we found that the scaling exponents τ_p^* are unaffected by the air contribution (data not shown), suggesting that intermittency observed in this experiment is due almost entirely to ε_l^ν . The weak air contribution is expected in the inertial range and is consistent with our earlier findings that air drag is significant only for $l > l_0$ [49].

It remains to be clarified the striking fact that the relative scaling exponent ζ_p/ζ_3 can be accounted for by intermittency in the locally averaged dissipation field $\langle(\varepsilon_l^{dis})^{p/3}\rangle \propto l^{\tau_{p/3}}$ with the result $\zeta_p/\zeta_3 \simeq p/3 + (\tau_{p/3} - (p/3)\tau_1)/\zeta_3$. The finding is surprising because in 2D turbulence most of the injected energy is transferred to large l instead of being dissipated in small l . Thus, the scaling behavior for the velocity difference δv_l on large scales should be determined by the energy transfer rate ε_l^t rather than the local energy dissipation rate ε_l^{dis} . However, using the Navier-Stokes equation with a forcing term \vec{F} , it can be shown that the energy transfer rate to large scales is given by $\varepsilon_l^t = \varepsilon_l^{inj} - \varepsilon_l^{dis}$, where $\varepsilon_l^{inj} = \langle \vec{F}(\vec{x}) \cdot \vec{v}(\vec{x}) \rangle_l$ is the energy injection rate. In particular, in the inertial range ($l_{inj} \leq l \leq l_0$), one expects $\varepsilon_l^t > 0$. Our observed scaling behavior therefore demands ε_l^t to be proportional to ε_l^{dis} or $\varepsilon_l^t = A\varepsilon_l^{dis}$, where $A > 0$ is a constant. In light of the energy budget, $\varepsilon_l^{inj} = (A+1)\varepsilon_l^{dis}$ in the inertial range. The above proportionalities ($\varepsilon_l^t \propto \varepsilon_l^{dis} \propto \varepsilon_l^{inj}$) make physical sense, and they imply that regions of large energy injection would on average dissipate more energy on small scales and at the same time transfer more energy to large scales. Indeed in 2D turbulence, longitudinal velocity fluctuations δv_l were found to correlate strongly with saddle points $\sigma^2(\vec{x})$ in the flow [16], which are responsible for energy dissipation as well as for energy transfer to large scales. In a recent study, we also found that when saddles are suppressed by polymers, inverse energy cascade is terminated [29]. Thus, even though turbulence in 2D and 3D is very different, both in hydrodynamic structures and in the mechanism of energy transfer, Kolmogorov's central idea of cascade, *i.e.* a dynamic equilibrium of energy flux $\delta v_l^3/l$ through δv_l fluctuations on the scale l and energy dissipation ε_l^{dis} within it, is remarkably preserved in two dimensions.

3.3 CONCLUSION

To summarize, we found velocity fluctuations in the inverse-energy-cascade subrange to be intermittent in 2D flowing soap films. The intermittency correlates strongly with coarse-grained saddle structures in the flow (or equivalently the local viscous energy dissipation rate) in a manner similar to K62. It is unclear why our film behaves differently from previous

studies [41]. One possible reason is the much higher turbulent intensity in the film than in the shallow layer of an electrolyte. The second possibility is the slight compressibility ($\sim 10\%$) of the film.

4.0 SINGLE-POINT VELOCITY STATISTICS

Single-point (SP) velocity statistics are investigated in forced and decaying two-dimensional turbulence in a flowing soap film. It is shown that the probability distribution functions (PDF) in both cases deviate from a Gaussian distribution, which is normally anticipated in turbulent fluid flows. In the forced turbulence case, the tail of the SP velocity PDF decays faster than Gaussian (termed the sub-Gaussian) and can be correlated with the forcing statistics on small scales. In the decaying turbulence case, the SP velocity PDF evolves from a sub-Gaussian to a super-Gaussian behavior as a function of time. However, for all times, the locally averaged vorticity remains normally distributed. While our forced turbulence data may be explained by recent theory proposed by Falkovich et al., the decaying turbulence data remains unexplained.

4.1 INTRODUCTION

It is generally believed that single-point (SP) velocity probability distribution functions (PDF) in turbulent fluid flows are Gaussian, resulting from random accelerations of a fluid element integrated over a time long compared to the correlation time of the acceleration [5, 39]. However, this Gaussian behavior was called into question by a recent theoretical analysis of Falkovich et al. (FKLM) [20, 21], who suggested that the tail part of the PDF, or the so-called rare events, should be correlated with the external force field and therefore in general is not Gaussian. According to this theory, the Gaussian SP velocity PDF only corresponds to a special forcing protocol and thus is not representative of general turbulence behavior. Herein we present experimental evidence obtained in two different experimental settings that show this non-Gaussian characteristic, demonstrating that FKLM's prediction may be observable in laboratory experiments. Both experiments were conducted in flowing soap films with one being constantly forced using an electromagnetic field and the other freely decaying. In the forced 2D turbulence case, the SP velocity PDF is reasonably good Gaussian if the strength of forcing is weak. However, for a strong forcing, the PDF develops sub-Gaussian tails and can be modeled using a modified version of FKLM's theory. In the freely decaying 2D turbulence, the SP velocity statistics show prominent exponential wings and cannot be accounted for by the theory. Though these experiments are by no means exhaustive, they demonstrate that at least in 2D spaces, the SP turbulence statistics is not as simple as previously perceived and calls for a better understanding of the phenomenon.

4.2 EXPERIMENTAL RESULTS

Our experiments were carried out using an electromagnetic convection cell and a vertical soap film channel, both having been described in previous publications [50, 6]. For brevity only information relevant to the current experiment is provided. For the driven turbulence experiment, the film is $7 \times 7 \text{ cm}^2$ and is rendered turbulent by a uniform electric current in the film suspended about $z = 1 \text{ mm}$ above a set of bar magnets. The in-plane electromagnetic

(E&M) force is spatially periodic, unidirectional, and its amplitude can be presented by $f_y = f_0 \sin(\pi x/l_0)$, where the width of the magnet $l_0 \sim 2.5$ mm, x and y represent directions perpendicular and parallel to the magnets. The applied current oscillates in time as a square wave with a frequency of 1 Hz. Depending on the injection current, the root-mean-square (rms) velocity v_{rms} varies between 8 – 14 cm/s, corresponding to a Taylor micro-scale Reynolds number $Re_\lambda = 110 - 212$. The dependence of v_{rms} on Re_λ is approximately linear. Particle imaging velocimetry (PIV) was used to measure the velocity field and about 150 fields (each contained 10^4 vectors) were used to calculate the velocity statistics. For the decaying-turbulence experiment, the soap film is driven by gravity in a channel with a mean speed of $U = 1.25$ m/s. Turbulence was created by inserting a comb (tooth diameter of 1 mm and spacing 2 mm) into the flowing film. The setup is therefore akin to 3D grid turbulence. Once turbulence is created near the comb, there is no feeding mechanism to sustain velocity fluctuations, and consequently these fluctuations decay with time t ($= y/U$ by Taylor frozen turbulence assumption), where y is the downstream distance from the comb. The velocity \vec{v} at different t was measured by a 2-channel Laser Doppler Velocimeter (LDV). Typically 10^6 data points were collected and the SP velocity PDF for each velocity component was calculated separately. An additional LDV channel was also used that enabled measurement of velocity at two separate locations simultaneously. If one uses the Taylor’s frozen turbulence assumption, the measurements using the two probes allow the vorticity $\bar{\omega}$ as a function of t to be determined, where $\bar{\omega}$ is the locally averaged vorticity over the probe separation of 1 mm.

In the decaying turbulence experiment, we used two LDV probes to measure the average vorticity in a circle of radius $r = 2l/3$, where $l = 1$ mm is the horizontal separation between the two probes as shown in Fig. 19. The first probe on the left acquires both x and y components of the velocity, designated as $v_x^{(1)}(t)$ and $v_y^{(1)}(t)$. The second probe on the right acquires only the vertical component of the velocity, designated as $v_y^{(2)}(t)$. The velocity fluctuations are transported downstream by the mean velocity U . The Taylor frozen turbulence assumption allows the average vorticity $\bar{\omega} = \int_S \nabla \times \vec{v} \cdot d\vec{S}/(\pi r^2)$ or the circulation $\bar{\Gamma} = \oint \vec{v} \cdot d\vec{l} = (\pi r^2)\bar{\omega}$ around the circle to be constructed. At a time t , the tangential velocity component $v_T(t)$ at locations “a” and “c” can be constructed from the time series

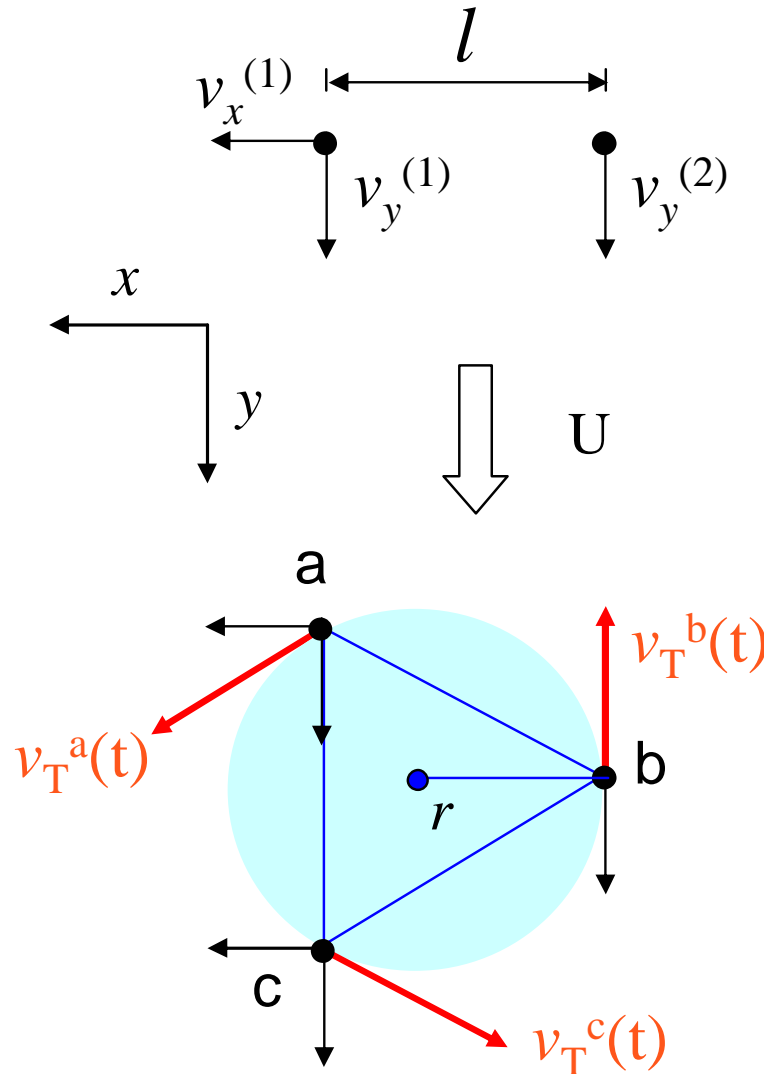


Figure 19: The schematic diagram for calculating the average vorticity using 2-channel LDV. The average vorticity $\bar{\omega}$ can be obtained by adding up the tangential components of the velocity at the points a, b, and c (see the text for details).

of $v_x^{(1)}(t)$ and $v_y^{(1)}(t)$ with the result: $v_T^a(t) = \bar{v}^{(1)}(t - \tau) \cdot \hat{t}_a$ at “a” and $v_T^c(t) = \bar{v}^{(1)}(t + \tau) \cdot \hat{t}_c$ at “c”, where $\tau = l/(\sqrt{3}U)$, and $\hat{t}_a \equiv (\sqrt{3}/2)\hat{x} + (1/2)\hat{y}$ and $\hat{t}_c = -(\sqrt{3}/2)\hat{x} + (1/2)\hat{y}$ are the tangential unit vectors at locations “a” and “c”. Likewise, at the time t , the tangential velocity $v_T(t)$ at position “b” is simply $v_T^b(t) = v_y^{(2)}(t)$. Thus the average vorticity at t is given by $\bar{\omega}(t) \simeq (2/r)(v_T^a(t) + v_T^b(t) + v_T^c(t))$.

Figure 20 shows the PDFs for the velocity component y along the forcing direction for four different injection currents for the forced turbulence experiments. As delineated in the inset, the velocity PDF changes systematically with the current, i.e., the width of $P(v_y)$ broadens continuously as the current increases, indicating that the turbulence intensity (v_{rms}) becomes stronger. The PDFs are nearly symmetric, indicating that all the odd moments are approximately zero. Although the PDFs have similar appearance, the wings of the PDFs become noticeably different if the PDFs are plotted in a non-dimensionalized form $v_{y,rms}P(v_y/v_{y,rms})$ as shown in the main figure. Here we noticed that although the center part of the PDFs can be collapsed and is well described by a Gaussian function (the dashed line), the tails of the PDFs are distinctively different for different runs. Curiously, as the current increases, the PDF decays faster in the tails and they fall well below the Gaussian function for the largest current used in the experiment. To quantify deviations from the Gaussian statistics, we plotted in Fig. 21 the normalized even moments $\Phi(p) \equiv \langle v_y^p \rangle / \langle v_y^2 \rangle^{p/2}$ for $p = 2, 4, 6, 8$, and 10. To ensure that the high-order moments can be reliably calculated using the measured PDFs we also displayed in the inset the integrand $v_y^{10}P(v_y)$ for the four runs. The inset shows that even for the highest moment, the integrands are still reasonably well behaved for large v_y and can yield estimates for $\Phi(p)$ up to $p = 10$. The solid squares in the main figure are the calculated values based on the Gaussian distribution, and the diamonds, stars, triangles, and circles are for the runs with $Re_\lambda = 110, 137, 180$ and 212, respectively. It is evident that as far as the low moments are concerned, such as the flatness $F \equiv \Phi(4)$, the experimental data are indistinguishable from the values derived from the normal distribution with $F = 3$. As noted earlier, the skewness $S \equiv \Phi(3)$ is approximately zero for all runs. However, for large moments ($p > 6$), which are more sensitive to the tails of the PDFs, the difference between the measurement and the Gaussian prediction becomes noticeable and this difference increases with Re_λ . The above findings are consistent with

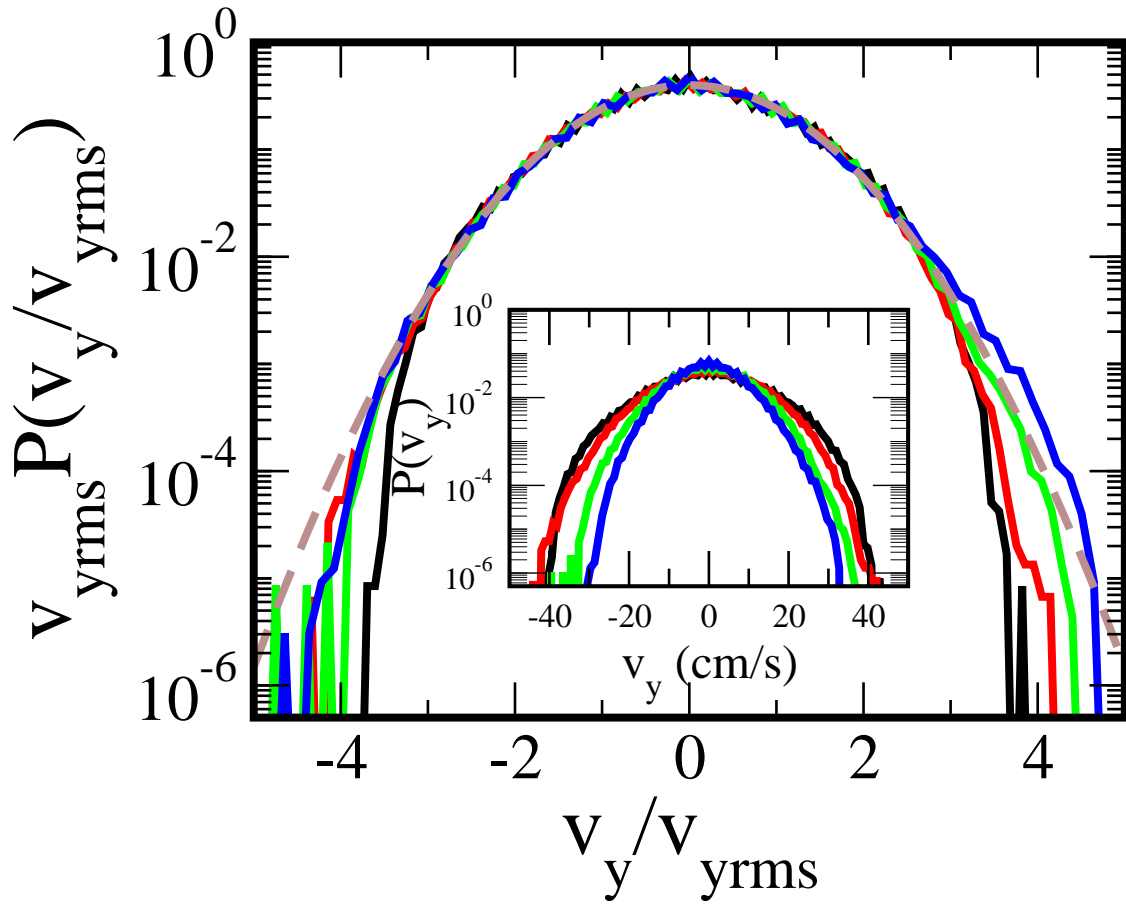


Figure 20: The SP velocity PDF along the forcing direction when $v_{yrms}=8.4$ (blue), 9.9 (green), 12.1 (red), and 13.2 (black) cm/s, corresponding to $Re_\lambda = 110, 137, 180,$ and 212, respectively. The curves in the main figure are normalized whereas those in the inset are unnormalized. The tails of the PDFs deviate from Gaussian, which is delineated by the dashed line.

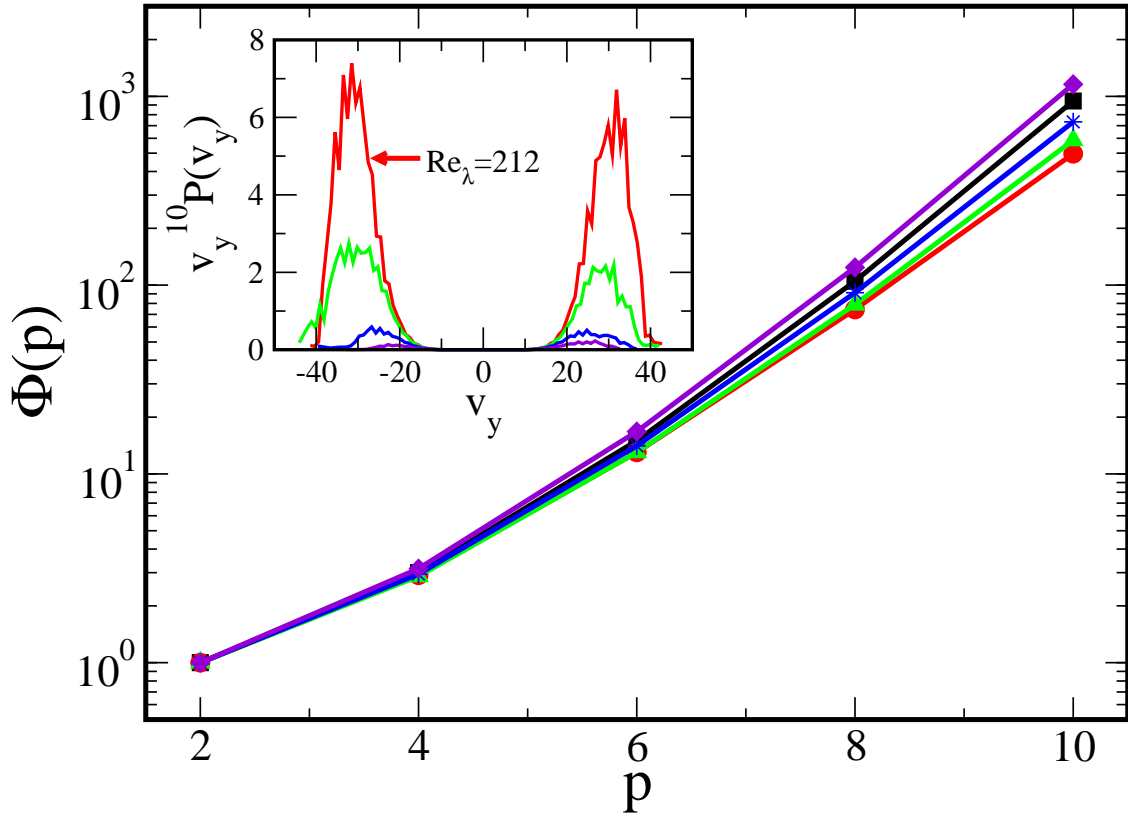


Figure 21: The normalized even moments $\Phi(p)$ vs. p . The symbols correspond to $\text{Re}_\lambda = 110$ (diamonds), 137 (stars), 180 (triangles), and 212 (circles). $\Phi(p)$ for the normal distribution is plotted as squares. The inset shows the integrand $v_y^{10}P(v_y)$ for $\text{Re}_\lambda=110, 137, 180,$ and 212.

investigations by pioneers in the field [5, 39] who used the measured S and F to justify that the SP velocity PDF of 3D turbulence is normally distributed. Their view on this matter has been widely accepted until recently [21]. We also investigated SP velocity PDF of the transverse velocity component v_x . Because of unidirectional forcing in this experiment, this velocity component is not directly coupled to f_y but receives energy due to the pressure term in the Navier-Stokes equation. Interestingly $P(v_x)$ in all four cases is much closer to Gaussian than $P(v_y)$ and thus displays a universal behavior.

An analysis of 2D decaying turbulence notes that although turbulence is not homogeneous in this case, the local fluctuations are nearly isotropic. Thus, in the following, only measurements of the horizontal velocity component v_x are presented. Our experiment shows that SP velocity PDFs for decaying turbulence are significantly different from the forced ones. We noticed that the functional form of the PDF changes continuously with the downstream distance y or time t as depicted in Fig. 22(a). For short times, the $P(v_x)$ is sub-Gaussian with a characteristic flat top. For long times, however, the PDFs sharpen and develop exponential wings for large v_x . Most interestingly this exponential function appears to be the asymptotic form as illustrated in the inset, where it is shown that $P(v_x)$ becomes nearly independent of t in late times. The observed velocity PDFs are very different from the vorticity PDFs, which are presented in Fig. 22(b). Although $P(\bar{\omega})$ also becomes narrower in late times, its functional form remains approximately Gaussian independent of t .

To analyze the time dependence of decaying turbulence, in Fig. 23(a) the flatness F of the velocity distribution, and in Fig. 23(b) the normalized energy E/E_0 and the normalized enstrophy Ω/Ω_0 are plotted as a function of t , where $E = \langle v^2 \rangle / 2$, $\Omega = \langle \bar{\omega}^2 \rangle / 2$, and E_0 and Ω_0 are the initial energy and enstrophy, respectively. One observes that $F \sim 2.2$ in early times and gradually approaches the Gaussian value of 3 at $t \simeq 0.1$ s, which corresponds to about 30 initial eddy turnover time $\tau_i \equiv 1/f_0$, with f_0 being the vortex shedding frequency. Remarkably, for $t > 0.1$ s, the flatness increases markedly and reaches $F \simeq 6$, which is consistent with the PDF being exponential. The normalized total energy E/E_0 and enstrophy Ω/Ω_0 of the system also evolve with t ; they both decay slowly initially and then rapidly in long times. Inspection of Figure 23 reveals that when the flatness starts to increase sharply,

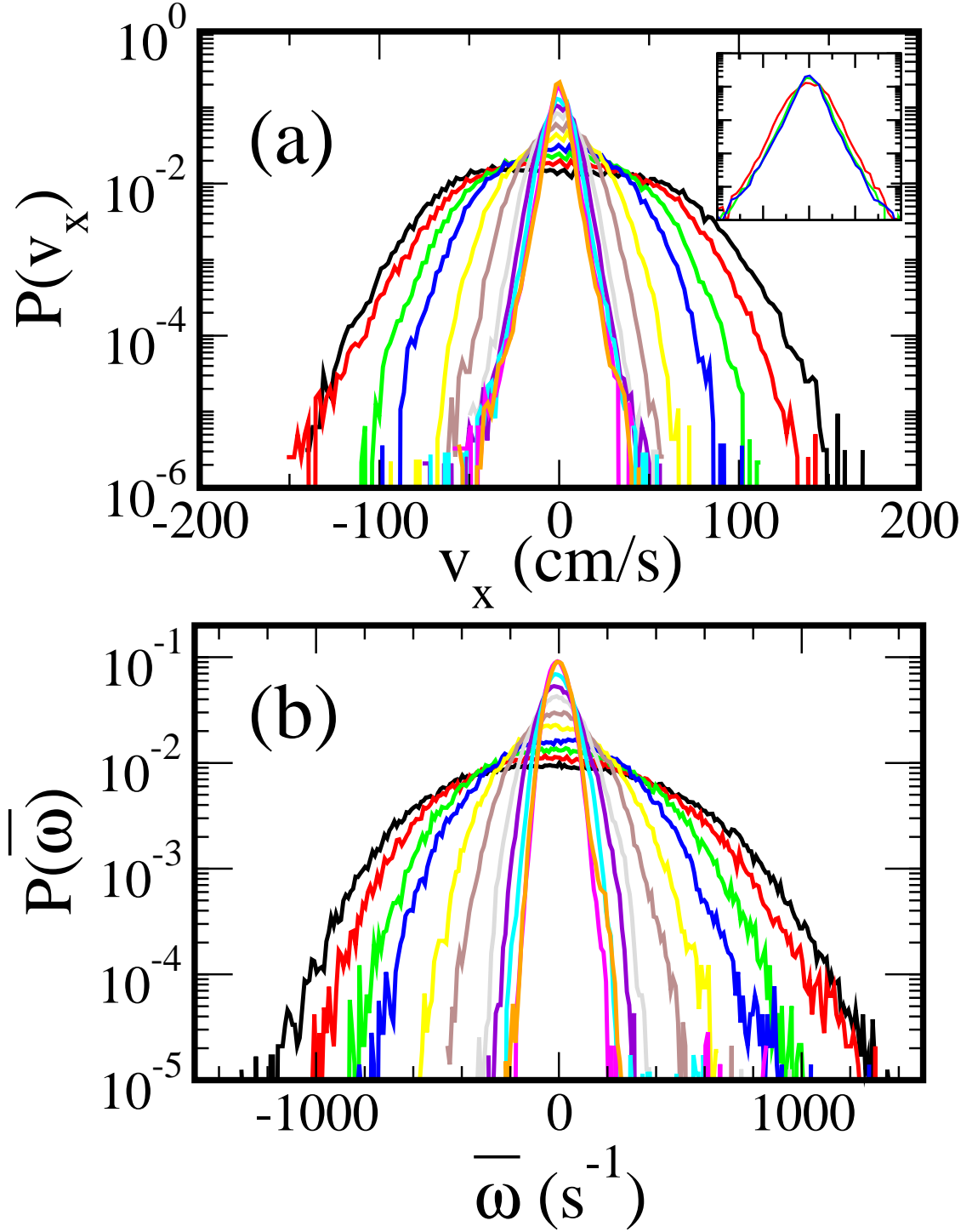


Figure 22: The SP velocity v_x (a) and vorticity $\bar{\omega}$ (b) PDFs at different times t in decaying 2D turbulence. As t increases (0.01, 0.02, 0.03, 0.05, 0.08, 0.11, 1.15, 0.18, 0.21, 0.26, and 0.33 s), the $P(v_x)$ becomes narrower, and evolves from sub-Gaussian ($F < 3$) to super-Gaussian ($F > 3$). The $P(\bar{\omega})$ however remains approximately Gaussian. The inset displays the late-time velocity PDFs with $t=0.21, 0.26,$ and 0.33 s.

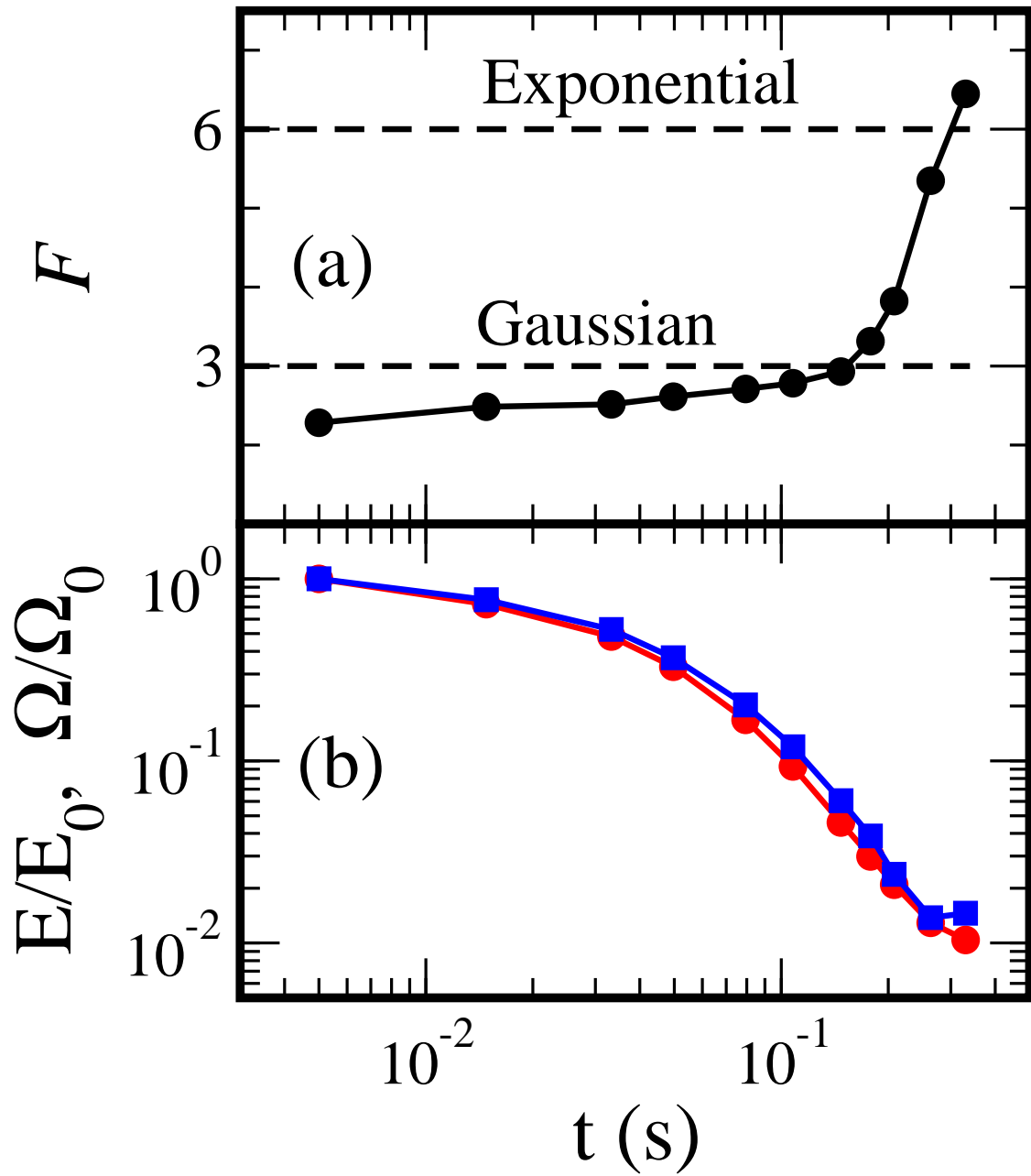


Figure 23: (a) The flatness F (a), and (b) the normalized energy E/E_0 (squares) and the normalized enstrophy Ω/Ω_0 (circles) vs. t .

most energy and enstrophy have already been drawn out of the system, and turbulence is in its late stage of evolution. Indeed a measurement of the integral scale shows that l is about 4.5 cm, which is about half of the channel width. Thus, it may be concluded that the exponential SP velocity PDF is associated with the late stage of 2D decaying turbulence.

The theory of FKLM provides a general method for finding the tails of the probability distribution functions, which are the solutions of stochastically forced differential equations. The remarkable finding of the theory is that these rare events are not completely random but are corresponding to “extreme” field-force configurations, which were coined as “instantons” by the investigators [20]. A similar approach was also used in treating properties of metals with quenched disorders [35]. Although a field theoretical approach was used in FKLM’s derivation, the physical idea may be conveyed using simple pictures. It is shown using saddle-point integrals that the tail of the SP velocity PDF is ascribed to the large-scale velocity fluctuations that have a turnover time $t_L = L/v$, where L is the integral scale of turbulence. For t_L shorter than the typical forcing time τ , the velocity is pumped by the external force f (or acceleration) $v \sim ft$ until it is saturated at $t = t_L$. This yields $v^2 \sim fL$ and the velocity distribution function $P_v(v)$ is related to the forcing statistics $P_f(f)$ by $P_v(v) \propto P_f(v^2/L)$. In the opposite limit, when t_L is much greater than τ , $v^2 \sim f^2 t_L \tau$ or $v^3 \sim f^2 L \tau$. This yields $P_v(v) \propto P_f(v^{3/2}/(L\tau)^{1/2})$. Hypothetically, if the forcing is a Gaussian process, FKLM predicts $P_v(v) \propto \exp(-v^4)$ for $t_L \ll \tau$ and $P_v(v) \propto \exp(-v^3)$ for $t_L \gg \tau$. In either case, the SP velocity PDF falls off faster than the force PDF. According to this theory, the Gaussian velocity PDF corresponds to a special forcing protocol with $P_f(f)$ obeying an exponential distribution and the force-force correlation time τ is very short. One of the interesting predictions of FKLM is that as one gets further into the tail of the PDF, the statistics should become more in favor of the long forcing-time limit ($t_L \ll \tau$). This is because for the given integral scale L , a large velocity v implies a small $t_L (= L/v)$ and consequently the short-forcing-time limit ($\tau \ll t_L$) becomes increasingly more difficult to satisfy when v increases. As noted latter, this prediction appears to be consistent with the author’s observations.

In order to make comparisons between theory and observation such as those in Fig. 20, a conceptual difficulty arises; namely, the force field in our experiment is not random but is periodic in time. This difficulty however can be circumvented by recognizing that it is the energy injection rate $\varepsilon = \vec{f} \cdot \vec{v}$ that is responsible for driving turbulent fluid flows, $v^2 (\equiv \vec{f} \cdot \vec{v} t) = \varepsilon t$. Unlike \vec{f} , ε is stochastic with a defined distribution $P_\varepsilon(\varepsilon)$ and a correlation time. This enables us to generalize FKLM to situation where the forcing itself is not random. Using the E&M cell, the velocity fields were acquired simultaneously with the current injection. The $P_\varepsilon(\varepsilon)$ was thus measured by knowing the phase of $\vec{f}(\vec{x}, t)$ and the velocity $\vec{v}(\vec{x}, t)$. Following FKLM's argument, one could derive the relationships between ε and v . In the long-forcing-time limit ($t_L \ll \tau$), $v^3 \propto \varepsilon L$, and $P_v(v) \sim P_\varepsilon(\varepsilon^{1/3})$. On the other hand, in the short-forcing-time limit ($t_L \gg \tau$), $v^5 \propto \varepsilon^2 L \tau$, and $P_v(v) \sim P_\varepsilon(\varepsilon^{2/5})$. In our experiment, since $L \simeq 2.5$ cm and $v_{rms} \simeq 13$ cm/s, the energy transfer time is $t_L \simeq 0.2$ s. Although the forcing is oscillatory with a period of 1 second, the correlation time for the energy injection is much shorter and can be estimated as $\tau = l_0 / \delta v_{l_0}$. Taking $l_0 = 0.25$ cm (the magnet size) and the velocity difference on the scale l_0 to be $\delta v_{l_0} \simeq 6$ cm/s, we found the energy injection correlation time $\tau \simeq 0.04$ s, which is shorter than t_L . This analysis suggests that our experiment is in the short-forcing-time regime, and $P_v(v) \sim P_\varepsilon(\varepsilon^{2/5})$ is to be expected.

The measured $P_\varepsilon(\varepsilon)$ is slightly asymmetric and is skewed towards the positive value of ε as it should be. To compare with the velocity distribution $P(v_y)$, the symmetric part of $P_\varepsilon(\varepsilon)$ was constructed, $P_\varepsilon^S(\varepsilon) \equiv (P_\varepsilon(-\varepsilon) + P_\varepsilon(\varepsilon))/2$, and used for the calculation. In Fig. 24, $P(v_y) \sim P_\varepsilon^S(\varepsilon^{2/5})$ (thick solid line) and $P_\varepsilon^S(\varepsilon^{1/3})$ (thin solid line) are plotted along with the run (circles) having the strongest external forcing, $Re_\lambda = 212$. For comparisons, the Gaussian PDF (dashed line) is also plotted. It is evident that for this normal distribution, large deviations were observed for $v_y > 2v_{y,rms}$. The expected theoretical form $P(v_y) \sim P_\varepsilon(\varepsilon^{2/5})$ works significantly better than the Gaussian, and the fit to the long-forcing-time prediction $P(v_y) \sim P_\varepsilon(\varepsilon^{1/3})$ is also reasonable. For completeness, we also analyzed the measurements using the generalized form $P(v_y) \sim P_\varepsilon(\varepsilon^\alpha)$, where α is a free parameter. A simple fitting procedure to the data in Fig. 20 yields $\alpha \sim 0.67, 0.64, 0.58$, and 0.4 for $Re_\lambda = 110, 137, 180$, and 212 , respectively. This result is plotted in the inset of Fig. 24, showing that α is a decreasing

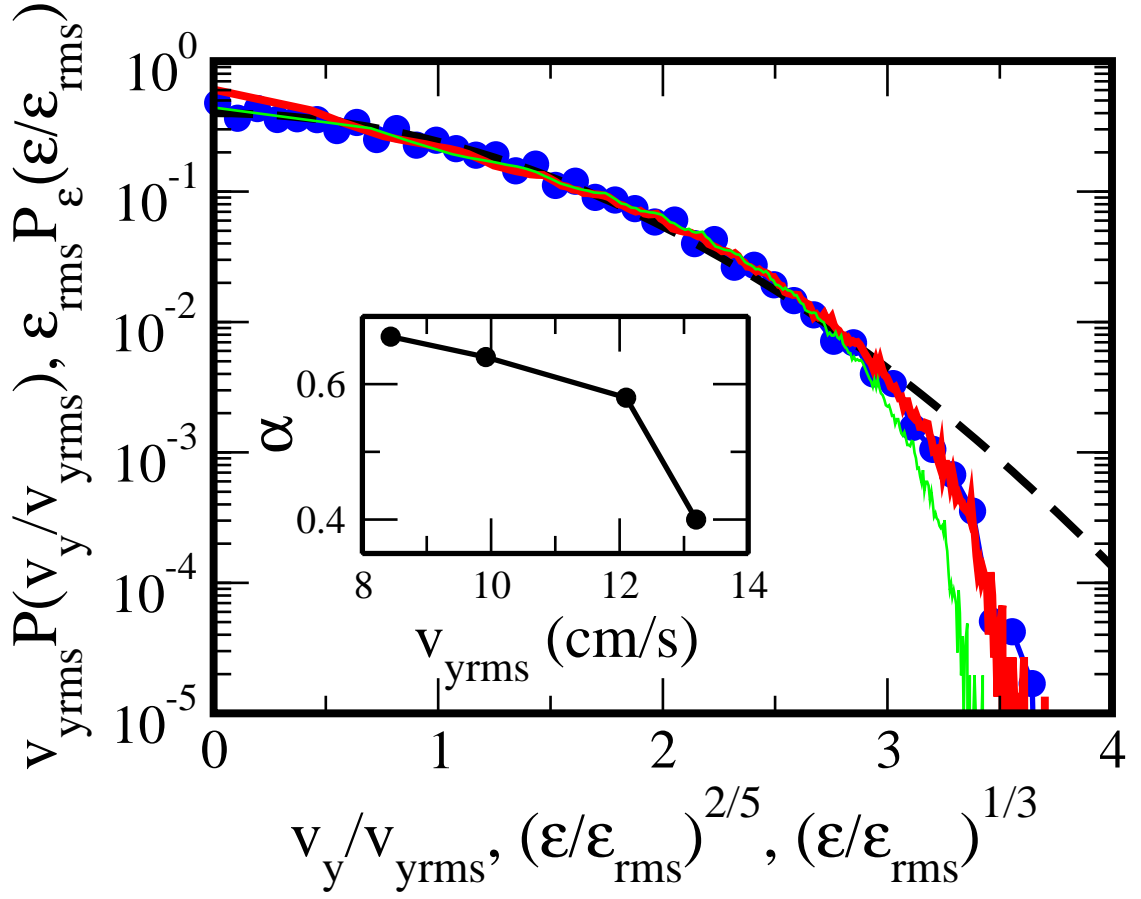


Figure 24: The normalized SP velocity PDF (circles) and the PDFs calculated based on the energy injection rate ϵ with $\alpha = 2/5$ (thick red line) and $1/3$ (thin green line) at $Re_\lambda = 212$ (see text for more details). The Gaussian PDF is presented by the dashed line. Inset: Exponent α is plotted as a function of v_{yrms} .

function of v_{yrms} or Re_λ . This trend is consistent with the theory in that as v_{yrms} increases, the system is more appropriately described by the long-forcing-time behavior with a decreasing α . Asymptotically one expects $\alpha = 1/3$ but it is not attained in the current measurement.

4.3 CONCLUSION

To conclude, we have investigated systematically the effect of external forcing on the single-point velocity statistics of 2D driven and 2D decaying turbulence. Remarkable differences are found in the two cases. For a weak external forcing, the PDF is approximately a Gaussian function. However, as the strength of the external force increases, the tail part of the PDFs increasingly deviate from Gaussian. The faster than Gaussian decay in the wings of the SP velocity PDF is consistent with the theoretical prediction of FKLM. The most unexpected aspect of this experiment is the exponential tail for the decaying 2D turbulence. Our measurement shows that such a tail appears prominently at the late stage of turbulence evolution. Physically, this corresponds to a small number of energetic vortices and their spatial distribution determines the shape of the PDF. There have been many discussions about the final state of a vortex liquid, which in the limit of vanishing viscosity or a large Re_λ , is expected to be governed by the maximization of entropy of the vorticity distribution [13]. The possible connection between our measured SP velocity PDFs and theory concerning the time evolution towards this final state in an open system remains to be explored.

APPENDIX A

HIERARCHICAL STRUCTURE MODEL

The lognormal model [32] proposed by Kolmogorov explains our data reasonably well. However, the lognormal model has the defect that as $p \rightarrow \infty$, $d\zeta_p/dp < 0$ which is not physical as recognized by Novikov [40]. To overcome such a short coming, a new model was proposed by She and Leveque (SL) [52] based on the hierarchical structures in fully developed turbulence. The SL model shows very good agreement with experimental and numerical results. Later, Dubrulle [19], and She and Waymire [52] interpreted the SL model based on log-Poisson statistics. We analyzed our data based on hierarchical structure model and the results clearly show that 2D turbulence at large scales is intermittent.

In fully developed 3D turbulence, the non-uniform distribution of the coarse-grained energy dissipation rate ε_l^{dis} is responsible for intermittency, and scales as $\delta v_l^3 \sim \varepsilon_l l$. This is called the Kolmogorov refined self-similarity hypothesis (KRSH). The moments of δv_l have the scaling behavior,

$$\langle (\delta v_l)^p \rangle \sim \langle \varepsilon_l^{p/3} l^{p/3} \rangle \sim l^{\tau_p/3} l^{p/3} \sim l^{\zeta_p}, \quad (\text{A.1})$$

where τ_q is the scaling exponent of the moments of ε_l : $\langle (\varepsilon_l)^q \rangle \sim l^{\tau_q}$. Here, one can obtain the relation $\zeta_p = p/3 + \tau_p/3$. SL further assumed a hierarchical relation between the ratio of the adjacent moments of the energy dissipation rates on scale of l as

$$\varepsilon_l^{(p+1)} = A_p \varepsilon_l^{(p)\beta} \varepsilon_l^{(\infty)1-\beta}, \quad 0 < \beta < 1, \quad (\text{A.2})$$

where

$$\varepsilon_l^{(p)} = \langle \varepsilon_l^{p+1} \rangle / \langle \varepsilon_l^p \rangle \quad \text{and} \quad \varepsilon_l^{(\infty)} = \lim_{p \rightarrow \infty} \varepsilon_l^{(p)} \quad (\text{A.3})$$

By definition, $\varepsilon_l^{(0)}$ is scale independent simply because $\varepsilon_l^0 = \langle \varepsilon_l^1 \rangle / \langle \varepsilon_l^0 \rangle = \langle \varepsilon \rangle$. Assuming that the most singular structures of turbulence are filaments, the quantity $\varepsilon_l^{(\infty)}$ associated with such structures was derived by SL:

$$\varepsilon_l^{(\infty)} \sim l^{-2/3}. \quad (\text{A.4})$$

From Eq. (A.2), (A.3), and (A.4), one can obtain an iteration relation:

$$\tau_{p+2} - (1 + \beta)\tau_{p+1} + \beta\tau_p + \frac{2(1 - \beta)}{3} = 0. \quad (\text{A.5})$$

SL solved the equation with the result:

$$\beta = 2/3 \quad \text{and} \quad \tau_p = -\frac{2}{3}p + 2(1 - 2/3)^p. \quad (\text{A.6})$$

This finally gives

$$\zeta_p = p/9 + 2 \left[1 - \left(\frac{2}{3} \right)^{p/3} \right]. \quad (\text{A.7})$$

For $p=3$, $\zeta_{p=3}=1$ as expected by K41, and for $p \rightarrow \infty$, $\zeta_p = p/9 + 2$, which $d\zeta_p/dp = 1/9 > 0$ so that it doesn't have the defect of the log-normal model, which has a negative slope at large p .

Although the SL model gives good agreement with data which have the Kolmogorov-like scaling exponents, we cannot apply the SL model to our data because the initial slope of ζ_p of our data is greater than $1/3$ predicted by K41. So, Dubrulle suggested that if the generalized scale $\xi(l) = \langle \langle \varepsilon_l \rangle^{-1} \delta v_l^3 \rangle$ is introduced, the SL model satisfies the extended self-similarity [19]. Using a different assumption of $\varepsilon_l^{(\infty)} \sim l^{-\Delta}$ with $0 \leq \Delta \leq 1$, and the definition $\pi_l = \varepsilon_l / \varepsilon_l^{(\infty)}$, we can write:

$$\frac{\delta v_l^3}{\langle \delta v_l^3 \rangle} \doteq \frac{\varepsilon_l}{\langle \varepsilon_l \rangle} = \frac{\pi_l}{\langle \pi_l \rangle}, \quad (\text{A.8})$$

where the symbol \doteq means that both sides have the same scaling properties, i.e. that the moments of both sides are proportional. Moreover, Eq. (A.2) is given by

$$\frac{\langle \pi_l^{p+1} \rangle}{\langle \pi_l^p \rangle} = A_p \left(\frac{\langle \pi_l^p \rangle}{\langle \pi_l^{p-1} \rangle} \right)^\beta, \quad (\text{A.9})$$

and

$$\langle \pi_l \rangle \sim \left(\frac{\langle \delta v_l^3 \rangle}{l_{dis} \langle \varepsilon \rangle} \right)^\Delta, \quad (\text{A.10})$$

where l_{dis} is the dissipative length scale and $\langle \varepsilon \rangle$ is the average energy dissipation rate of the system. Eq. (A.10) states that the dissipative structures are spatially intermittent. Then, one can get the relation

$$\langle \delta v_l^p \rangle \sim \langle \delta v_l^3 \rangle^{\zeta_p/\zeta_3},$$

with

$$\frac{\zeta_p}{\zeta_3} = (1 - \Delta) \frac{p}{3} + \frac{\Delta}{1 - \beta} (1 - \beta^{p/3}). \quad (\text{A.11})$$

If $\zeta_3 = 1$ and $\Delta = \beta = 2/3$, Eq. (A.7) can be recovered.

When expressed in terms of the velocity structure function, Eq. (A.2) and (A.9) can be written as

$$\frac{S_{p+1}(l)}{S_p(l)} = A_p \left[\frac{S_p(l)}{S_{p-1}(l)} \right]^\beta [S^{(\infty)}(l)]^{1-\beta}, \quad (\text{A.12})$$

where $S^{(\infty)}(l) \equiv \lim_{p \rightarrow \infty} S_{p+1}(l)/S_p(l)$ for $0 < \beta < 1$, and A_p is a constant independent of l . Since it is difficult to obtain $S^{(\infty)}(l)$ for infinite p , $S^{(\infty)}(l)$ can be removed by normalizing Eq. (A.12) with Eq. (A.12) of $p = 1$:

$$\frac{H_{p+1}(l)}{H_2(l)} = \frac{A_p}{A_1} \left[\frac{H_p(l)}{H_1(l)} \right]^\beta \quad (\text{A.13})$$

where $H_p(l) = S_p(l)/S_{p-1}(l)$.

Fig. 25 shows the log-log plot of Eq. (A.13). The scaling exponent β in fully developed turbulence is a measure of intermittency [19]. For instance, when $\beta = 1$, turbulence is nonintermittent. We found in our experiment $\beta \simeq 0.82 \pm 0.01$ (circles) and 0.84 ± 0.01 (squares) at $\text{Re}_\lambda = 212$ and 110 , respectively. These are different from unity for nonintermittent flow (solid line) and $2/3$ (dashed line) for 3D turbulence. This indicates that intermittency in 2D turbulence exists even though it is small compared to that in 3D turbulence. From this analysis, we also found β is not strongly dependent on the turbulence intensity.

Considered next is the quantity Δ , which is linked to the codimension $C_0 = d - D$ of the dissipative structures, where d and D are the real dimension of the system and the embedded dimension in the system. [19]. One can rewrite Eq. (A.11) as

$$\frac{\zeta_p}{\zeta_3} - \Gamma = (1 - \Delta) \left[\frac{p}{3} - \Gamma \right] \quad (\text{A.14})$$

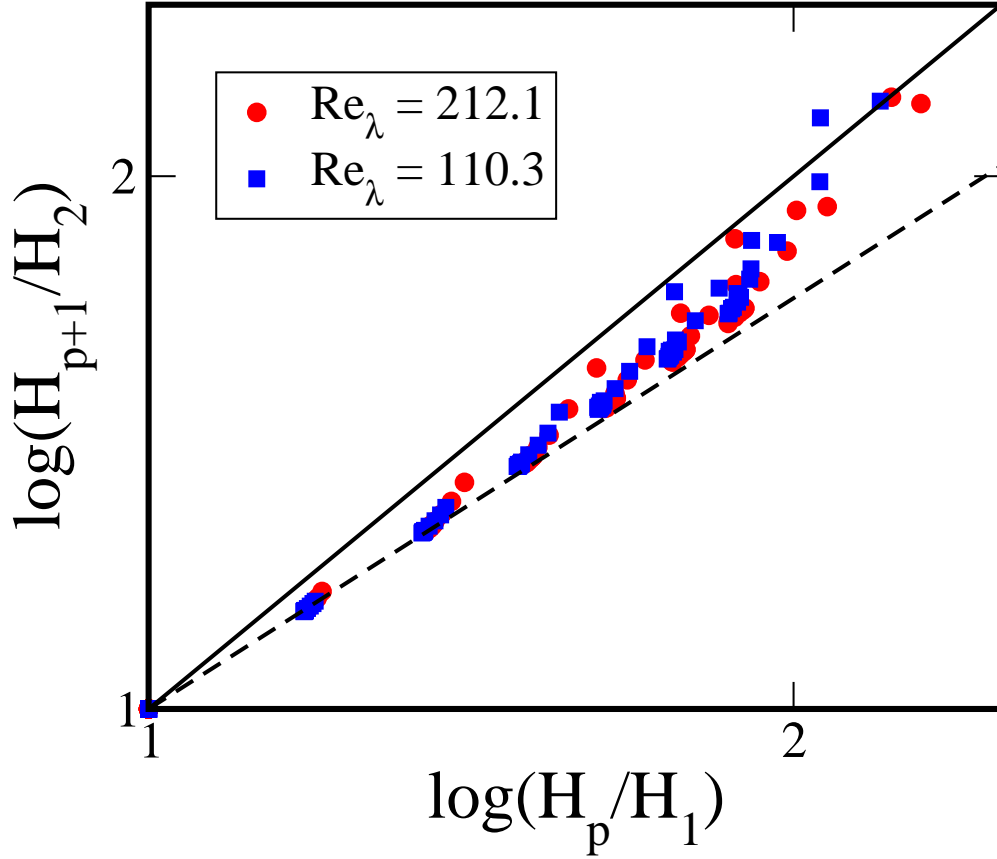


Figure 25: The log-log plot for the test of the hierarchical structures: $\frac{H_{p+1}(l)}{H_2(l)} = \frac{A_p}{A_1} \left[\frac{H_p(l)}{H_1(l)} \right]^\beta$. It is represented as the circles and the squares at $\text{Re}_\lambda = 212$ and 110, respectively. The solid line and the dashed line denote the slope $\beta = 1$ and $2/3$, respectively.

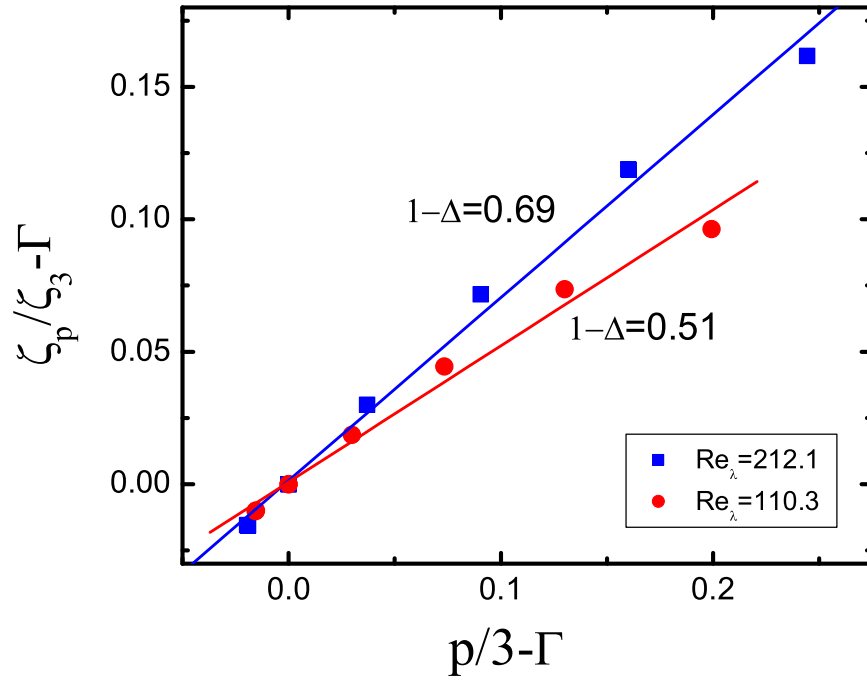


Figure 26: The plots of Eq (A.14). Δ is obtained from the slopes of the plots: 0.31 for $\text{Re}_\lambda = 212$ and 0.49 for $\text{Re}_\lambda = 110$.

where $\Gamma = (1 - \beta^{p/3})/(1 - \beta)$. Fig. 26 is the plot of Eq. (A.14) for $\text{Re}_\lambda = 212.1$ (squares) and 110 (circles). The Δ s obtained from the slopes of the plot are 0.31 ± 0.02 for $\text{Re}_\lambda = 212$ and 0.49 ± 0.02 for $\text{Re}_\lambda = 110$. These values are smaller than that in the SL model, which is $2/3$ in 3D turbulence.

Fig. 27 is the plot of ζ_p/ζ_3 based on β and Δ obtained from experimental data. It shows a good agreement with the experimental data up to $p = 8$.

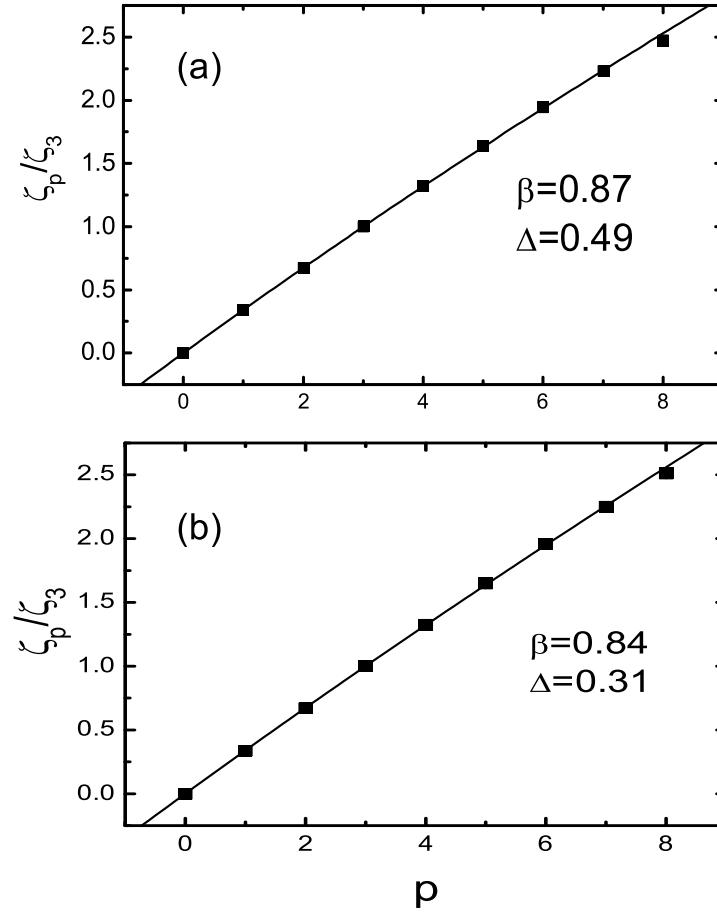


Figure 27: The plot of ζ_p / ζ_3 based on the log-Poisson fit for $\text{Re}_\lambda = 212$ (a) and 110 (b).

APPENDIX B

LOCAL AVERAGE STATISTICS

Until now we have focused on whether 2D turbulence is intermittent and if it is, how to describe it. A different view is that while intermittency is absent in 2D turbulence, it is believed to result from the nonuniform distribution of the energy dissipation rate in fully developed 3D turbulence. We present the connection between the energy transfer rate Π_l and the squared strain rate σ_l^2 in forced 2D turbulence. When the energy transfer rate is conditioned by the strain rate, intermittency is surprisingly reduced.

The coarse-grained two-point velocity difference with a separation l is given by

$$\{\delta v_l^3(\vec{x})\} \equiv \frac{1}{N} \sum_i^N \left[[(\vec{v}(\vec{x}') - \vec{v}(\vec{x}))]^2 (\vec{v}(\vec{x}') - \vec{v}(\vec{x})) \cdot \hat{l} \right]_i$$

or

$$\{\delta v_l^3(\vec{x})\} \equiv \frac{1}{N} \sum_i^N \left[[\delta v_{l/2}(\vec{x})]^2 \cdot \delta v_{l/2}^L \right]_i,$$

where the bracket $\{\dots\}$ denotes the circular average around a circle with a radius $l/2$, N is the number of velocity difference pairs of length $l/2$ centered at the location \vec{x} , and \hat{l} is the unit vector in the direction between two points. The velocity difference is defined by $\delta v_{l/2} \equiv \vec{v}(\vec{x}') - \vec{v}(\vec{x})$ and $\delta v_l^2 \equiv [(\vec{v}(\vec{x}') - \vec{v}(\vec{x}))]^2 = (\delta v_l^L)^2 + (\delta v_l^T)^2$, where the superscript L and T denote the longitudinal and transverse components of the velocity difference, respectively. For isotropic turbulence, this quantity $\{\delta v_l^3(\vec{x})\}$ corresponds to the two point velocity difference $\delta v_l^3 = [(\vec{x}_l(\vec{x} + \vec{l}) - \vec{v}(x)) \cdot \hat{l}]^3$ usually adapted in 2D and 3D turbulence analysis.

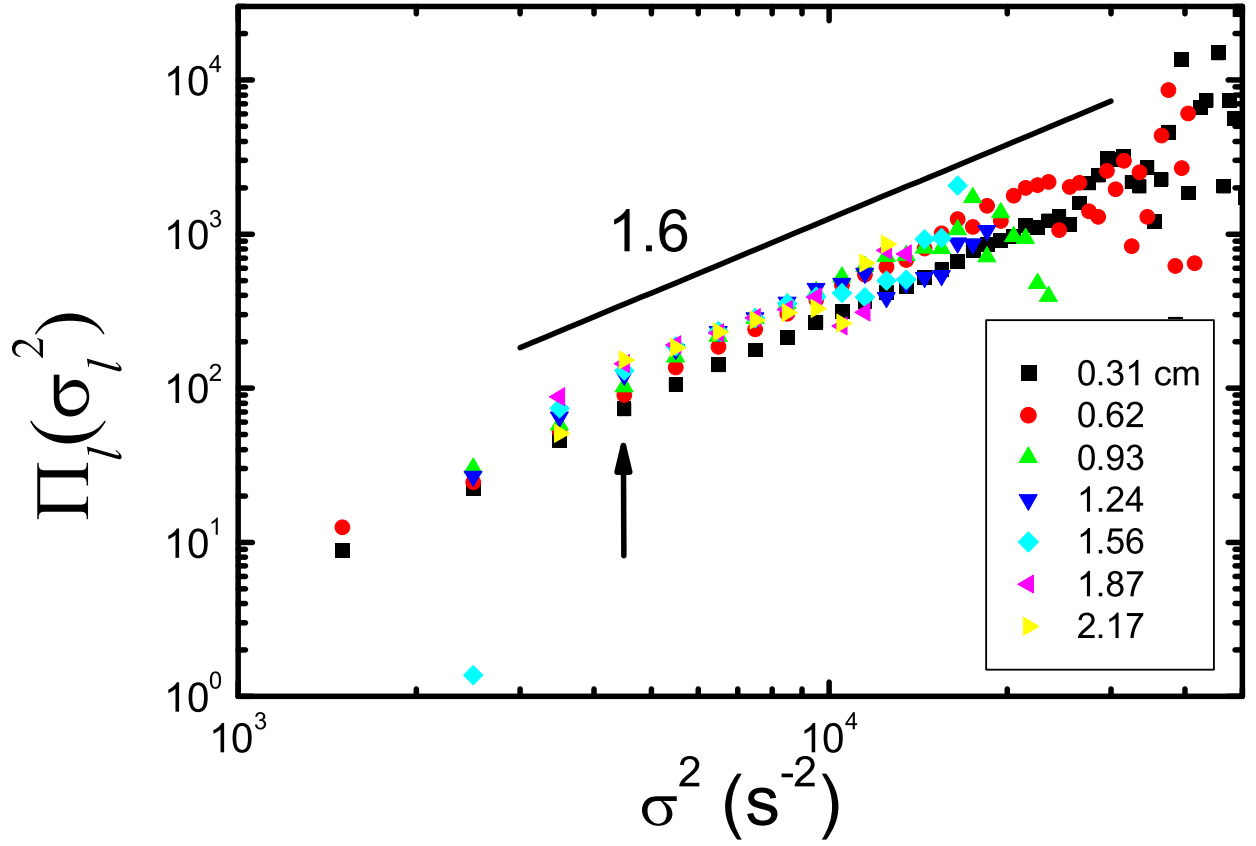


Figure 28: The coarse-grained energy transfer rate Π_l as a function of the coarse-grained strain rate σ_l^2 . The length scales are 0.31 (squares), 0.62 (circles), 0.93 (triangle), 1.24 (triangle-down), 1.56 (diamond), 1.87 (triangle-left), and 2.17 (triangle-right) cm. The arrow denotes $\sigma_l^2 = 4500 \text{ s}^{-2}$.

The corresponding energy transfer rate ϕ_l is

$$\phi_l(\vec{x}) \equiv \frac{1}{l} \{ \delta v_l^3(\vec{x}) \},$$

which indicates the energy flow per second through the circle of a diameter l centered at \vec{x} . The coarse-grained strain rate in the circle of the radius $l/2$ centered at \vec{x} is defined as follows:

$$\sigma_l^2(\vec{x}) = \frac{1}{M} \sum_i^M \sigma_i^2(\vec{x}') \text{ with } |\vec{x} - \vec{x}'| < l/2$$

where M is the number of the points of $\sigma^2(\vec{x}')$ inside the circle. It is interesting to investigate the correlation between the the energy flux and the strain rate on the given circles.

In Fig. 28, the quantity Π_l is plotted as a function of σ_l^2 , which is obtained by the definition,

$$\Pi_l(\sigma_l^2) = \langle |\phi_l(\sigma_l^2)| \rangle \equiv \int_{-\infty}^{+\infty} |\phi_l| P(\phi_l | \sigma_l^2) d\phi_l$$

where $P(\phi_l | \sigma_l^2)$ is the conditional probability distribution function of ϕ_l . The $\Pi_l(\sigma_l^2)$ s at different scales l overlap in the range of $2500 \text{ s}^{-2} < \sigma_l^2 < 11500 \text{ s}^{-2}$. Outside the above quoted range of σ_l^2 , the deviations come from the lack of statistics. The length scales in the plot are 0.31 (squares), 0.62 (circles), 0.93 (triangle), 1.24 (triangle-down), 1.56 (diamond), 1.87 (triangle-left), and 2.17 (triangle-right) cm. In the overlapping σ_l^2 range, we found the relation $\Pi_l \sim (\sigma_l^2)^{1.6}$, which is different from Kolmogorov's prediction for 3D turbulence, $\Pi_l \sim \sigma_l^2$, indicating the energy flux is not entirely determined by σ_l^2 . This relation is universal and independent of the Reynolds number Re_λ and the length scales l in our experiment.

It is interesting to ask what is responsible for the inverse energy cascade in large scales. To answer this question we investigated the energy transfer rate to small scales and to large scales. The outward flux, Π_l^+ (circle), and the inward flux, Π_l^- (square), are plotted in Fig. 29. For comparison, we display the absolute values of Π_l^- . The scaling behaviors are very similar in both cases in all length scales, while the number of events (frequency) of Π_l^+ is larger than that of Π_l^- for a given $\sigma_l^2(\vec{x}) \sim 4500 \text{ s}^{-2}$, as shown in Fig. 30. This suggests that for all length scales the energy flux always fluctuates, but the inverse energy cascade in the large scales is due to the asymmetric distribution of Π_l^+ and Π_l^- , which means that the frequency of Π_l^+ is greater than that of Π_l^- at given σ_l .

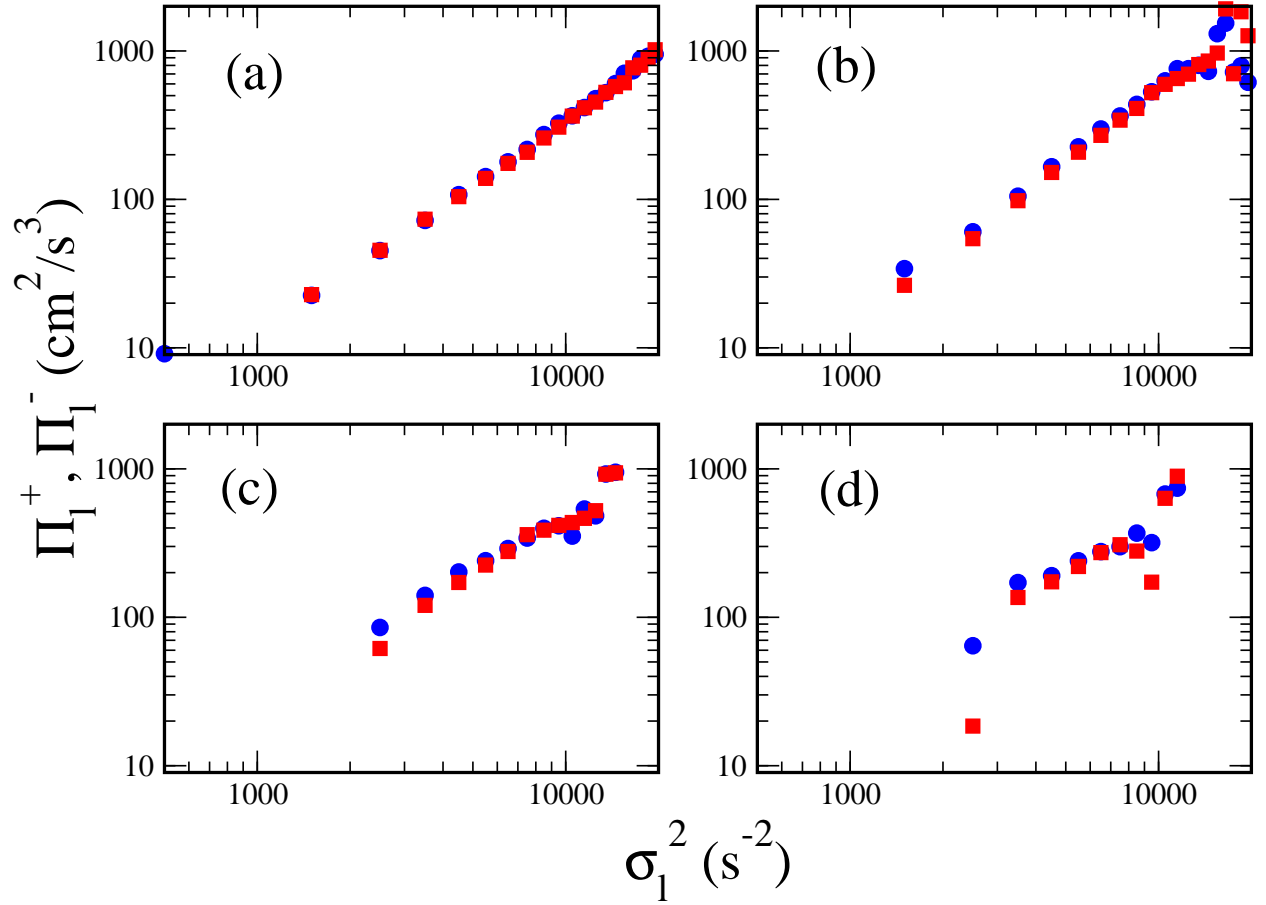


Figure 29: The coarse-grained outward energy flux Π_l^+ (circles) and inward flux Π_l^- (squares). The length scales l are 0.31 (a), 0.93 (b), 1.56 (c), and 2.17 (d) cm.

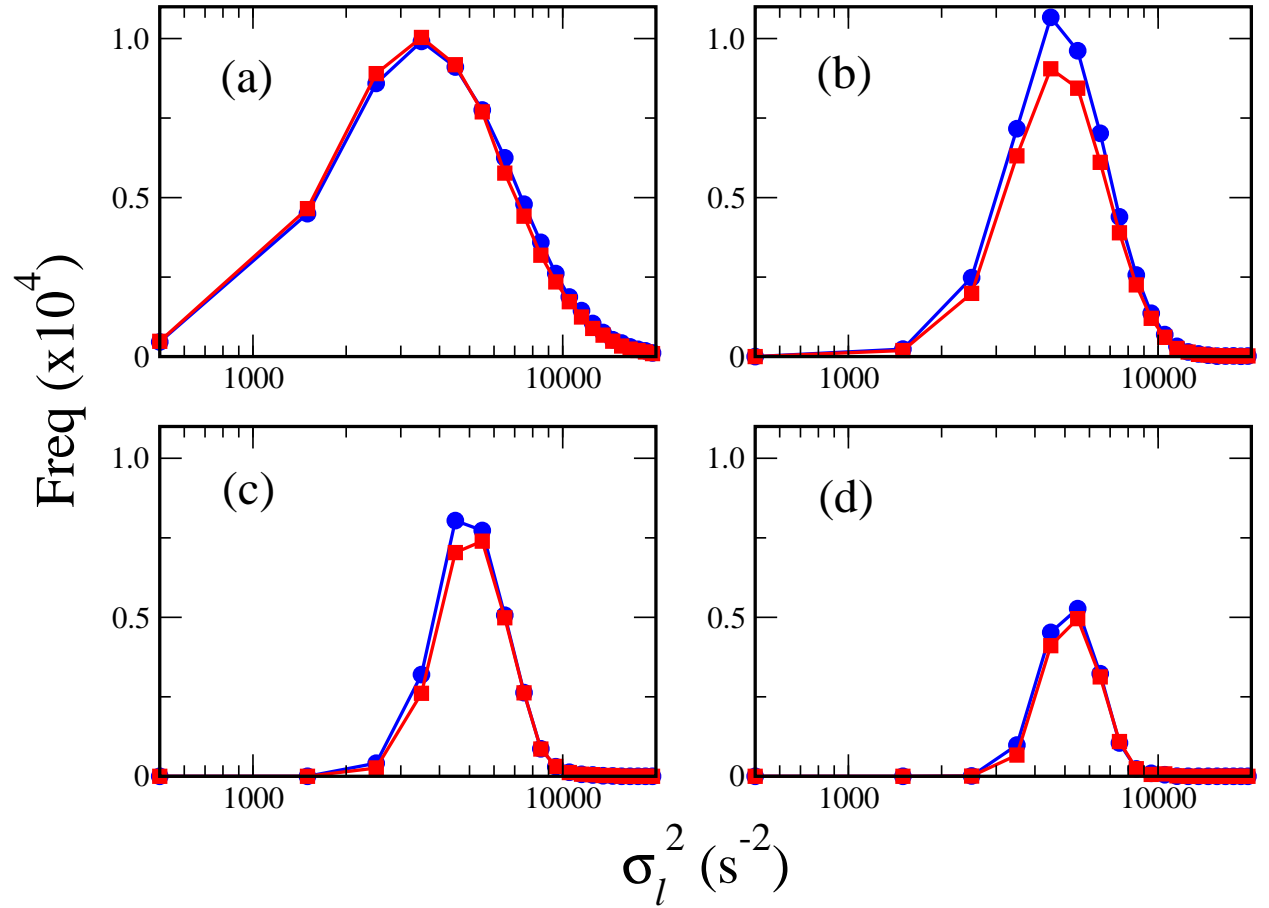


Figure 30: The number of events (frequency) of the coarse-grained outward energy flux Π_l^+ (circles) and inward flux Π_l^- (squares). The length scales l are 0.31 (a), 0.93 (b), 1.56 (c), and 2.17 (d) cm.

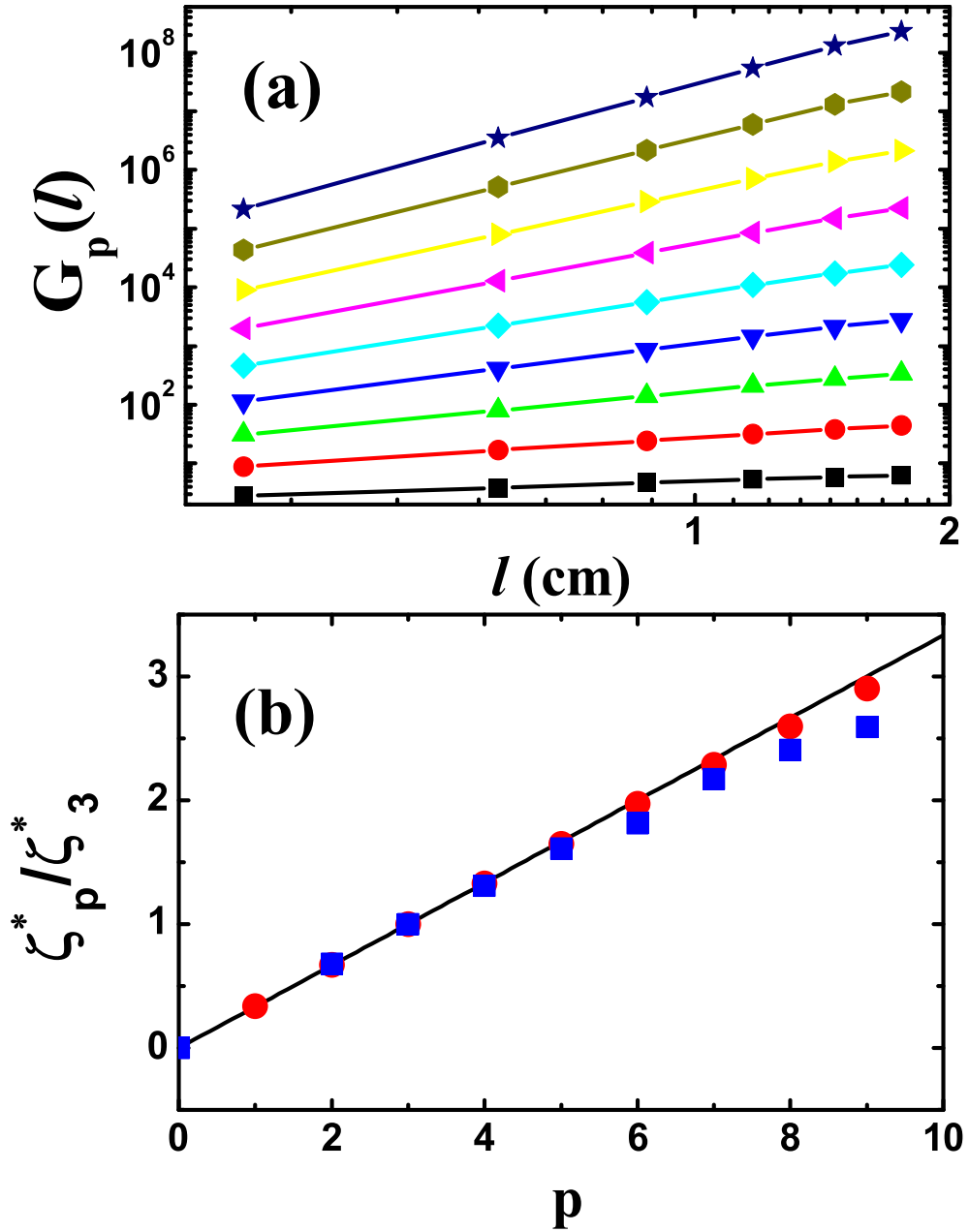


Figure 31: (a) The coarse-grained high order moments $G_p(l)$. From bottom to top, $p=1$ to 9. (b) The scaling exponent ζ_p/ζ_3 as a function of p . The squares represent data from previous analysis [29] and the circles are obtained from coarse-grained velocity difference.

Next, we investigated intermittency through the coarse-grained high-order structure functions, defined as

$$\begin{aligned}
G_p(l) &\equiv \langle \langle \{\delta v_l^3\}^{p/3} \rangle \rangle \\
&= \int_{-\infty}^{+\infty} \{\delta v_l^3\}^{p/3} P(\{\delta v_l^3\} | \sigma_l^2) d\{\delta v_l^3\} \\
&\sim l^{\zeta_p^*}
\end{aligned}$$

where $\langle \dots \rangle$ represents the conditional ensemble average, and the scaling exponent ζ_p^* is used to distinguish ζ_p from previous analysis [29]. Fig. 31(a) shows $G_p(l)$ as a function of the length l up to $p = 9$. The scaling range is extended to the entire inertial range and one can obtain ζ_p^* by a linear fitting algorithm. The relative scaling exponents ζ_p^*/ζ_3^* are obtained by the extended self-similarity (ESS) suggested by Benzi et. al. [7] and plotted in Fig. 31(b). In the figure, the circles and the squares represent ζ_p^*/ζ_3^* and ζ_p/ζ_3 , respectively. When compared with our previous analysis, the intermittency effect is significantly reduced. From this, we may conclude that intermittency stems from the non-uniform distribution of the energy dissipation rate or the squared strain rate in fully developed turbulence.

APPENDIX C

THE STATISTICS OF PRESSURE FLUCTUATIONS

C.1 INTRODUCTION

One of the interesting properties of turbulence is the spatial distribution of the pressure fields. It has not attracted as much attention as the study of the velocity fields, despite its importance. The equation of motion describing 2D turbulent flow in the soap film is the 2D Navier-Stokes equation

$$\partial_t v_i + v_j \partial_j v_i = -\partial_i p + \nu \partial_j \partial_j v_i + f_i - \alpha v_i, \quad (\text{C.1})$$

where α is the drag coefficient between the air and the soap film, p is reduced pressure which is P/ρ where P is pressure and ρ is the density of fluid. f_i is the reduced force which is F_i/ρ where F_i is the external force. The pressure gradient is one of four forces governing the dynamics of the flow; the external force f_i , the dissipative force $\nu \partial_j \partial_j v_i$, the drag force by the air αv_i , and the pressure gradient force $\partial_i p$. Among these forces, the pressure gradient $\partial_i p$ does not contribute the creation or the dissipation of the energy, but it accelerates the fluid molecules and redistributes energy among different velocity components.

The Poisson expression of the pressure fields can be obtained by taking the divergence of Eq. (C.1). After applying the incompressible condition ($\partial_i v_i = 0$), one gets the following simple result:

$$-\nabla^2 p = \Lambda, \quad (\text{C.2})$$

where $\Lambda \equiv (\sigma^2 - \omega^2)/2$. Here the squared strain rate is defined as $\sigma^2 = \sum_{i,j}(\partial_i v_j + \partial_j v_i)^2/2$ and the enstrophy $\omega^2 = \sum_{i,j}(\partial_i v_j - \partial_j v_i)^2/2$. The statistics of the quantity Λ has been investigated by Hua [28] and Rivera et al. [47]. Rivera et al. showed that the positive tail of the PDF of Λ decays differently from the negative tail due to the different number of degrees of freedom of the flow structures, assuming that the statistics of the stream fields are random Gaussian.

The spectrum of pressure fluctuations is defined as follows:

$$\langle p^2 \rangle = \int_0^\infty E_{pp}(k) dk,$$

where

$$E_{pp}(k) \sim \langle \varepsilon \rangle^{4/3} k^{-7/3} \quad (\text{C.3})$$

in the inertial range for high Reynolds numbers. This scaling relation was derived theoretically with various assumptions in the 1950s by Batchelor [5]. Measurements by George, Beuther, and Arndt [25] and Tsuji and Ishihara [58] supported the $-7/3$ scaling in fully developed 3D turbulence. Others [12, 34] found deviations from such a scaling law.

C.2 EXPERIMENTAL RESULTS

Our experiments were performed using a freely-suspended soap film in an electromagnetic convection cell as described in Chap. 4.

As shown in Fig. 32, the pressure field is color-coded with strong positive pressure being represented by red and the strong negative pressure being represented by blue. As expected, most of positive pressure regions are associated with the saddle structures of the flow, while most of the negative pressure regions are associated with the vortex structures of the flow. Both of the positive (right handed) and the negative (left handed) vortices give negative pressure values. Careful examinations of the pressure field suggest that the negative values of pressures are more abundant compared to the positive ones but also have large numerical

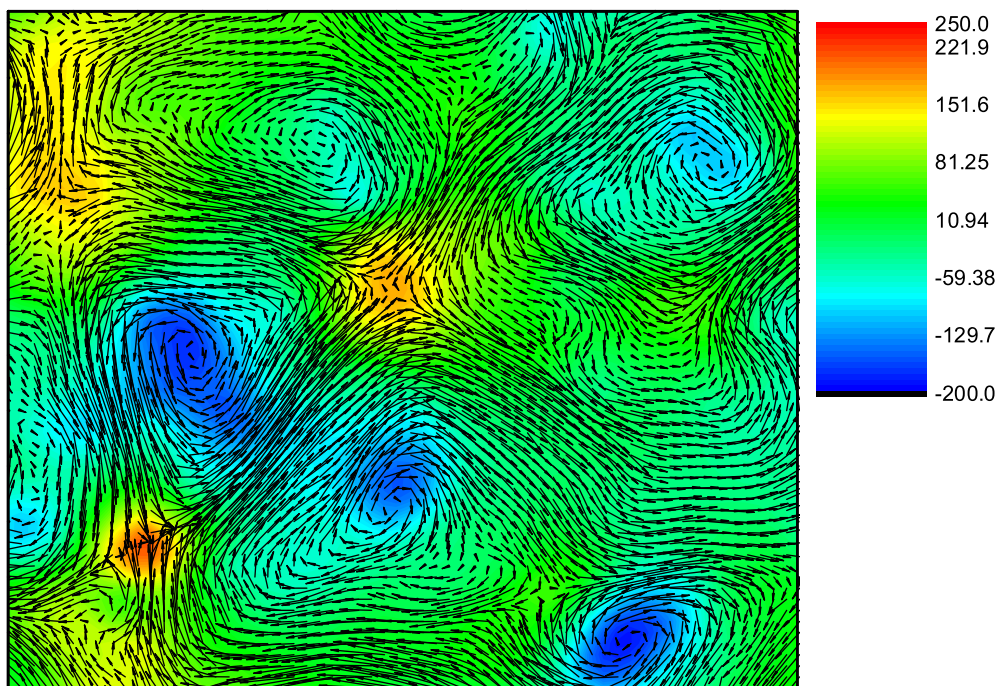


Figure 32: The snapshot of the pressure field (color-coded) and the velocity field (arrows).

Run No.	Re_λ	$\langle p^2 \rangle^{1/2} / \langle u^2 \rangle$	$-S_p$	F_p
1	212	0.526	0.45	4.23
2	180	0.525	0.50	4.07
3	136	0.522	0.66	5.12
4	110	0.535	0.56	4.68

Table 1: The table of the skewness S_p and the flatness F_p of pressure fluctuations.

values. Since $\langle p \rangle = 0$ it suggests that the peak of the pressure PDF $P(p)$ should be in the positive p region.

Table 1 shows the summary of the measurements of pressure. Four turbulence intensities are investigated with Taylor micro-scale Reynolds number $\text{Re}_\lambda = 212, 180, 137,$ and $110,$ respectively. The non-dimensionalized pressure PDFs, $p' = p/\sigma_p$, for all runs are plotted in Fig. C.2, where σ_p is the variance of the pressure fluctuations. The inset of Fig. C.2 shows σ_p^2 which is a linear increasing function of Re_λ . The different color lines indicate different runs: black (1), red (2), blue (3), and green (4). For all runs, the non-dimensionalized PDFs collapse on to each other remarkably well, which means the reduced pressure PDF is a universal function independent of Re_λ . The the tail part of the non-dimensionalized PDF of pressure fluctuations can be described by an exponential function, in the form of

$$P(p/\sigma_p) \sim \exp \left[-\gamma^\pm (|p|/\sigma_p) \right],$$

where γ^\pm are nondimensional parameters which are independent of Re_λ but has different values for positive and negative pressures. Experimentally, we found $\gamma^+ \simeq 2.05$ and $\gamma^- \simeq 1.25$. The negative side of the PDF has a longer tail than the positive side. The exponential form of the pressure PDF may be loosely connected with the fact that two-point velocity correlation function on large scales is Gaussian [26]. The positive side of PDF is also approximately exponential though near the top, it is Gaussian [45].

Fig. 34 shows the plot of the first three non-trivial moments of the pressure fluctuations as a function of Re_λ . The average pressure fluctuations $p_{\text{norm}} \equiv \langle p^2 \rangle^{1/2} / \langle u^2 \rangle$ are shown in

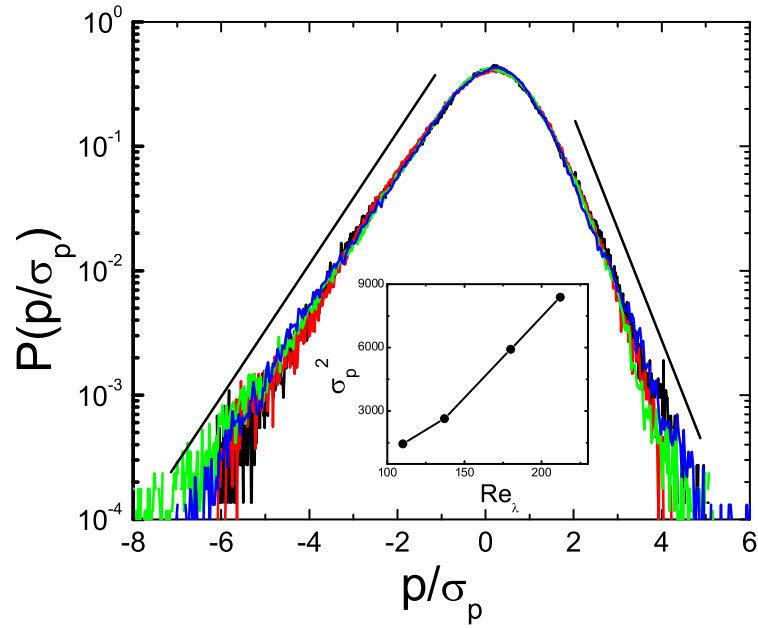


Figure 33: The non-dimensionalized PDF of pressure for all runs (see Table 1). The black, red, blue, and green lines indicate the run 1, 2, 3, and 4, respectively. The tail part of the PDF decays exponentially.

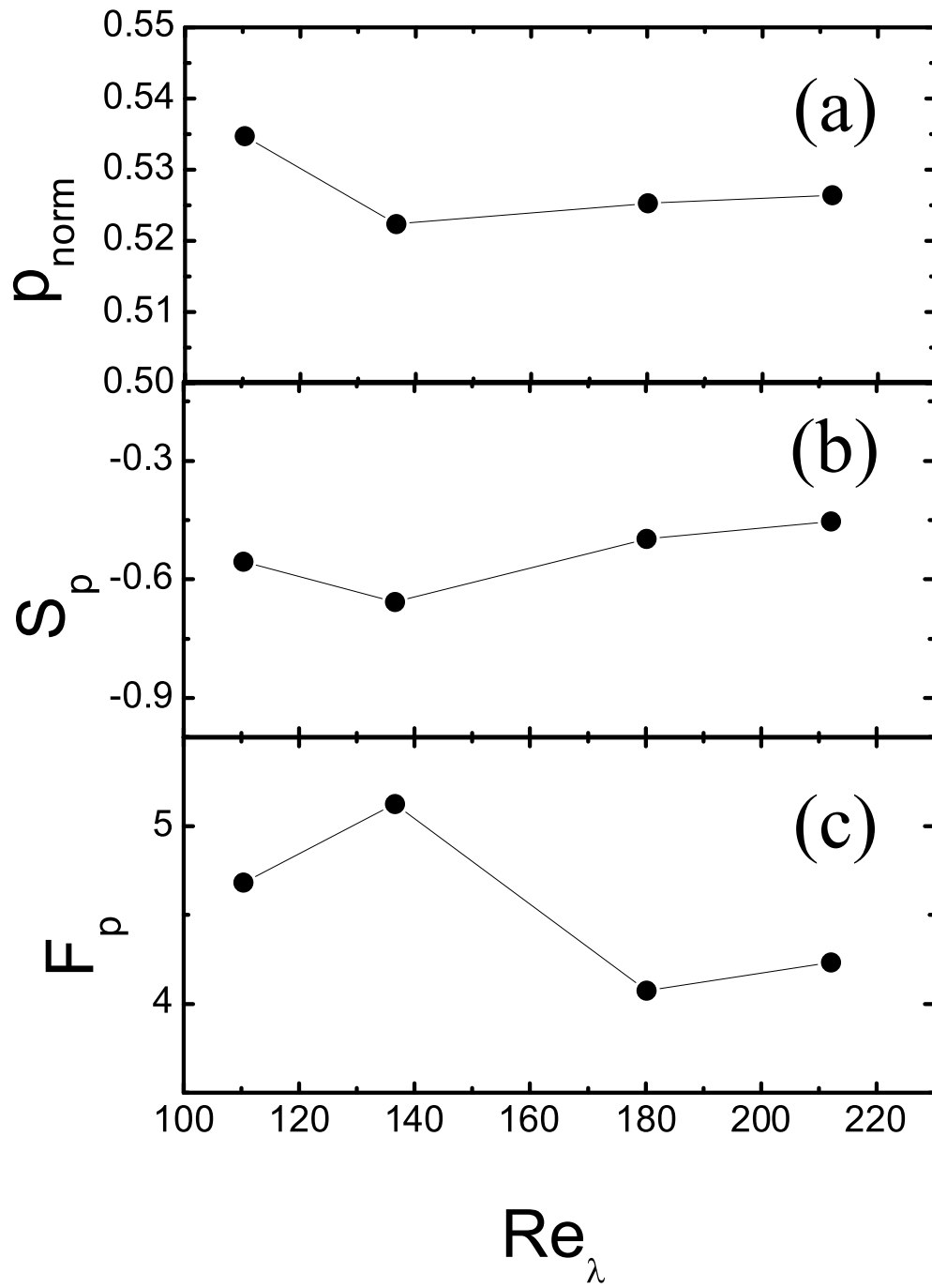


Figure 34: The lower moments of pressure fluctuations: (a) p_{norm} , (b) the skewness S_p , and (c) flatness F_p (see the contents for the definitions)

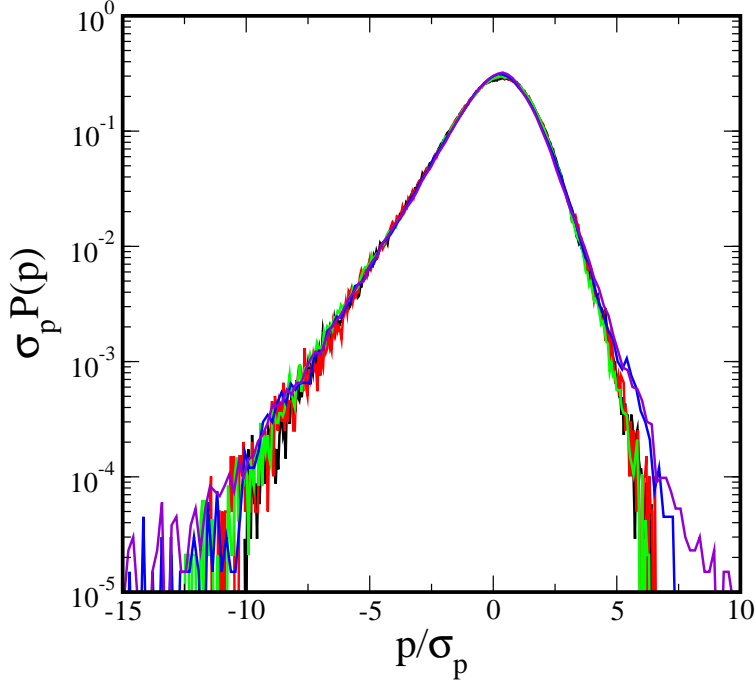


Figure 35: The pressure PDFs in presence of polymer.

Table 1. In 3D turbulence, Batchelor shows that for Gaussian velocity fields, $p_{\text{norm}} = 0.6$ [4]. Our measurements show that $p_{\text{norm}} \simeq 0.53$ and almost constant over the range of Reynolds number we investigated. The useful values to characterize the PDF of fluctuating quantities are the skewness S_p and the flatness F_p which are defined as

$$S_p \equiv \frac{\langle p^3 \rangle}{\langle p^2 \rangle^{3/2}},$$

and

$$F_p \equiv \frac{\langle p^4 \rangle}{\langle p^2 \rangle^2}.$$

In 2D turbulence, Holzer and Siggia found that $S_p = -1.92$ and $F_p = 9$ when the velocity is restricted to a shell, and $S_p = -1.19$ and $F_p = 6.44$ for the equilibrium spectrum $E(k) \sim k/(k^2 + k_0^2)$, with $k_0=6$ and $k < 118$ [26]. As shown in Table 1, in our experiment, both of S_p and F_p are much less than the values obtained by Holzer and Siggia. The discrepancy may be due to the unrealistic velocity spectrum they used.

An interesting observation was also made in the presence of different amounts of linear polymers (the experimental details are given in Chap. 2 and in Ref. [30]) as displayed in Fig. 35. The pressure fields in this case were again calculated based on the Λ -distributions using Eq. C.2. It is found that for low polymer concentrations (0-9 ppm) the $P(p)$ is essentially the same as without polymers. On the other hand, for high polymer concentrations (12 and 24 ppm), the $P(p)$ is different for the large positive p but remains the same for negative p . The broadening of $P(p)$ for $p/p_{rms} \ll 1$ makes the pdfs significantly more symmetric than without polymers. Interesting, the change of PDFs occurs at the same polymer concentration where turbulent quenching was observed (see. Chap. 2). While it is reasonable to speculate that the changes in the pressure PDFs is a result of changes in the turbulent structures, particularly the saddle structures. The basic physics is not known at present. The main difficulty is the constitutive equation for polymers in the soap films and its effect on the pressure equation (C.2) is not characterized. Our experiment may provide some clues as what forms of the constitutive equation are reasonable and what are not.

Regarding the power spectrum of pressure, even though one can calculate the scaling law for E_{pp} using a dimensional analysis as given in Eq. (C.3), the result is controversial. In 3D turbulence, there are many measurements for the pressure spectrum. George, Benter, and Arndt showed that $E_{pp}(k)$ follows the classical result $E_{pp} \sim k^{-7/3}$ [25]. Pumir also gave support to this scaling relation using a computer simulation [45]. Recently, Tsuji and Ishihara reported $E_{pp}(k)$ scales as $k^{-7/3}$ for $Re_\lambda > 600$ in a turbulence jet [58]. The scaling exponent other than $-7/3$ was also found by other investigations. Pullin and Rogallo [44], and Cao, Chen and Doolen [12] found that $E_{pp}(k) \sim k^{-5/3}$ through the computational study. There is no agreement to the scaling exponent of pressure as far as we know. In 2D turbulence, it is predicted by the same dimensional analysis that $E_{pp}(k) \sim k^{-7/3}$ for large scales ($k < k_{inj}$) and k^{-5} for small scales ($k > k_{inj}$). Lesieur, Ossia, and Métais found the result in support of Kolmogorov scaling for pressure using a quasi-normal or Eddy Damped Quasi-normal Markovianised approximation [34]. Our data shows an agreement with the Kolmogorov scaling of pressure in 2D turbulence. The 2D pressure power spectrum is presented in Fig. 36.

In Fig. 37, the power spectra of pressure are plotted for four different runs with Reynolds

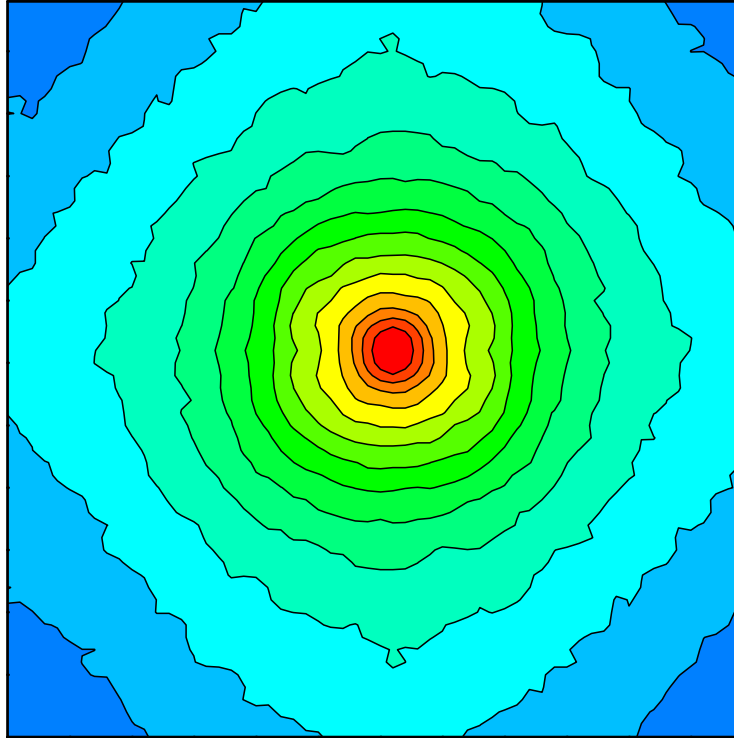


Figure 36: The pressure spectrum $E(k_x, k_y)$ in k -space.

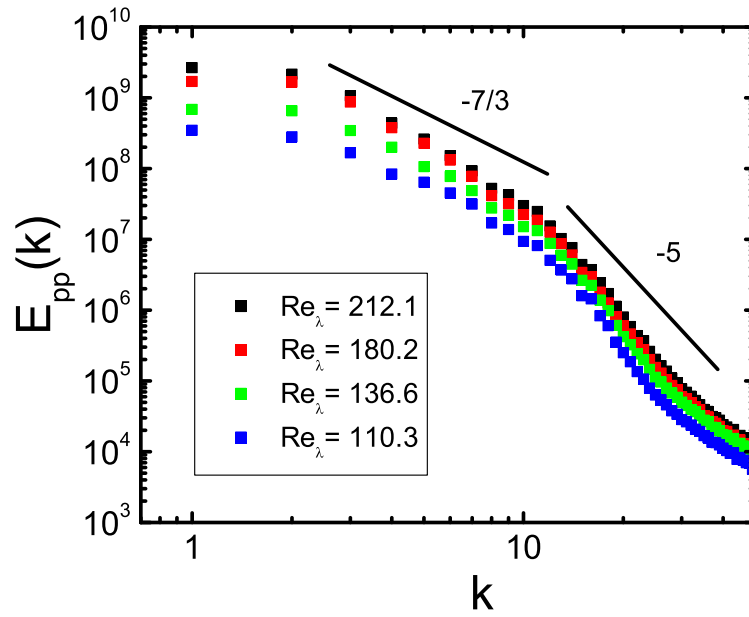


Figure 37: The power spectrum of the pressure $E_{pp}(k)$ for four different turbulence intensities: $Re_\lambda =$ (squares), 180 (circles), 137 (triangle-ups), and 110 (triangle-downs). All have same scaling exponent in both of large and small scales.

number $\text{Re}_\lambda = 212, 180, 137,$ and 110 . For all runs, the scaling behavior is almost the same except for the magnitude of the spectrum. This plot shows two scaling ranges: in the inverse energy cascade regime, $k < k_{inj}$, $E_{pp}(k)$ scales as $k^{-7/3}$ and in enstrophy regime, $k > k_{inj}$, $E_{pp}(k)$ scales as k^{-5} .

C.3 CONCLUSION

The properties of pressure fluctuations were also investigated for various turbulence intensities. The negative side of PDF of pressure fluctuations decays slower than the positive one, but both of them have the exponential tails. It is presented that the spectra of pressure approximately scale as k^{-5} in small scales and $k^{-7/3}$ in large scales.

BIBLIOGRAPHY

- [1] Y. Amarouchene and H. Kelley. Polymer in 2d turbulence: Suppression of large scale fluctuations. *Phys. Rev. Lett.*, 89(10):104502, 2002.
- [2] A. Anselmet, Y. Gagne, R. J. Hopfinger, and R. A. Antonia. High-order velocity structure functions in turbulent shear flows. *J. Fluid Mech.*, 140:63–89, 1984.
- [3] A. Babiano, B. Dubrulle, and Frick P. Scaling properties of numerical two-dimensional turbulence. *Phys. Rev. E*, 52:3719, 1995.
- [4] B.K. Batchelor. Pressure fluctuations in isotropic turbulence. *Proc. Cambridge Philos. Soc.*, 47:359, 1951.
- [5] B.K. Batchelor. *Theory of Homogeneous Turbulence*. Cambridge University Press, New York, 1953.
- [6] A. Belmonte, W.I. Goldburg, H. Kellay, M.A. Rutgers, B. Martin, and X.L. Wu. Velocity fluctuations in a turbulent soap film: The third moment in two dimensions. *Phys. Fluids*, 11:1196, 1999.
- [7] R. Benzi, S. Ciliberto, Tripiccione R., Baudet C., F. Massaioli, and S. Succi. Extended self-similarity in turbulent flows. *Phys. Rev. E*, 48:R29, 1993.
- [8] Roberto Benzi, Elisabetta De Angelis, Rama Govindarajan, and Itamar Procaccia. Shell model for drag reduction with polymer additives in homogeneous turbulence. *Phys. Rev. E*, 68:016308, 2003.
- [9] G. Boffetta, A. Celani, and M. Vergassola. Inverse energy cascade in two-dimensional turbulence: Deviations from gaussian behavior. *Phys. Rev. E*, 61:R29, 2000.
- [10] Guido Boffetta, Antomio Celani, and Stefano Musachio. Two-dimensional turbulence of dilute polymer solutions. *Phys. Rev. Lett.*, 91(3):34501, 2003.
- [11] V. Borue. Inverse energy cascade in stationary two-dimensional homogeneous turbulence. *Phys. Rev. Lett.*, 72:1475, 1994.
- [12] Nianzheng Cao, Shiyi Chen, and Gary D. Doolen. Statistics and structures of pressure in isotropic turbulence. *Phys. Fluids*, 11:2235, 1999.

- [13] Pierre-Henri Chavanis, Joel Sommeria, and R Robert. Statistical mechanics of two-dimensional vortices and collisionless stellar system. *Astrophys. J.*, 471:385–399, 1996.
- [14] Shiyi Chen, Gary D. Doolen, Robert H. Kraichnan, and Zhen-Su She. On statistical correlations between velocity increments and locally averaged dissipation in homogeneous turbulence. *Phys. Fluids*, A 5:458, 1993.
- [15] J.R. Cressman, Q. Bailey, and W.I. Goldburg. Modification of a vortex street by a polymer additive. *Phys. Fluids*, 13:867, 2001.
- [16] W. Brent Daniel and Maarten A. Rutgers. Topology of two-dimensional turbulence. *Phys. Rev. Lett.*, 89:134502, 2002.
- [17] J. M. J. de Toonder, M. A. Hulsen, G. D. C. Kuiken, and F. T. M. Nieuwstadt. Drag reduction by polymer additives in a turbulent pipe flow: numerical and laboratory experiments. *J. Fluid. Mech.*, 337:193, 1997.
- [18] T. Dudok de Wit. Can high-order moments be meaningfully estimated from experimental turbulence measurements? *Phys. Rev. E*, 70:055302, 2004.
- [19] Berengere Dubrulle. Intermittency in fully developed turbulence: Log-poisson statistics and generalized scale covariance. *Phys. Rev. Lett.*, 73:959, 1994.
- [20] G. Falkovich, I. Kolokolov, V. Lebedev, and A. Migdal. Instantons and intermittency. *Phys. Rev. E*, 54:4896, 1996.
- [21] G. Falkovich and V. Lebedev. Single-point velocity distribution in turbulence. *Phys. Rev. Lett.*, 79:4159, 1997.
- [22] M. Farge, K. Schneider, and N. Kevlahan. Non-gaussianity and coherent vortex simulation for two-dimensional turbulence using an adaptive orthogonal wavelet basis. *Phys. Fluids*, 11:2187, 1999.
- [23] U. Frisch. *Turbulence*. Cambridge University Press, Cambridge, 1995.
- [24] Y. Gagne. *Contribution a l'etude experimentale de l'intermittence de la turbulence a petite echelle*. PhD thesis, Universite de Grenoble, 1980.
- [25] W. K. George, P. D. Benter, and R. E. Arndt. Pressure spectra in turbulent free shear flows. *J. Fluid Mech.*, 148:155, 1984.
- [26] Mark Holzer and Eric D. Siggia. Skewed, exponential pressure distributions from gaussian velocities. *Phys. Fluids A*, 5:2525, 1993.
- [27] I. Hosokawa, C. W. Van Atta, and S. T. Thoroddsen. Experimental study of the kolmogorov refined similarity variable. *Fluid Dyn. Res.*, 13:329–333, 1994.

- [28] L.H. Hua. Skewness of the generalized centrifugal force divergence for a joint normal distribution of strain and vorticity components. *Phys. of Fluids*, 6:32000–3202, 1994.
- [29] Yonggun Jun and X.L. Wu. Large-scale intermittency in two-dimensional driven turbulence. *Phys. Rev. E*, 72:035302(R), 2005.
- [30] Yonggun Jun, Jie Zhang, and X. L. Wu. Submitted for publication, 2005.
- [31] A.N. Kolmogorov. The local structure of turbulence in incompressible viscous fluid for very large reynolds number. *Dokl. Akad. Nauk SSSR*, 30:9, 1941.
- [32] A.N. Kolmogorov. A refinement of previous hypotheses concerning the local structure of turbulence in a viscous incompressible fluid at high reynolds number. *J. Fluid Mech.*, 13:82, 1962.
- [33] Robert H. Kraichnan. Inertial ranges in two-dimensional turbulence. *Phys. Fluids*, 10:1417, 1967.
- [34] Marcel Lesieur, Sepand Ossia, and Olivier Metais. Infrared pressure spectra in two- and three-dimensional isotropic incompressible turbulence. *Phys. Fluids*, 11:1535, 1999.
- [35] I. Lifshits, S. Gredeskul, and A. Pastur. *Introduction to the Theory of Disordered Systems*. Wiley, New York, 1988.
- [36] Erik Lindborg. A note on Kolmogorov’s third-order structure-function law, the local isotropy hypothesis and the pressure-velocity correlation. *J. Fluid Mech.*, 326:343–356, 1996.
- [37] J. L. Lumley. Drag reduction in turbulent flow by polymer additives. *J. Polym. Sci.*, 7:263–290, 1973.
- [38] Victor S. L’vov, Anna Pomyalov, and Itamar Procaccia. Guasi-gaussian statistics of hydrodynamic turbulence in $4/3+\epsilon$ dimensions. *Phys. Rev. Lett.*, 89:064501–1, 2002.
- [39] A. Monin and A.M. Yaglom. *Statistical Fluid Mechanics*. MIT Press, Cambrigde, 1975.
- [40] E.A. Novikov. Intermittency and scale similarity of the structure of turbulent flow. *Prikl. Math. Mekh.*, 35:266, 1970.
- [41] Jerome Paret and Patrick Tabeling. Intermittency in the 2d inverse cascade of energy: experimental observations. *Phys. Fluids*, 10:3126, 1998.
- [42] Giorgio Parisi and U. Frisch. Turbulence and predictability in geophysical fluid dynamics. In Ghil. M, R. Benzi, and Giorgio Parisi, editors, *International School of Physics “Enrico Fermi”*, page 84, North-Holland, Amsterdam, 1985.

- [43] A. A. Praskovsky. Experimental verification of the kolmogorov refined similarity hypothesis. *Phys. Fluids A*, 4:2589, 1992.
- [44] D. I. Pullin and R. S. Rogallo. Pressure and higher-order spectra for homogeneous isotropic turbulence. In *the Summer Program*, page 177, Center for Turbulence Research, 1994.
- [45] Alain Pumir. A numerical study of pressure fluctuations in three-dimensional, incompressible, homogeneous, isotropic turbulence. *Phys. Fluids*, 6:1071, 1994.
- [46] Lewis Fry Richardson. *Weather prediction by numerical processes*. Cambridge University Press, Cambridge, 1922.
- [47] M. Rivera, X. L. Wu, and C. Yeung. Universal distribution of centers and saddles in two-dimensional turbulence. *Phys. Rev. Lett.*, 87(4):044501, 2001.
- [48] M. Rivera and X.L. Wu. External dissipation in driven soap film turbulence. *Phys. Rev. Lett.*, 85:976, 2000.
- [49] Michael Rivera and Xiao Lun Wu. Homogeneity and the inertial range in driven two-dimensional turbulence. *Phys. Fluids*, 14:3098, 2002.
- [50] Michael. K. Rivera. *The Inverse Energy Cascade of Two-dimensional Turbulence*. PhD thesis, University of Pittsburgh, 2000.
- [51] M. A. Rutgers. Forced 2d turbulence: Experimental evidence of simultaneous inverse energy and forward enstrophy cascades. *Physical Review Letters*, 81(11):2244–7, 1998.
- [52] Zhen-Su She and Emmanuel Leveque. Universal scaling laws in fully developed turbulence. *Phys. Rev. Lett.*, 72:336, 1994.
- [53] L.M. Smith and Victor Yakhot. Bose condensation and small-scale structure generation in a random force driven 2d turbulence. *Phys. Rev. Lett.*, 71:352, 1993.
- [54] J. Sommeria. Experimental study of the two-dimensional inverse energy cascade in a square box. *J. Fluid Mech.*, 170(139), 1986.
- [55] G. Stolovitzky, P. Kailasnath, and K. R. Sreenivasan. Kolmogorov’s refined similarity hypothesis. *Phys. Rev. Lett.*, 69:1178, 1992.
- [56] Tabor Tabor and P.-G. de Gennes. A cascade theory of drag reduction. *Europhys. Lett.*, 2:519–522, 1986.
- [57] B. A. Toms. In *Proceedings of the international congress on rheology*. North-Holland, Amsterdam, 1949.
- [58] Yoshiyuki Tsuji and Takashi Ishihara. Similarity scaling of pressure fluctuation in turbulence. *Phys. Rev. E*, 68:026309, 2003.